

Ane Bjerkebak

Design Sensitivity Analysis of the X-rotor Offshore Wind Turbine Jacket Structure

Master's thesis in Civil and Environmental Engineering

Supervisor: Michael Muskulus

Co-supervisor: Adriana Correia da Silva

June 2023

Ane Bjerkebæk

Design Sensitivity Analysis of the X-rotor Offshore Wind Turbine Jacket Structure

Master's thesis in Civil and Environmental Engineering
Supervisor: Michael Muskulus
Co-supervisor: Adriana Correia da Silva
June 2023

Norwegian University of Science and Technology
Faculty of Engineering
Department of Civil and Environmental Engineering



Preface

I would like to express my deepest gratitude to my supervisor, Michael Muskulus, for his guidance and engagement when introducing me to this field of study. His ability to quickly understand complex problems and provide smart feedback was invaluable. Likewise, I would like to express my greatest appreciation to co-supervisor Adriana Correia da Silva. She eagerly answered and discussed my questions and doubts with a positive attitude and shared her valuable knowledge on the finite element solver FEDEM Windpower.

Additionally, I want to acknowledge the contributions of the other members of our Wednesday group meetings: Jing Dong, David Oyegbile, Glen Oumellal and Eva Melina Schmitt. Their patience and thoughtful input during discussions significantly enhanced my understanding. During these meetings, Professor Muskulus shared anecdotes from his experiences working in offshore wind energy. These stories were not only enlightening but also served to create a relaxed atmosphere in our sessions. Hearing about his journey in the field has been truly inspiring, and I am excited about embarking on my own career in this area of research.

Abstract

The X-rotor is an innovative offshore wind turbine project in the field of renewable energy. It aims to develop a new type of wind turbine incorporating an X-shaped rotor, a hybrid vertical-horizontal axis design. A feasibility study indicated that this concept could diminish operational and maintenance costs, thereby reducing the overall cost of energy by an impressive 20 to 30 percent. Furthermore, the X-rotor concept offers a fresh perspective on vertical axis wind turbines, a design yet to gain large-scale commercial success. This concept confronts the inherent structural drawbacks while capitalising on the benefits of rotor power take-off systems close to the ground.

In the early design stages of the X-rotor jacket structure, it is essential to generate near-optimal designs that highlight the superiority of the X-rotor over conventional offshore wind turbines. The turbine is anchored by a four-legged jacket structure, initially positioned at a water depth of 40 meters. Achieving a cost-effective design in early phases requires a robust design sensitivity analysis. This paper examines the jacket structure of the X-rotor offshore wind turbine, where the fatigue limit state typically determines the structure's lifespan.

The direct differentiation method, a gradient-based method, is implemented to perform the design sensitivity analysis. This method quantifies the change in response, stress, and damage due to variations in the cross-sectional properties of the tubular beams in the jacket structure. The structural analysis is performed in FEDEM Windpower. To determine the response sensitivity accurately, the stiffness matrix is obtained numerically using the flexibility method. The flexibility method also called the force method, is performed on two simple structures and a beam in the X-rotor to verify the method and compare it to the Euler-Bernoulli beam theory. The study uncovers a non-linear relation between loads and response in FEDEM, especially in bending. This influences both the design sensitivity analysis and the stiffness matrix. Deriving the stiffness matrix numerically demands more computational resources compared to the marginal accuracy achieved. The analytical stiffness matrix of an Euler-Bernoulli beam element is used further in the sensitivity analysis. The direct differentiation method can accurately determine damage sensitivities as the jacket structure is primarily subjected to stress from axial loading, which is not notably impacted by the non-linear effect.

Critical sections to fatigue damage are the welded joints, which are evaluated using the hot spot approach. Changes in the beam's thickness cause more variation in the stress concentration factors (SCFs) of the welded joints compared to changes in radius. Consequently, optimisation efforts should prioritise thickness, given its more significant impact on damage, as thickness and radius contribute equally to the structure's mass. Ultimately, the goal of optimisation should be to minimise the ratio between the brace and chord thickness, denoted as τ , as this decreases damage and mass.

Keywords: offshore wind, jacket structure, fatigue, design sensitivity analysis, direct differentiation method, numerical stiffness matrix, stress concentration factors

Sammendrag

X-rotor er et innovativt offshore vindturbin-prosjekt innen fornybar energi. Målet er å utvikle en ny type vindturbin som har en X-formet rotor, en hybrid mellom vertikalt og horisontalt aksedesign. En mulighetsstudie indikerte at dette konseptet kan redusere drifts- og vedlikeholdskostnader, og dermed redusere den totale energikostnaden med inntil 20 til 30 prosent. Videre gir X-rotor et nytt perspektiv på vertikalakslede vindturbiner, et design som ennå ikke har oppnådd storskala kommersiell suksess. Dette konseptet tar tak i de strukturelle ulempene samtidig som det utnytter fordelene ved å ha kraftuttakssystemet i rotor nærmer bakken.

I de tidlige designstadiene av X-rotorens jacket konstruksjon er det essensielt å oppnå tilnærmet optimalt design slik at X-rotorens fordel kan fremheves over konvensjonelle offshore vindturbiner. Turbinen er forankret med en firebeint jacket konstruksjon, opprinnelig plassert på 40 m dypt vann. For å oppnå et kostnadseffektivt design i tidlige faser kreves en robust sensitivitetsanalyse. Denne oppgaven undersøker jacket konstruksjonen til X-rotor, hvor utmattelse mest sannsynlig bestemmer konstruksjonens levetid.

Den direkte differensieringsmetoden, en gradientbasert metode, blir implementert for å utføre sensitivitetsanalysen. Denne metoden finner endringen i respons, spenning og utmattelse på grunn av endringer i tverrsnittsegenskapene til de rørformede bjelkene i jacket konstruksjonen. Den strukturelle analysen utføres i FEDEM Windpower. For å bestemme responssensitiviteten nøyaktig, blir stivhetsmatrisen funnet numerisk ved hjelp av fleksibilitetsmetoden. Fleksibilitetsmetoden, også kalt kraftmetoden, utføres på to enkle strukturer og en bjelke i X-rotor jacketen for å verifisere metoden og sammenligne den med Euler-Bernoulli bjelketeori. Studien avdekker en ikke-lineær relasjon mellom laster og respons i FEDEM, spesielt ved bøyning. Dette påvirker både sensitivitetsanalysen og stivhetsmatrisen. Å finne stivhetsmatrisen numerisk krever mer databehandlingsressurser sammenlignet med den marginale nøyaktigheten oppnådd. Den analytiske stivhetsmatrisen til et Euler-Bernoulli bjelkeelement brukes videre i sensitivitetssanalysen. Den direkte differensieringsmetoden kan nøyaktig bestemme utmattelsessensitiviteten ettersom jacket konstruksjonen hovedsakelig er utsatt for spenninger fra aksial belastning, som ikke påvirket markant fra den ikke-lineære effekten.

Kritiske punkter for utmatting er de sveisede skjøtene, som evalueres ved hjelp av en hot spot tilnærming. Endringer i bjelkens tykkelse forårsaker mer variasjon i stresskonsentrasjonsfaktorene (SCF) til de sveisete leddene sammenlignet med endringer i radius. Dermed bør optimalisering prioritere tykkelsen, gitt dens mer betydelige innvirkning på utmattelse, da tykkelse og radius bidrar like mye til strukturens masse. Til slutt bør målet med optimalisering være å minimere forholdet mellom tykkelsen på stagene og jacket-benene, betegnet som τ , da dette reduserer utmattelse og masse.

Nøkkelord: offshore vind, jacket konstruksjon, utmattelse, design sensitivitetsanalyse, direkte differensieringsmetode, numerisk stivhetsmatrise, stresskonsentrasjonsfaktorer

Table of Contents

| | | |
|----------|--|-----------|
| 1 | Introduction | 1 |
| 1.1 | Motivation of the work | 1 |
| 1.2 | State of the art | 1 |
| 1.3 | Objectives | 2 |
| 1.4 | Structure of the document | 2 |
| 1.5 | Software used | 3 |
| 2 | Theory | 4 |
| 2.1 | X-rotor concept | 4 |
| 2.2 | Sensitivity of a response function | 7 |
| 2.3 | Direct differentiation method | 8 |
| 2.4 | Euler-Bernoulli beam element | 9 |
| 2.5 | Geometrical stiffness | 11 |
| 2.6 | The flexibility method | 11 |
| 2.7 | Coordinate transformation | 12 |
| 2.8 | Fatigue limit state of welded joints in a jacket structure | 14 |
| 2.9 | Rainflow counting | 18 |
| 2.10 | Establishment and differentiation of functions utilizing the least square method | 21 |
| 2.11 | Offshore environment loads | 22 |
| 3 | Numerical stiffness matrix | 25 |
| 3.1 | Numerical stiffness matrix of a vertical beam in 2D | 25 |
| 3.2 | Finding stiffness matrix and its sensitivity numerically on an inclined beam in 3D | 29 |
| 3.3 | Stiffness matrix sensitivity of the beams in X-rotor jacket structure | 33 |
| 4 | Stress concentration factors | 36 |
| 4.1 | Joint classification | 36 |
| 4.2 | SCF dependency on the cross-section properties | 38 |
| 5 | Design Sensitivity analysis | 47 |
| 5.1 | Sensitivity of cross-section properties and step length | 47 |
| 5.2 | Sensitivity of stresses in the X-rotor | 51 |
| 5.3 | Sensitivity of damage in the X-rotor | 58 |

| | |
|--|-----------|
| 6 Conclusion | 68 |
| 6.1 Possibilities for future research | 69 |
| Bibliography | 70 |
| Appendix | 72 |
| A Stress concentration factors | 1 |
| B Damage sensitivity in hot spots of other brace beams as beam 82 is changed | 15 |
| C Damage sensitivity with respect to brace thickness | 23 |
| D Linear regression to find SCF sensitivity for SCF 5 | 41 |

Nomenclature

Abbreviations

| | |
|------|------------------------------|
| SCF | Stress concentration factor |
| DOF | Degree of freedom |
| FEA | Finite element analysis |
| FLS | Fatigue limit state |
| HSS | Hot spot stress |
| DFF | Design fatigue factor |
| IP | In-plane |
| OP | Out-of-plane |
| HAWT | Horizontal axis wind turbine |
| VAWT | Vertical axis wind turbine |
| EOM | Equation of motion |

Symbols

| | |
|----------------|--|
| E | Young's modulus also referred to as E-modulus |
| ν | Poisson's ratio |
| ρ | density |
| t | brace thickness |
| d | brace diameter |
| T | chord thickness |
| D | damage / chord diameter |
| b_i | representing the sensitivity variable |
| \mathbf{u} | response vector |
| \mathbf{K} | stiffness matrix |
| \mathbf{R} | external load vector |
| A | cross-section area |
| I | Second moment of area |
| J | St. Venant torsional constant |
| L | length of beam / length of chord in SCF calculation |
| G | shear modulus |
| v | translation DOF |
| θ | rotation DOF |
| N | axial force |
| M | moment |
| σ | stress / spectral shape parameter in the wave spectrum |
| \mathbf{M} | mass matrix |
| \mathbf{C} | damping matrix |
| \mathbf{K}_G | geometrical stiffness matrix |
| \mathbf{F} | flexibility matrix |
| \mathbf{i} | local coordinate unit vector |
| \mathbf{I} | global coordinate unit vector |
| \mathbf{T} | transformation matrix |
| τ | brace and chord thickness ratio |
| β | brace and chord diameter ratio |

| | |
|------------------|---|
| γ | ratio of chord diameter and thickness |
| α | ratio of chord length and diameter |
| C | constant in SCF function |
| $\Delta\sigma_j$ | stress cycle j |
| N_j | cycles to failure of stress cycle j |
| n_j | cycles of a stress cycle j in a load history |
| k | total number of stress blocks |
| DFF | design fatigue factor |
| ν | usage factor |
| d_j | scaling factor of stress cycle j |
| p | probability of occurrence |
| \bar{a} | intercept of the S-N curve with the logN x-axis |
| m | inverse slope of the S-N curve |
| P_1 | stress cycle count start point in rainflow counting |
| X | active extremum in rainflow counting |
| S | wave spectrum |
| ω | natural frequency |
| T_p | spectral peak period |
| T_{low} | lower cut-off period value |
| T_{high} | higher cut-off period value |
| ω_1 | higher cut-off natural frequency value |
| ω_2 | lower cut-off natural frequency value |
| ω_p | peak natural frequency |
| H_s | significant wave height |
| γ | spectral peakedness factor |
| M_{mg} | added mass due to marine growth |
| ρ_{mg} | average mass density of the marine growth |
| z_u | water depth relative to the mean sea level where the marine growth starts |
| z_l | water depth relative to the mean sea level where the marine growth end |
| t_{mg} | thickness of the marine growth layer |
| U | wind speed |
| U_{10} | mean wind speed over 10 minutes at a 10 meters height |
| α | roughness factor of the terrain |
| I_p | polar moment |
| r | radius |
| g | gap in leg joints |
| F_d | drag force |
| F_a | added mass force |
| ρ_w | water density |
| D_d | drag diameter including marine growth |
| L | beam length |
| C_d | drag coefficient |
| C_a | added mass coefficient |
| u | structure velocity |
| u_w | water particle velocity |
| e | relative error |
| \mathbf{S} | stress calculation matrix |
| SCF | stress concentration factor |

1 Introduction

1.1 Motivation of the work

When designing an offshore wind turbine, the driving constrain is often the damage due to fatigue in the welded joints [14]. The recommended practice regarding fatigue is made such that when the fatigue limit state is reached there is still a small probability of failure. Existing industry guidelines work with S-N curves that have a 97.7 % probability of not exceeding the fatigue limits during the structure's intended lifespan [9]. Thus if all structural parts are fully utilised, 23 out of 1000 turbines are predicted to fail during the designed lifetime. This risk acceptance might appear counterintuitive, but it represents a careful balancing act between durability and cost efficiency. This should be seen as a positive outcome because the remaining 977 turbines stand and are cheap to build in terms of not over-dimension the structure. The result is wind turbines with low mass meaning cheap structures, which give rise to affordable energy. Making today's offshore wind turbines profitable is one of the governing concerns.

However, achieving this delicate balance requires a high degree of accuracy in design considerations. Overly conservative designs can lead to over-dimensioning of the structure, escalating costs without proportionate benefits. Conversely, underestimating the fatigue performance could result in failure during the lifetime and costly repairs or replacements. As such, accurate assessments of fatigue limits and their impacts on structural integrity play a vital role in the economically efficient and successful deployment of offshore wind turbines. It is within this context that this work aims to contribute valuable insights.

1.2 State of the art

The X-rotor is a new hybrid vertical-horizontal axis wind turbine that promises a reduction in the cost of energy compared to existing solutions for extracting offshore wind. A feasibility study suggests that the concept could lower capital costs by mitigating operational and maintenance expenses, leading to a cost of energy reduction[19]. As a part of this innovative concept, NTNU contributes to designing several components, including the jacket support structure. Despite the limited environmental information available during the early design stages, it is vital to establish a design with the same cost framework as the final one to ensure the project's commercial appeal[25].

Oest et al. have conducted a gradient-based optimisation on a horizontal axis wind turbine, focusing on the diameter and thickness of the structural elements to minimise the structure's mass. To achieve this, a design sensitivity analysis using the direct differentiation method was performed[25]. Tortorelli and Michaleris have in their thesis explored three different sensitivity-finding methods – the finite difference method, direct differentiation method, and adjoint method. The direct differentiation method is chosen as it requires only the solution of one pseudo problem for each of the design parameters[31]. Due to the new turbine concept, X-rotor, the jacket structure will face unique design loads, influencing the required material quantity and jacket geometry. Therefore, a design sensitivity analysis using the direct differentiation method should be conducted to evaluate this unique structure and load environment.

For simulations, FEDEM Windpower is used, a simulation software specifically designed for analysing and optimising the performance of wind turbines, including the analysis of loads, dynamics, and power production[12]. Euler-Bernoulli beam theory forms the basis for the design sensitivity analysis carried out in FEDEM. However, the stiffness matrix is obtained numerically using the flexibility method to accurately assess response sensitivity. This method is a standard approach

for determining the inverse of the stiffness matrix, the so-called flexibility matrix. Kollbein Bell discourages this method for complex structures due to its numerical instability to rounding errors when inverting a large matrix[4]. It faces limited application, as finite element software calculates the stiffness matrix of complex structures. However, the matrix is usually not output from the structural analysis. This method becomes essential when analysing the design sensitivity of the X-rotor jacket related to the cross-section properties. In this context, it can be used to numerically determine the stiffness matrix sensitivity for the beam element undergoing changes.

1.3 Objectives

In offshore wind structures, the fatigue limit state (FLS) typically serves as the primary constraint [14]. Therefore, it is essential to examine how the dimensions of the jacket impact the global response and resulting damage. This thesis aims to carry out a design sensitivity analysis focusing on the cross-sectional properties of structures, employing the direct differentiation method under quasi-static assumptions. Establishing damage sensitivity can facilitate dimension optimization and together with ensuring the satisfaction of all constraints leading to a feasible design.

The structure is exposed to quasi-periodic excitation due to aerodynamic load from the rotor and marine forces over its 20-year operational lifetime. A finite element analysis (FEA) is performed on the jacket structure using the finite element solver, FEDEM Windpower. The welded tubular joints, being the critical sections to fatigue damage, will be assessed using the hot spot approach, stress concentration factors, and S-N curves according to DNVGL-RP-C203 [9].

In light of the above, this Master's thesis in Offshore Wind at the Department of Civil and Environmental Engineering at NTNU formulates the following research question and objectives:

Q: Can the direct differentiation method, in conjunction with the flexibility method, accurately ascertain the damage sensitivity of the welded joints in the X-rotor jacket?

OBJ1: Numerically determine the stiffness matrix using the flexibility method.

OBJ2: Investigate the stress concentration factors and their dependency on the cross-sectional properties of the beams.

OBJ3: Implement the direct differentiation method to perform a design sensitivity analysis concerning the damage of the jacket structure.

1.4 Structure of the document

The organization of the thesis is intended to clearly differentiate between the parts of the text which concern the literature review and the author's own contributions. The background theory used in this thesis is provided in Chapter 2. Chapter 3 is connected to OBJ1 where the numerical stiffness matrix is provided for three structures with varying complexity. Each structure has its own section with method, results and discussion. Chapter 4 provides OBJ2 by plotting the SCFs, determining the joint classification and expressing them in terms of the cross-sectional properties. Chapter 5 constitutes OBJ3, which is divided into three sections respectively sensitivity of cross-sectional properties, stresses and damage. All these three sections have a method, result and discussion part, which altogether constitute the design sensitivity analysis. Finally, Chapter 6 contains concluding remarks and suggestions for further research.

1.5 Software used

1. MATLAB version R2020a, a general-purpose mathematical modeling program developed by MathWorks Inc.[28].
2. FEDEM Windpower R7.2.2, a simulation software specifically designed for analysing and optimising the performance of wind turbines, including the analysis of loads, dynamics, and power production[12].
3. Mathcha, an online mathematics editor, used to create figures[24]. Used for all figures if nothing else is specified in the figure text.

2 Theory

2.1 X-rotor concept

The X-rotor offshore wind turbine project is an innovative design in the field of renewable energy. It aims to develop a new type of wind turbine incorporating an X-shaped rotor, a hybrid vertical-horizontal axis design. The goal is to decrease the cost of energy extraction compared to current solutions. A feasibility study indicates that the concept can potentially reduce capital, operational, and maintenance costs, resulting in a notable 20 to 30 percent decrease in the overall cost of energy [19]. A sketch of the X-rotor is shown in Figure 2.1, however, the dimensions are not in the correct scale.

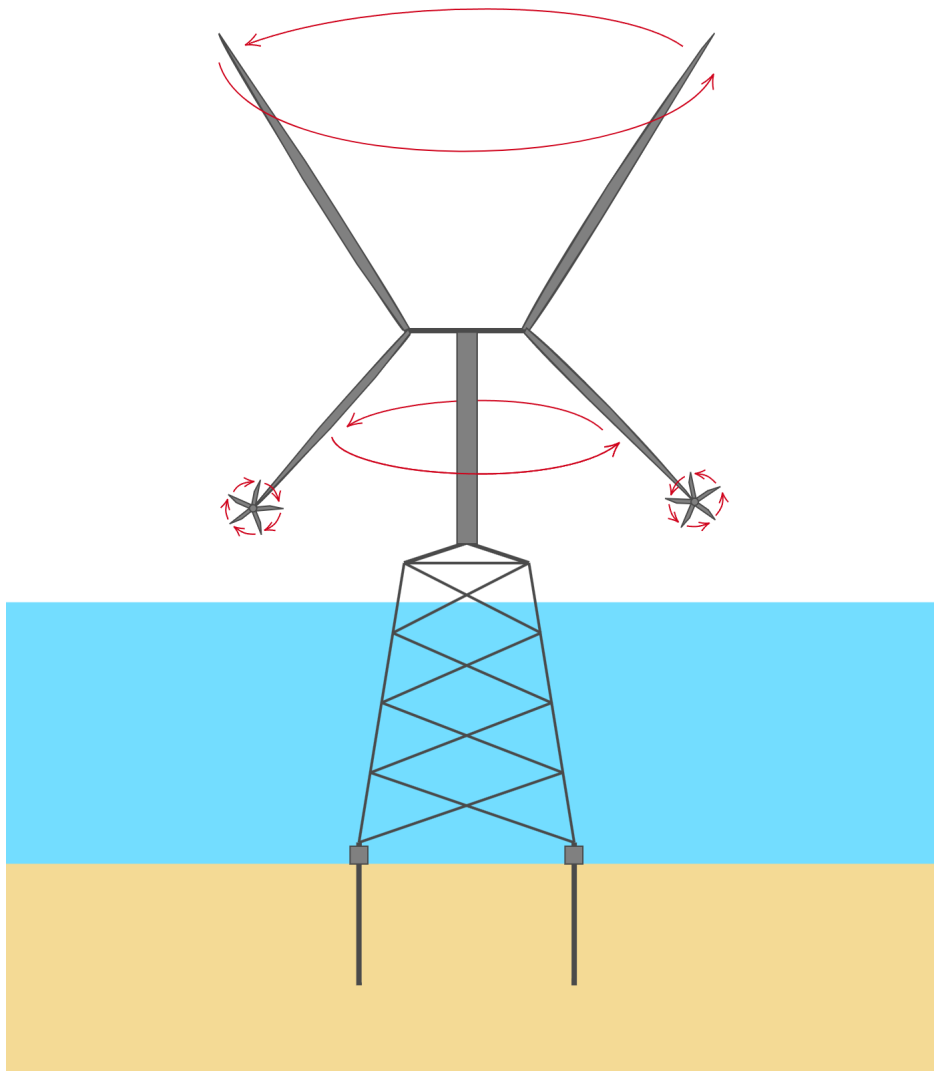


Figure 2.1: Sketch of the X-rotor including the turbine, tower, jacket structure and piles. Red arrows showing the rotation direction for the primary and secondary rotors.

The rotor comprises an upper part with two blades in the form of a V and a lower part with two blades in the form of an inverted V. Each lower blade of the main rotor has an additional rotor, known as a secondary rotor, attached at its end. The upper and lower blades on the primary rotor have a length of 100 m and 65 m respectively, and the secondary rotor has a radius of 4.7

m. The rated wind speed for the turbine is 12.5 m/s, at which the turbine achieves its designated maximum power output. The upper part of the X-rotor primarily extracts mechanical power from the wind, while the lower half serves to reduce the overturning moment, support the secondary rotors, and enhance mechanical power extraction. The secondary rotors are responsible for driving generators and generating electrical power.

The design of the X-rotor takes a departure from conventional horizontal axis turbines, where upscaling typically follows an increasing trend in blade length and size. Instead, upscaling in the X-rotor is achieved by either attaching two secondary turbines to each lower primary blade or increasing the number of primary blades from four to six, with one secondary rotor positioned on each lower blade[1].

2.1.1 Jacket structure

The choice of foundation type for offshore wind turbines becomes critical as water depths increase. For depths exceeding 40 m, jacket structures supported on multiple foundations have gained prominence over monopiles[16]. Four-legged jacket structures offer several advantages over their three-legged counterparts. These include larger angles between the legs and braces, facilitating improved manufacturing detailing. Furthermore, the presence of four legs enables a smoother transfer of loads into the seabed, enhancing the overall stability and performance of the structure[13]. As an initial reference design, the Upwind jacket structure, to host a typical 5.0 MW horizontal axis wind turbine, is chosen. To develop the finite element model of the X-Rotor's substructure, the dimensions of the Upwind jacket reference structure are initially adopted, with modifications to suit the slightly higher rated power surpassing 5 MW and increase loading as the of the X-Rotor in primary a vertical axis wind turbine (VAWT)[1]. It should be emphasized that this is only an initial design, not the optimal one.

As the X-rotor primarily works as a VAWT the rotor creates large lateral loads which cause significant overturning moments in comparison to the horizontal-axis wind turbine (HAWT). This loading situation could be compared to the HAWT being started up and shut down with every rotation of the blades. As a consequence, the stresses in the X-rotor jacket structure primarily result from the aerodynamic loading, the rotation of the primary blades leads to a wide variation in loading. Consequently, wind-induced loads exert a significant level of damage on the X-rotor jacket structure compared to the wave loads¹.

The X-rotor jacket shown in Figure 2.2 features four legs interconnected by bracings, with four crossed bracing at varying heights. These bracings are fixed to the legs using K-joints, although they may be classified as Y-joints in certain load cases. The classification of the joints is discussed further in Section 2.8.3.

The jacket's material is steel, and the properties and geometry of the beams are shown in Table 2.1. Structural damping of the jacket, transition piece and tower is considered with a stiffness proportional component of 0.01. This is a simplification that leads to a stiffer structure than in reality. The shear coefficient, which accounts for the shear deformation and warping effects in thin-walled beams[4], is set to zero. Originally the jacket is anchored to the ground with piles however, in the model, this is simplified by fixing the bottom nodes of the jacket.

In this thesis, any mention of 'diameter' will consistently refer to the outer diameter.

¹This statement is sourced from an unpublished presentation about the X-rotor project at the Wind Energy Science Conference (WESC) 2023 by Michael Muskulus.

Table 2.1: X-rotor jacket structure properties

| Symbol | Parameter | Value |
|--------|-------------------|---------------------------|
| E | Young's modulus | 210 GPa |
| ν | Poisson's ratio | 0.03 |
| ρ | Density | 7 825.0 kg/m ³ |
| g | Gap in leg joints | 0.7 m |
| t | Brace thickness | 0.06 m |
| d | Brace diameter | 1.00 m |
| T | Chord thickness | 0.11 m |
| D | Chord diameter | 1.83 m |

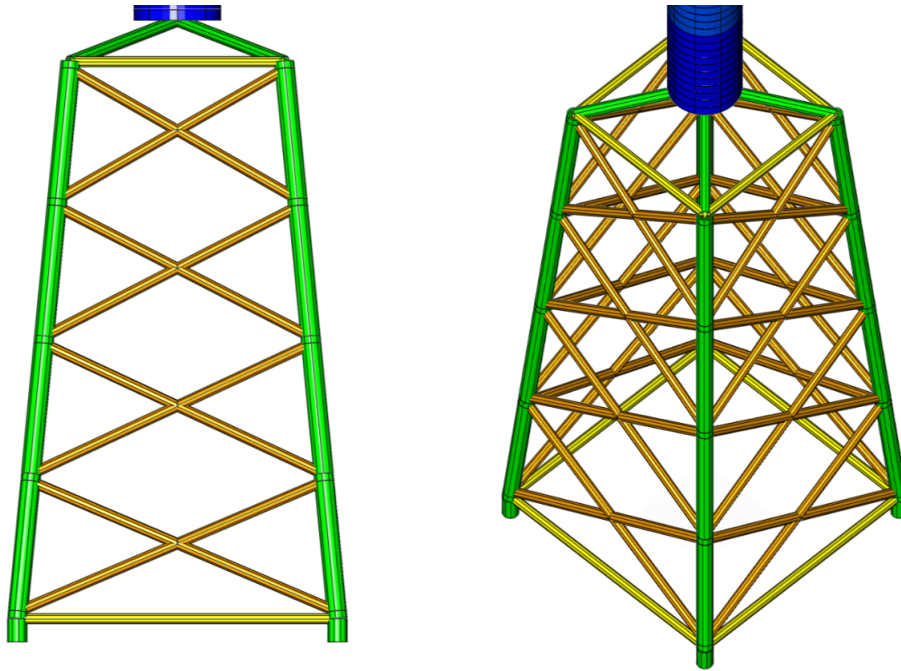


Figure 2.2: Jacket structure for the X-rotor visualized in FEDEM Windpower[12].

2.1.2 Environment

The jacket structure is placed at a mean sea level of 40 m. A representative North Sea site is chosen to define the wind and wave loads, site number 15 "North Sea Center" from Table 1 in "Joint Distribution of Environmental Condition at Five European Offshore Sites for Design of Combined Wind and Wave Energy Devices" [20]. The technical report X-rotor design basis - WP4 Design of Mechanical Structure and Analysis represents different simulation events corresponding to different sea states and wind conditions[6]. The wind direction is defined as the red arrow in Figure 2.3, where the loads from the wind are transferred to the structure through the tower top.

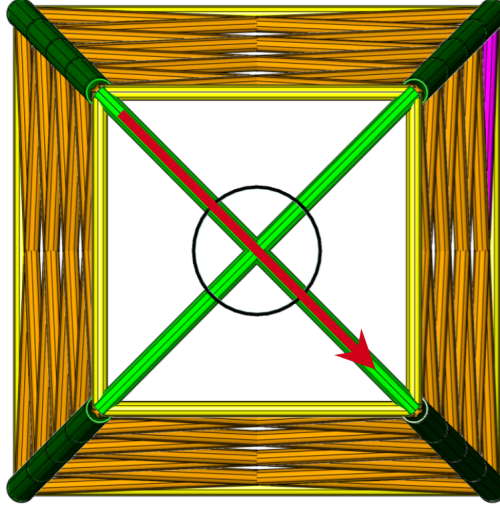


Figure 2.3: The jacket structure from above, visualized in FEDEM[12]. The wind direction is shown as a red arrow. Beam 82 which has a vital role in this report is shown in pink.

2.2 Sensitivity of a response function

When performing a structure analysis, the response $\mathbf{u}(b_i)$ of the structure exposed to external and internal loads determines the design through response functions F , such as the forces and stresses. The response functions depend on all system properties, where one such property or variable is noted as b_i . The relationship between these properties is given in Equation 2.1.

$$F(b_i) = G(\mathbf{u}(b_i), b_i) \quad (2.1)$$

The response function is influenced by variable b_i in both explicit and implicit ways, the latter being due to its dependence on the response $\mathbf{u}(b_i)$. As a result, to calculate the sensitivity of a response function with respect to the design variable, as demonstrated in Equation 2.2, the chain rule is used[31].

$$\frac{dF}{db_i}(b_i) = \frac{\partial G}{\partial b_i}(\mathbf{u}(b_i), b_i) + \frac{\partial G}{\partial \mathbf{u}}(\mathbf{u}(b_i), b_i) \frac{d\mathbf{u}}{db_i}(b_i) \quad (2.2)$$

In this thesis, the derivative of the response with respect to time, such as velocity and acceleration, is denoted with a dot. On the other hand, differentiation with respect to structural properties, denoted as b_i , is expressed with $\frac{d}{db_i}$.

2.3 Direct differentiation method

To determine the sensitivity of the response functions, as Equation 2.2 indicates, the sensitivity of the response must first be established, which is generally unknown. This can be accomplished using the direct differentiation method, which determines the sensitivity of the response implicit through the equation of motion (EOM)[31].

The EOM of a multi-degree-of-freedom dynamic system under random excitation with mass, damping, and stiffness matrix; \mathbf{M} , \mathbf{C} , \mathbf{K} is given by Equation 2.3. The system has a displacement \mathbf{u} , velocity $\dot{\mathbf{u}}$ and acceleration $\ddot{\mathbf{u}}$ when it is exposed to an external load \mathbf{R} [5]. All of these components are or can be dependent on the property b_i , even though this dependency is not included in the following equations.

$$\mathbf{M}\ddot{\mathbf{u}} + \mathbf{C}\dot{\mathbf{u}} + \mathbf{K}\mathbf{u} = \mathbf{R} \quad (2.3)$$

In the direct differentiation method, the sensitivity of the response $\frac{d\mathbf{u}}{db_i}(b_i)$ is computed by differentiating the EOM with respect to the property b_i using the product rule[31] as provided in Equation 2.4.

$$\frac{d\mathbf{M}}{db_i}\ddot{\mathbf{u}} + \mathbf{M}\frac{d\ddot{\mathbf{u}}}{db_i} + \frac{d\mathbf{C}}{db_i}\dot{\mathbf{u}} + \mathbf{C}\frac{d\dot{\mathbf{u}}}{db_i} + \frac{d\mathbf{K}}{db_i}\mathbf{u} + \mathbf{K}\frac{d\mathbf{u}}{db_i} = \frac{d\mathbf{R}}{db_i} \quad (2.4)$$

Equation 2.4 can be rearranged to a new EOM, where the displacements, velocity and acceleration are the differentiation of the original response, responding to Equation 2.5.

$$\mathbf{M}\frac{d\ddot{\mathbf{u}}}{db_i} + \mathbf{C}\frac{d\dot{\mathbf{u}}}{db_i} + \mathbf{K}\frac{d\mathbf{u}}{db_i} = \underbrace{\frac{d\mathbf{R}}{db_i}}_{\text{external force}} - \underbrace{\left(\frac{d\mathbf{M}}{db_i}\ddot{\mathbf{u}} + \frac{d\mathbf{C}}{db_i}\dot{\mathbf{u}} + \frac{d\mathbf{K}}{db_i}\mathbf{u}\right)}_{\text{internal force}} \quad (2.5)$$

Time integration is required to calculate the sensitivity of the response from Equation 2.5. To reduce the computational costs, the following assumptions are made to simplify the problem[25]:

1. Assuming quasi-static analysis: $\ddot{\mathbf{u}} = \dot{\mathbf{u}} = \frac{d\ddot{\mathbf{u}}}{db_i} = \frac{d\dot{\mathbf{u}}}{db_i} = \mathbf{0}$
2. External forces are assumed independent of the sensitivity, which means they do not change with b_i : $\frac{d\mathbf{R}}{db_i} = \mathbf{0}$

This results in the EOM in Equation 2.5 being reduced to Equation 2.6, which corresponds to a quasi-static load case where the structure is exposed to a pseudo load $-\frac{d\mathbf{K}}{db_i}\mathbf{u}(b_i)$.

$$\mathbf{K}\frac{d\mathbf{u}}{db_i} = -\frac{d\mathbf{K}}{db_i}\mathbf{u}(b_i) \quad (2.6)$$

Solving the pseudo-problem where the structure is exposed to the pseudo load gives the pseudo response $\frac{d\mathbf{u}}{db_i}$ [31]. This implies that the change in the response due to a change in a design variable can be found by applying a pseudo load to the original structure.

2.3.1 First-order Taylor expansion

The Taylor Series is a mathematical method used to represent a function as an infinite sum of terms. These terms are calculated based on the function's derivatives at a single point[18].

It is the gradient of the response concerning a change in the design variable b_i that is found in the pseudo problem, however, from this slope, the response for the variable $b_i + \Delta b_i$ can be found according to the first-order Taylor expansion, as an example this is shown for a function f in Equation 2.7.

$$f(b_i + \Delta b_i) \approx f(b_i) + \frac{df}{db_i}(b_i) \Delta b_i \quad (2.7)$$

2.4 Euler-Bernoulli beam element

Structural analysis is carried out using the Euler-Bernoulli beam theory. This theory makes a fundamental assumption that the cross-section plane is infinitely rigid, implying that shear deformations are neglected and no deformations occur in the cross-section plane. Consequently, this theory only applies to slender beam elements[3]. The beam properties are presented in Table 2.2, and the relation between E-modulus, shear modulus and Poisson's ratio is given in Equation 2.8.

Table 2.2: Beam properties of an Euler-Bernoulli beam element

| Symbol | Parameter |
|--------|--|
| A | Cross-section area |
| I_y | Second moment of area about the y-axis |
| I_z | Second moment of area about the z-axis |
| J | St. Venant torsional constant |
| L | Length of the beam in x-direction |
| E | Young's modulus |
| G | Shear modulus |
| ν | Poisson's ratio |

$$G = \frac{E}{2(1 + \nu)} \quad (2.8)$$

2.4.1 Stiffness matrix in 2D

The stiffness matrix of an Euler-Bernoulli beam element in 2D is given in Equation 2.9 where the axial stiffness matrix and bending stiffness matrix are added together[4]. The corresponding degrees of freedom (DOFs) order is $[v_x^1, v_y^1, \theta_z^1, v_x^2, v_y^2, \theta_z^2]$ and the beam element is defined in Figure 2.4.



Figure 2.4: 2D beam element with DOFs in node 1 and 2.

$$\mathbf{K} = \frac{EI}{L^3} \begin{bmatrix} 0 & 0 & 0 & 0 & 0 & 0 \\ 0 & 12 & -6L & 0 & -12 & -6L \\ 0 & -6L & 4L^2 & 0 & 6L & 2L^2 \\ 0 & 0 & 0 & 0 & 0 & 0 \\ 0 & -12 & 6L & 0 & 12 & 6L \\ 0 & -6L & 2L^2 & 0 & 6L & 4L^2 \end{bmatrix} + \frac{EA}{L} \begin{bmatrix} 1 & 0 & 0 & -1 & 0 & 0 \\ 0 & 0 & 0 & 0 & 0 & 0 \\ 0 & 0 & 0 & 0 & 0 & 0 \\ -1 & 0 & 0 & 1 & 0 & 0 \\ 0 & 0 & 0 & 0 & 0 & 0 \\ 0 & 0 & 0 & 0 & 0 & 0 \end{bmatrix} \quad (2.9)$$

2.4.2 Stiffness matrix in 3D

In 3D the DOFs that are considered is translation v_{axis}^{node} and rotation θ_{axis}^{node} around all three axes. This means axial deformation, torsion and bending about the y- and z-axis. Figure 2.5 shows a 3D tubular beam element.

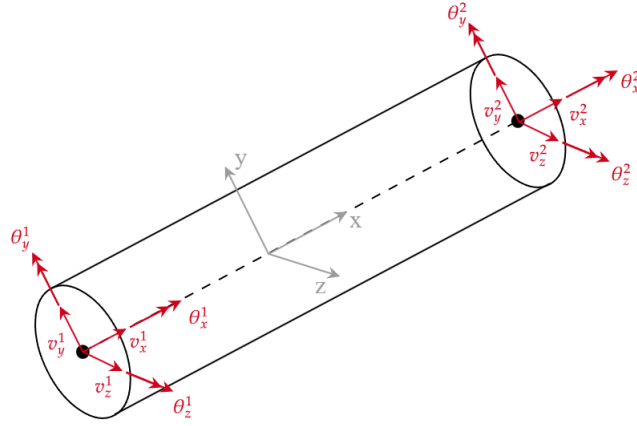


Figure 2.5: 3D beam element with local coordinate system and DOFs in node 1 and 2.

Equation 2.10 shows the stiffness matrix of a 3D Euler-Bernoulli beam element expressed in terms of axial stiffness A^* , bending stiffness I^* around the z- and y-axis and torsional stiffness T^* defined in Equation 2.11. With the order of DOFs as the following vector interprets $[v_x^1, v_y^1, v_z^1, \theta_x^1, \theta_y^1, \theta_z^1, v_x^2, v_y^2, v_z^2, \theta_x^2, \theta_y^2, \theta_z^2]$ [17].

$$\mathbf{K} = \begin{bmatrix} A^* & 0 & 0 & 0 & 0 & 0 & -A^* & 0 & 0 & 0 & 0 & 0 \\ 0 & 12I_z^* & 0 & 0 & 0 & 6LI_z^* & 0 & -12I_z^* & 0 & 0 & 0 & 6LI_z^* \\ 0 & 0 & 12I_y^* & 0 & -6LI_y^* & 0 & 0 & 0 & -12I_y^* & 0 & -6LI_y^* & 0 \\ 0 & 0 & 0 & T^* & 0 & 0 & 0 & 0 & 0 & -T^* & 0 & 0 \\ 0 & 0 & -6LI_y^* & 0 & 4L^2I_y^* & 0 & 0 & 0 & 6LI_y^* & 0 & 2L^2I_y^* & 0 \\ 0 & 6LI_z^* & 0 & 0 & 0 & 4L^2I_z^* & 0 & -6LI_z^* & 0 & 0 & 0 & 2L^2I_z^* \\ -A^* & 0 & 0 & 0 & 0 & 0 & A^* & 0 & 0 & 0 & 0 & 0 \\ 0 & -12I_z^* & 0 & 0 & 0 & -6LI_z^* & 0 & 12I_z^* & 0 & 0 & 0 & -6LI_z^* \\ 0 & 0 & -12I_y^* & 0 & 6LI_y^* & 0 & 0 & 0 & 12I_y^* & 0 & 6LI_y^* & 0 \\ 0 & 0 & 0 & -T^* & 0 & 0 & 0 & 0 & 0 & T^* & 0 & 0 \\ 0 & 0 & -6LI_y^* & 0 & 2L^2I_y^* & 0 & 0 & 0 & 6LI_y^* & 0 & 4L^2I_y^* & 0 \\ 0 & 6LI_z^* & 0 & 0 & 0 & 2L^2I_z^* & 0 & -6LI_z^* & 0 & 0 & 0 & 4L^2I_z^* \end{bmatrix} \quad (2.10)$$

$$A^* = \frac{EA}{L}, \quad I_y^* = \frac{EI_y}{L^3}, \quad I_z^* = \frac{EI_z}{L^3}, \quad T^* = \frac{GJ}{L} \quad (2.11)$$

2.4.3 Stresses in an Euler-Bernoulli beam element

The nominal stresses, from axial load N and moments M_y and M_z about the y-axis and z-axis, in an Euler-Bernoulli beam element, are given by Equation 2.12 [4]. The stresses for the bending moments are the maximum stress in the cross-section appearing at the outer radius.

$$\sigma_x = \frac{N}{A}, \sigma_{my} = \frac{M_y}{I_y}r, \sigma_{mz} = \frac{M_z}{I_z}r \quad (2.12)$$

2.5 Geometrical stiffness

Geometrical stiffness corresponds to the stiffness contribution due to the change in geometry of a structural element when it is subjected to loading. This is especially significant when the structure undergoes large displacements, rotations, or changes in configuration. It is included in the EOM as shown in Equation 2.13. The geometrical stiffness establishes an interaction between axial and bending displacements as the matrix, known as the consistent geometric stiffness matrix, in Equation 2.14 shows where the bending DOFs are connected to the axial load N for 2D beam element[5].

$$\mathbf{M}\ddot{\mathbf{u}} + \mathbf{C}\dot{\mathbf{u}} + \mathbf{K}\mathbf{u} + \mathbf{K}_G\mathbf{u} = \mathbf{R} \quad (2.13)$$

$$\mathbf{K}_G = \frac{N}{30L} \begin{bmatrix} 0 & 0 & 0 & 0 & 0 & 0 \\ 0 & 36 & 3L & 0 & -36 & 3L \\ 0 & 3L & 4L^2 & 0 & -3L & -L^2 \\ 0 & 0 & 0 & 0 & 0 & 0 \\ 0 & -36 & -3L & 0 & 36 & -3L \\ 0 & 3L & -L^2 & 0 & -3L & 4L^2 \end{bmatrix} \quad (2.14)$$

When performing the direct differentiation method the geometrical stiffness should be taken into consideration, however since the matrix does not depend on the cross-section properties of the beam it will not affect the pseudo-problem other than that it must be assumed that the axial load does not change as the cross-section properties change.

2.6 The flexibility method

The flexibility method is a numerical technique used in structural analysis to determine the stiffness matrix of a structure. The stiffness matrix is the inverse of the flexibility matrix, which is obtained by applying a series of unit loads to the structure and performing a static structural analysis. This method is beneficial for complex structures where analytical solutions are difficult to obtain. It allows for accurate numerical solutions of the behaviour of the system. Furthermore, it is useful when the stiffness matrix is interesting but unknown for the structure, as in many finite element analysis (FEA) software programs. However, it is sensitive to rounding errors[4] as it involves taking the inverse of a big matrix. Therefore the resultant stiffness matrix should be examined to identify if these effects occur.

From the generalized Hooke's law, the relation between the flexibility matrix \mathbf{F} , forces \mathbf{R} and response \mathbf{u} can be obtained as shown in equation 2.15 [4].

$$\begin{aligned}\mathbf{R} &= \mathbf{K} \mathbf{u} \\ \mathbf{u} &= \mathbf{K}^{-1} \mathbf{R} = \mathbf{F} \mathbf{R}\end{aligned}\tag{2.15}$$

A unit load is applied separately to each DOF of the structure to obtain the flexibility matrix, while all other loads are zero. This results in a set of displacement values, which can be used to determine the column of the flexibility matrix corresponding to the DOF number. The complete flexibility matrix can be constructed by repeating this process for all DOFs.

Equation 2.16 shows these steps carried out for DOF i where flexibility column \mathbf{F}_i is obtained. This indicates that the load applied in the current DOF not necessarily needs to be a unit load; it can be scaled by any factor as long as the resulting displacements are divided by the load magnitude. Furthermore, this normalisation step ensures that the resulting entries in the flexibility matrix represent the flexibility of the structure in the corresponding DOFs, regardless of the magnitude of the applied loads.

$$\begin{aligned}\mathbf{u} &= \mathbf{F} [0 \quad \dots \quad 0 \quad R_i \quad 0 \quad \dots \quad 0]^T \\ \mathbf{F}_i &= \frac{\mathbf{u}}{R_i}\end{aligned}\tag{2.16}$$

This is further described and visualised in Section 3.1 for two vertical beams. The stiffness matrix can then be found from the inverse of the flexibility matrix as Equation 2.17 states[4].

$$\mathbf{F} = \mathbf{K}^{-1}\tag{2.17}$$

2.7 Coordinate transformation

In structural analysis, it is often necessary to transform between different coordinate systems, particularly the global and local coordinate systems. This is because the global coordinate system is typically used to define the overall geometry and boundary conditions of a structure, whereas the local coordinate system is used to define the properties and behaviour of individual structural elements. Coordinate transformation is therefore required to analyze the response of a structure accurately. This allows the contributions of each element to the overall structural response to be correctly combined.

2.7.1 Rotation matrix

To perform the coordinate transformation, a rotation matrix is used to relate the local coordinate system to the global coordinate system[17].

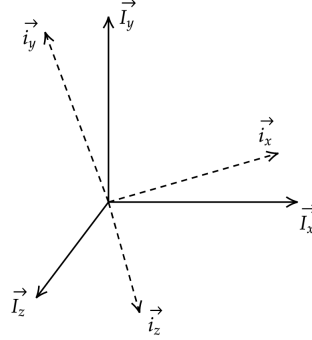


Figure 2.6: Unit vectors of the global coordinate system \mathbf{I} and the local coordinate system \mathbf{i} .

The rotation matrix in 3D to transform from the global to the local coordinate system is composed of the unit vectors of the local system expressed in the global system as derived from Equation 2.18. The local coordinate unit vectors are noted as \mathbf{i} , and the global coordinate vectors are noted as \mathbf{I} as defined in Figure 2.6. The unit vectors of the global system constitute the identity matrix[17].

$$\begin{bmatrix} \mathbf{i}_x \\ \mathbf{i}_y \\ \mathbf{i}_z \end{bmatrix} = \mathbf{R} \begin{bmatrix} \mathbf{I}_x \\ \mathbf{I}_y \\ \mathbf{I}_z \end{bmatrix} = \mathbf{R} \begin{bmatrix} 1 & 0 & 0 \\ 0 & 1 & 0 \\ 0 & 0 & 1 \end{bmatrix} = \mathbf{R} \quad (2.18)$$

2.7.2 Transformation matrix of a 3D beam element

A transformation matrix is employed to convert the 12 DOFs of a 3D beam element, as defined in Section 2.4, from the global to the local coordinate system. This matrix can also convert other properties like the stiffness matrix. The transformation matrix applies the rotation matrix to the three translation and rotation DOFs at each node separately. The transformation matrix \mathbf{T} is defined in Equation 2.19 where $\mathbf{0}$ represents a 3x3 matrix filled with zeros.

$$\mathbf{T} = \begin{bmatrix} \mathbf{R} & \mathbf{0} & \mathbf{0} & \mathbf{0} \\ \mathbf{0} & \mathbf{R} & \mathbf{0} & \mathbf{0} \\ \mathbf{0} & \mathbf{0} & \mathbf{R} & \mathbf{0} \\ \mathbf{0} & \mathbf{0} & \mathbf{0} & \mathbf{R} \end{bmatrix} \quad (2.19)$$

2.7.3 Identification of unit vectors

Once the global coordinate system for the structure and the local coordinate system for an element is defined but unit vectors are unknown, the rotation matrix between them can be obtained using dot and scalar products.

To obtain the rotation matrix for a local coordinate system, it is necessary to have some information about the direction of one axis and the plane of another. In Figure 2.7, the local x-axis direction

is defined in the direction of vector \mathbf{b} , while the y-axis is required to be in the plane defined by vector \mathbf{a} and \mathbf{b} . To find the local y-axis, the projection of \mathbf{a} onto \mathbf{b} is subtracted from \mathbf{a} to obtain the remaining part that is orthogonal to \mathbf{i}_x and in the \mathbf{ab} plane. The vector projection is shown in Equation 2.20 [10]. It should be mentioned that all the vectors are defined in the global coordinate system.

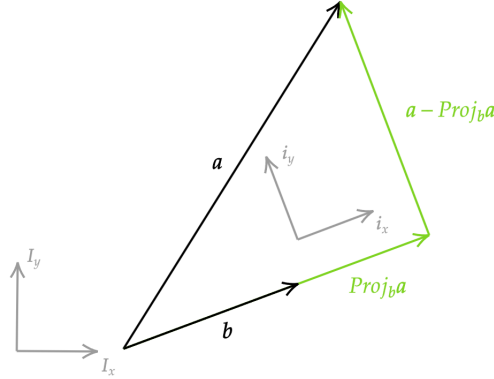


Figure 2.7: Projection of \mathbf{a} onto \mathbf{b}

$$Proj_b \mathbf{a} = \frac{\mathbf{a} \cdot \mathbf{b}}{|\mathbf{b}|^2} \mathbf{b} \quad (2.20)$$

The unit vectors are found by normalizing these two vectors in the x- and y-direction. The z-axis is orthogonal to these two vectors and defined by the cross product of \mathbf{i}_x and \mathbf{i}_y [10].

$$\begin{aligned} \mathbf{i}_x &= \frac{\mathbf{b}}{|\mathbf{b}|} \\ \mathbf{i}_y &= \frac{\mathbf{a} - Proj_b \mathbf{a}}{|\mathbf{a} - Proj_b \mathbf{a}|} \\ \mathbf{i}_z &= \mathbf{i}_x \times \mathbf{i}_y \end{aligned} \quad (2.21)$$

2.8 Fatigue limit state of welded joints in a jacket structure

The limit state of a steel structure is not solely a function of high stresses but is also influenced by cyclic stresses that generate cracks and propagate them, ultimately resulting in fatigue failure. The primary driving constraint in an offshore wind turbine jacket is usually fatigue damage. Thus this will dictate the lifetime of the structure. Critical sections for fatigue damage of a jacket structure are the welded joints[14]. The tubular beams of the jacket are connected as Y-, K- and X-joints. The fatigue damage should be evaluated in these welded joints according to DNV's Recommended Practice for Fatigue Design of Offshore Steel Structures, DNVGL-RP-C203 [9].

2.8.1 Hot spot stress approach

According to the guidelines for a tubular joint, eight equally distributed points around the cross-section should be evaluated. These are so-called hot spot stresses (HSS), the geometric stress at the respective point. The HSS is derived by scaling the nominal stresses according to the location

of the hot spot within the joint. It should be mentioned that these eight evaluated spots are not necessarily the points with maximum stresses in the cross-section[14]. The stresses that are considered in a tubular joint are a superposition of the nominal axial stress of the brace $\sigma_{x,b}$ from the axial load N and the nominal stresses from moments about the y- and z-axis in the brace beam, σ_{my} and σ_{mz} which according to the coordinate system in Figure 2.8 is referred to as the out-of-plane moment M_{OP} and in-plane moment M_{IP} . In addition, the chord stresses from the axial load N^{chord} and in-plane moment are included M_{IP}^{chord} [9].

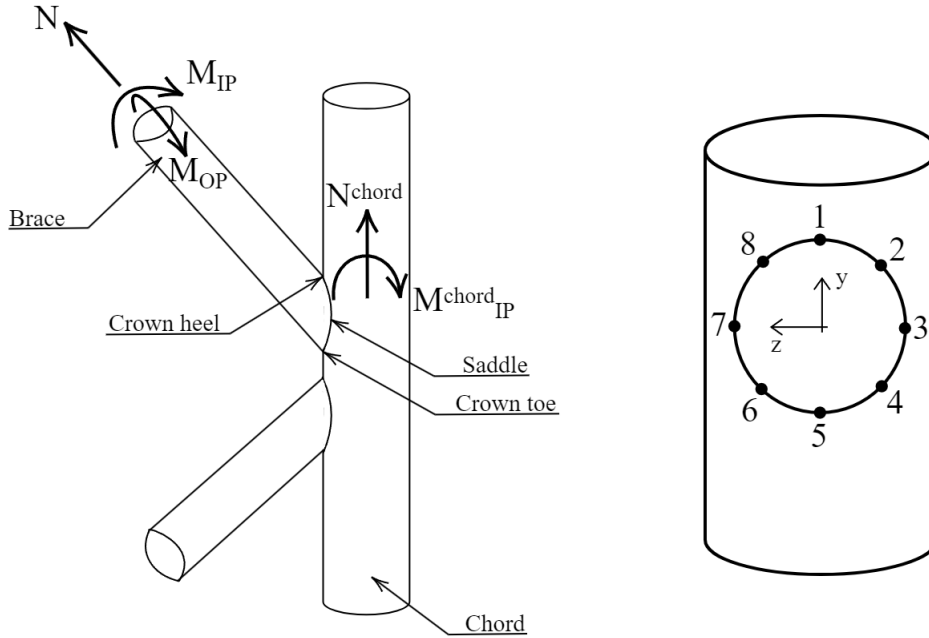


Figure 2.8: Geometry of a welded K-joint including the loads and moments considered in the design for the brace and chord. The hot spot placements are also defined from 1 to 8.

2.8.2 Stress concentration factors

For design purposes, the geometry and thickness of the connected tubular beams are considered in the stresses through SCFs at the brace and chord side of the joint. The brace and chord connection are classified as a Y- K- or X-joint depending on the geometry, and load situation of the respective joint. The SCF is an important consideration in the design of welded tubular joints in offshore structures, as it can significantly affect the fatigue life of the joint. Therefore, accurate estimation of the SCF is essential to ensure the safety and reliability of the structure[9]. This will be discussed further in Section 4. The HSS, including the SCFs, are given in Equation 2.22 where the SCFs are given by the empirical formulas from Appendix B in DNVGL-RP-C203 [9]. For axial loading, the SCFs are SCF_{AS} and SCF_{AC} , respectively for the saddle and crown hot spot. As for moment in-plane and out-of-plane, it is SCF_{MIP} and SCF_{MOP} .

The standard also states that if the chord has significant dynamic axial stresses, the HSS at the crown toe and heel (HSS 1 and HSS 5) should consider these stresses. This is done by adding the stresses in the axial direction of the chord multiplied with an SCF of 1.20. The chord stresses considered are the in-plane moment M_{IP}^{chord} and axial load N^{chord} , as shown in Figure 2.8.

$$\begin{aligned}
\sigma_1 &= SCF_{AC} \sigma_{x,b} + SCF_{MIP} \sigma_{my} + 1.20 (\sigma_{Nchord} + \sigma_{MIP}^{chord}) \\
\sigma_2 &= \frac{1}{2} (SCF_{AC} + SCF_{AS}) \sigma_{x,b} + \frac{\sqrt{2}}{2} SCF_{MIP} \sigma_{my} - \frac{\sqrt{2}}{2} SCF_{MOP} \sigma_{mz} \\
\sigma_3 &= SCF_{AS} \sigma_{x,b} + SCF_{MOP} \sigma_{mz} \\
\sigma_4 &= \frac{1}{2} (SCF_{AC} + SCF_{AS}) \sigma_{x,b} - \frac{\sqrt{2}}{2} SCF_{MIP} \sigma_{my} - \frac{\sqrt{2}}{2} SCF_{MOP} \sigma_{mz} \\
\sigma_5 &= SCF_{AC} \sigma_{x,b} - SCF_{MIP} \sigma_{my} + 1.20 (\sigma_{Nchord} + \sigma_{MIP}^{chord}) \\
\sigma_6 &= \frac{1}{2} (SCF_{AC} + SCF_{AS}) \sigma_{x,b} - \frac{\sqrt{2}}{2} SCF_{MIP} \sigma_{my} + \frac{\sqrt{2}}{2} SCF_{MOP} \sigma_{mz} \\
\sigma_7 &= SCF_{AS} \sigma_{x,b} - SCF_{MOP} \sigma_{mz} \\
\sigma_8 &= \frac{1}{2} (SCF_{AC} + SCF_{AS}) \sigma_{x,b} + \frac{\sqrt{2}}{2} SCF_{MIP} \sigma_{my} + \frac{\sqrt{2}}{2} SCF_{MOP} \sigma_{mz}
\end{aligned} \tag{2.22}$$

The stress concentration factors are a function of the chord and brace cross-sectional properties, through τ , β , γ and α defined in Equation 2.23.

$$\tau = \frac{t}{T}, \quad \beta = \frac{d}{D}, \quad \gamma = \frac{D}{2T}, \quad \alpha = \frac{2L}{D} \tag{2.23}$$

The SCFs are calculated on the chord and brace side of the joint, where the largest one is chosen to determine the HSS to be on the safe side.

2.8.3 Joint classification of joints at the jacket legs

The SCFs depend on the geometry and load situation. The joints between the legs and braces of the jacket have the geometry of a K-joint, one in each direction of two nearby legs. As the DNV standard states brace planes within angles smaller than 15° can be considered as individual braces. Although the joints possess the shape of a K-joint, they may be classified as a Y-joint depending on the load situation. Appendix B in DNVGL-RP-C203 outlines that if within 10 % of the brace axial load is balanced out by the connected brace it is classified as a K-joint. If the load is transferred to the leg instead of the connected brace, it will be classified partly as a Y-joint, it is then a combination called a KY-joint. Unless no load is taken by the connected brace, then it is classified as a Y-joint, as if the connected brace is not there. The load component perpendicular to the chord direction is compared, which is dependent on the angle of the brace. The moment SCFs follows the axial load classification. This classification criterion is shown in Figure 2.9.

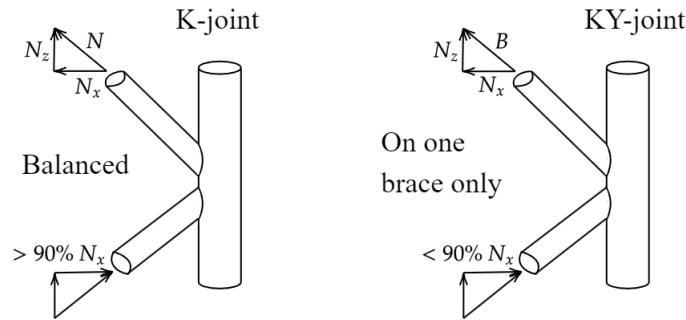


Figure 2.9: Joint classification of a K shape joint dependent on the load balancing.

If the connected brace balances less than 90 % of the considered brace load it is classified as a KY-joint. The SCFs are then a combination of the K- and Y-joint SCFs, where the percent K-joint is defined as how many percent of the brace load is transferred to the connected brace. This is described in Equation 2.24.

$$K\% = \frac{\text{connected brace load}}{\text{brace load}} \cdot 100\% \quad (2.24)$$

$$Y\% = 100\% - K\%$$

2.8.4 Fatigue damage

The Palmgren-Miner rule is used to predict the fatigue life of the jacket structure subjected to quasi-periodic loading. The basic idea behind the rule is that the total damage caused by a cyclic loading history can be expressed as the sum of the damage caused by each cycle, provided that the loading amplitudes are small enough such that the material behaviour remains linear[22].

According to the Palmgren-Miner rule, the cumulative fatigue damage in a structural part subjected to multiple cyclic loads can be obtained by summation of ratios between the number of cycles endured n_j and the corresponding cycles to failure N_j for the number of stress blocks, k . Rainflow counting, described in Section 2.9, is used to obtain the number and magnitude of stress ranges in the load history.

The number of cycles to failure is found from an S-N curve which describes the logarithmic relationship between applied stress range $\Delta\sigma_j$ and the number of cycles to failure N_j . This curve is generated through experimental testing and is specific to the material and loading conditions under consideration[23]. The S-N curve for tubular joints in an offshore steel structure is shown in Figure 2.10.

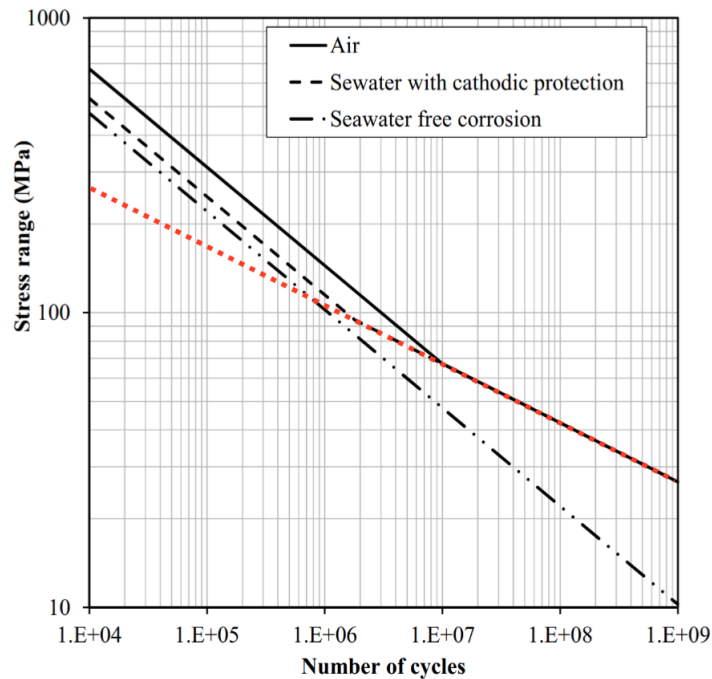


Figure 2.10: S-N curve for tubular joints, Figure 2.10 in DNVGL-RP-C203, including the linear assumption (red dashed line) chosen to simplify the damage expression. [9]

The accumulated damage D is calculated by Palmgren Miner's rule in Equation 2.25. The accumulated damage must be lower than the usage factor $\eta = \frac{1}{DFF}$. The design fatigue factor (DFF) depends on the type accessibility and inspection plan[9]. The d_j factor scales the damage to represent the entire lifetime of the component, assuming the same loading conditions will continue, and account for the probability of occurrence of that load case, p [26].

$$D = \sum_{j=1}^k d_j \frac{n_j}{N_j} \leq \eta \quad (2.25)$$

To be able to describe the damage directly in terms of the stresses, the S-N curve is simplified by looking at a single slope, which makes the relation between $\log(N_j)$ and $\log(\Delta\sigma_j)$ linear. The slope that is chosen is the curve used for lower stress ranges, this will give a conservative number of cycles to failure for higher stress ranges, as this gives higher damage. In Figure 2.10, this is the curve where N_j is larger than $1.8 \cdot 10^6$ is marked as the red dashed line. Using this simplification, the N_j can be expressed in terms of the stress range as represented in Equation 2.26 [9].

$$\log N_j = \log \bar{a} - m \log(\Delta\sigma_j) \Rightarrow N_j = \frac{\bar{a}}{(\Delta\sigma_j)^m} \quad (2.26)$$

The constant $\log \bar{a}$ is the intercept of the S-N curve with the $\log N$ x-axis, and constant m is the inverse slope of the S-N curve. These are dependent on the chosen S-N curve[23]. The accumulated damage in Equation 2.27 is then expressed in terms of the stress ranges.

$$D = \frac{DFF}{\bar{a}} \sum_{j=1}^k d_j n_j (\Delta\sigma_j)^m \leq 1 \quad (2.27)$$

2.9 Rainflow counting

Rainflow counting is a method used to extract fatigue cycles from a time series of stress or strain data. It involves identifying the ranges and applying a counting algorithm to calculate the number of cycles at different stress amplitudes. ASTM E1049-85 standard practices for cycle counting in fatigue analysis are used to determine the number of cycles, n_i a given stress range $\Delta\sigma_i$ have during a load sequence. This is done briefly according to the following four steps:

1. Identify local maxima and minima: The first step is identifying all the local maxima and minima in the time series data. A local maximum is a data point higher than its neighbouring points, and a local minimum is a data point lower than its neighbouring points.
2. Identify half cycles: The data segments between consecutive maxima and minima.
3. Merge half cycles: In this step, some half-cycles are merged to form complete cycles. When a positive half-cycle, going from a minimum to a maximum, is combined with a negative half-cycle, going from a maximum to a minimum, it creates a complete cycle. This is done for the stress ranges "inside" a larger stress range. Figure 2.11 shows this as the green cycles. The algorithm checks each half-cycle to see if it meets this criterion. The previous cycle counting continues past these full cycles as the orange dotted lines in Figure 2.11 illustrated as they pass these green cycles and count the next smaller minimum or larger maximum.
4. Count cycles: The remaining cycles are counted and categorised by mean stress and range. The mean stress is the average stress of the cycle, and the range is the difference between the maximum and minimum stress of the cycle[2].

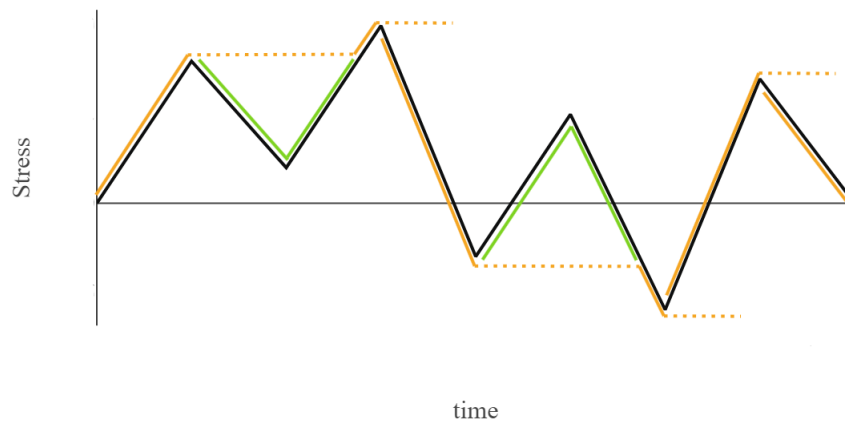


Figure 2.11: Sketch of rainflow counting with orange half cycles and green full cycles.

The flow chart in Figure 2.12 shows how the algorithm in MATLAB goes through all extremums and counts the cycles, and corresponding stress ranges[29].

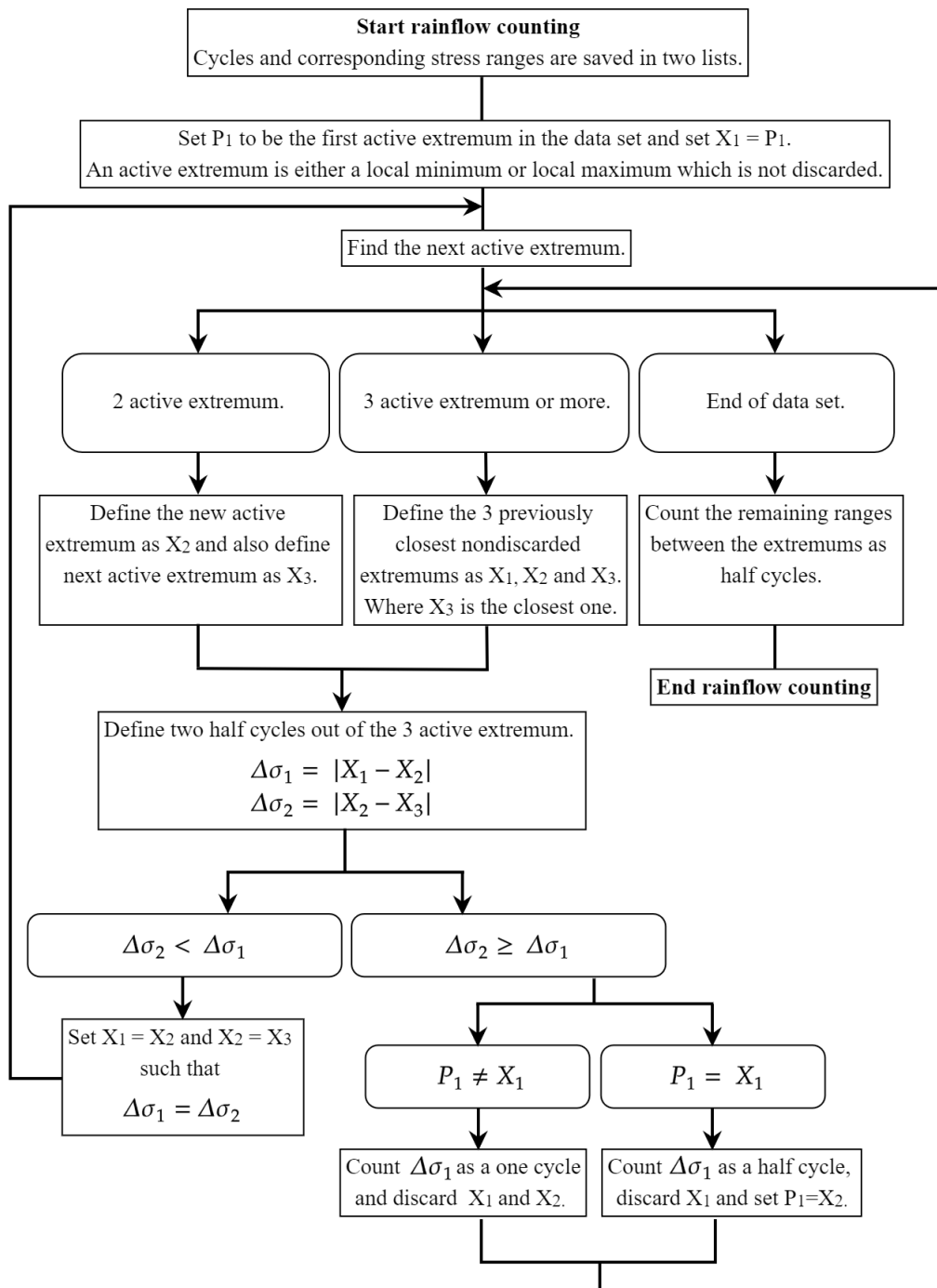


Figure 2.12: Flow chart of rainflow count according to ASTM E1049-85 algorithm

Considering the stress cycles in Figure 2.11 and using the algorithm presented in flow chart in Figure 2.12 to identify the stress ranges and cycles gives the count shown in Figure 2.13.

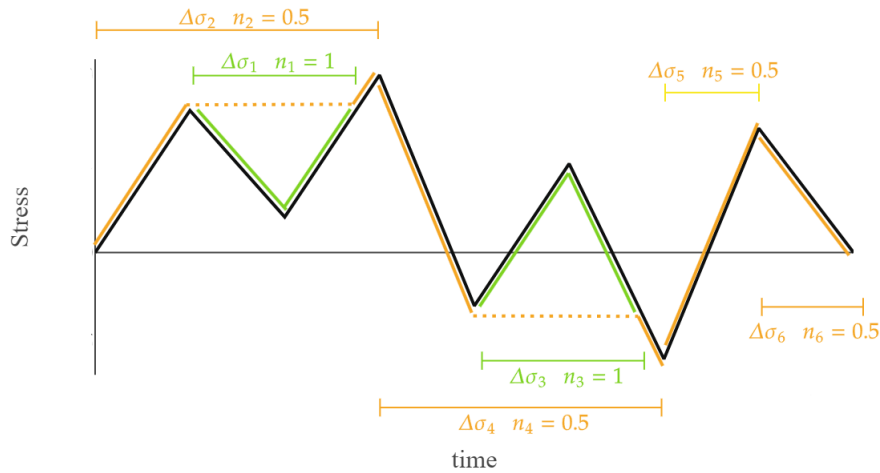


Figure 2.13: Sketch of how the full cycles and half cycles are counted using rainflow counting according to the flow chart in Figure 2.12.

2.10 Establishment and differentiation of functions utilizing the least square method

The least square method is an optimisation technique that aims to find the best-fit curve to data points by minimising the sum of the squares of the differences between the observed and predicted values[18].

When dealing with power functions involving negative or fractional exponents, the least squares method can be used for accurate curve fitting. By applying a logarithmic scale, we can transform the power function into a linear equation. Equation 2.28 demonstrates how the power function f dependent on the variable x and constants a and b , can be converted into a linear equation by taking the logarithm on both sides[18].

$$f(x) = ax^b \Rightarrow \log(f(x)) = \log(a) + b\log(x) \quad (2.28)$$

The function $f(x)$ is transformed into a linear relationship between $\log(f(x))$ and $\log(x)$. This enables the application of the least squares method to estimate the coefficients accurately. The slope of the resulting line corresponds to the exponent b , while the intercept represents $\log(a)$. If an equation consists of terms with different exponential dependencies on x , the least squares method can be applied to each term individually and then combined to give the best-fitted curve.

This approach can be particularly helpful in differentiation when dealing with intricate equations where variables are expressed in terms of several other variables. For example, the SCF functions, where the thickness and diameter are expressed through powers of β , γ , α and τ .

To prevent differentiation errors and facilitate the solution of such intricate functions dependent on x , Equation 2.29 can be employed using the constants a and b obtained in the least square method to approximate the derivative of f with respect to x .

$$\frac{d}{dx}f(x) = abx^{b-1} \quad (2.29)$$

2.11 Offshore environment loads

2.11.1 Wave loads

The JONSWAP spectrum, derived from the Joint North Sea Wave Project, is a widely used model for wind-generated waves in the North Sea. This is because the JONSWAP spectrum considers that the energy in wind-generated waves is concentrated around a dominant frequency. This improved representation of wave behaviour from the Pierson-Moskowitz spectrum has made the JONSWAP spectrum an essential tool for studying wave dynamics in the North Sea and similar environments [15].

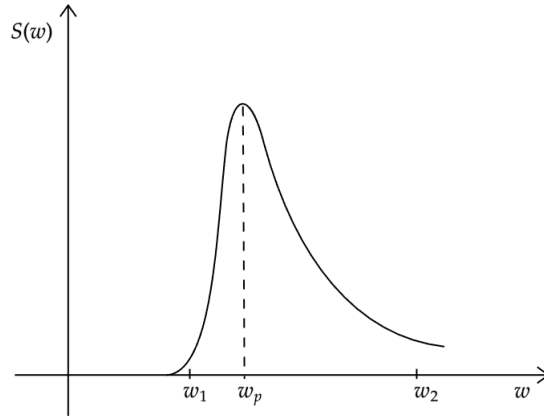


Figure 2.14: JONSWAP spectrum as defined in the Fedem Release 7.2.1 User's Guide [11].

$$w_1 = \frac{2\pi}{T_{high}}, \quad w_p = \frac{2\pi}{T_p}, \quad w_2 = \frac{2\pi}{T_{low}} \quad (2.30)$$

The JONSWAP spectrum is illustrated in Figure 2.14 where the spectrum is expressed in terms of the natural frequency and key parameters in Equation 2.30 where T_{low} and T_{high} are period cut-off values that define the frequency range to be used in the wave spectrum. The parameters given in Table 2.5 define the wave spectrum [11].

Table 2.3: JONSWAP wave spectrum properties as defined in the Fedem Release 7.2.1 User's Guide [11].

| Symbol | Parameter |
|------------|-----------------------------|
| S | Wave spectrum |
| ω | natural frequency |
| T_p | Spectral peak period |
| T_{low} | Lower cut-off period value |
| T_{high} | Higher cut-off period value |
| H_s | Significant wave height |
| σ | Spectral shape parameter |
| γ | Spectral peakedness factor |

The dimensionless frequency parameter, σ , determines the width of the peak in the wave spectrum and is typically defined in two parts, depending on whether the frequency is less than or greater

than the peak natural frequency ω_p . The spectral peakedness factor, γ , measures how sharp or pronounced the peak of the wave spectrum is. In the JONSWAP spectrum, the spectral peakedness factor, also called the peak enhancement factor, is applied to the Pierson-Moskowitz spectrum to better represent the energy distribution of wind-generated waves [21] [7]. This gives Equation 2.31, taken from Section 6.2.1 in FEDEM Release 7.2.1 User's Guide [11].

$$\begin{aligned}
 S(\omega) &= A_\gamma \frac{5}{16} \frac{H_s^2 \omega_p^4}{\omega^5} \exp\left(-\frac{5}{4} \left(\frac{\omega}{\omega_p}\right)^{-4}\right) \gamma^Y \\
 A_\gamma &= 1 - 0.287 \ln(\gamma) \\
 Y &= \exp\left(-\frac{1}{2} \left(\frac{\omega - \omega_p}{\sigma \omega_p}\right)^2\right)
 \end{aligned} \tag{2.31}$$

The JONSWAP spectrum characterises the amplitudes of individual sinusoidal wave components that, when combined, generate a model of irregular waves. The forces due to these sea actions give drag and added mass to the beam elements included in FEDEM based on the Morison equation. A simplified load model valid for slender beams with circular outer cross-sections is used. The drag F_d and added mass F_a forces for a fully submerged beam element are shown in Equation 2.32 [11] with the parameters defined in Table 2.4.

$$\begin{aligned}
 F_d &= \rho_w \cdot \frac{D_d}{2} \cdot L \cdot C_d \cdot (u - u_w) |u - u_w| \\
 F_a &= \rho_w \cdot \pi \cdot \frac{D_d^2}{4} \cdot L \cdot (C_a \dot{u} - C_m \dot{u}_w)
 \end{aligned} \tag{2.32}$$

Table 2.4: Parameter to define the wave loads according to the Morison equation.

| Symbol | Parameter |
|----------|---------------------------------------|
| F_d | Drag force |
| F_a | Added mass force |
| ρ_w | Water density |
| D_d | Drag diameter including marine growth |
| L | Beam length |
| C_d | Drag coefficient |
| C_a | Added mass coefficient |
| u | Structure velocity |
| u_w | Water particle velocity |

The water velocity is defined through the irregular waves in the wave spectrum. For the X-rotor model in FEDEM the drag and added mass coefficients are 1.0. The drag diameter is influenced by the marine growth such that $D_d = D + t_{mg}$. Sea water has a density of 1025 kg/m³.

2.11.2 Marine growth

Marine growth is the accumulation of various aquatic organisms on the surfaces of offshore structures over the years of operation. Marine growth can have multiple effects, including impacts on structural integrity, hydrodynamics, maintenance, and environmental implications [30]. The

accumulation of marine growth increases the structure's weight, thereby exerting additional static stress on its components. This added weight also impacts the structure's dynamic behaviour when exposed to waves and current through drag and added mass [11].

Thus, added mass is included in the structural analysis by adding mass to all structural elements with a centre of gravity between the lower and upper water depth limits for marine growth. For a beam with length L and outer diameter D , the added mass is given by Equation 2.33. This is taken from Section 6.1.2 in the FEDEM Release 7.2.1 User's Guide [11].

$$M_{mg} = \rho_{mg}\pi(D + t_{mg})t_{mg}L \quad (2.33)$$

Table 2.5: Marine growth properties

| Symbol | Parameter |
|-------------|---|
| M_{mg} | Added mass due to marine growth |
| ρ_{mg} | Average mass density of the marine growth |
| z_u | Water depth relative to the mean sea level where the marine growth starts |
| z_l | Water depth relative to the mean sea level where the marine growth end |
| t_{mg} | thickness of the marine growth layer |

When calculating sea action loading, the thickness of marine growth is taken into account through the Morison equation, by increasing the diameter of the beams [11].

2.11.3 Wind loads

To accurately assess the impact of wind on a structure, it is essential to define the wind loads and how they vary with height. In estimating wind speeds at varying heights, a power law wind profile is adopted, given in Equation 2.34 [7].

$$U(z) = U_{10} \left(\frac{z}{10} \right)^\alpha \quad (2.34)$$

The wind speed is defined as the mean wind speed over 10 minutes at a 10 meters height U_{10} , and the roughness of the terrain is taken into consideration in α , which for the position of the X-rotor is set to be 0.1 [6]. The wind speed U can then be extrapolated from 10 meters height and found at any height z .

3 Numerical stiffness matrix

The stiffness matrix plays a vital role in sensitivity analysis; therefore, it should be found accurately. As Section 2.6 states, the flexibility method can be employed to determine the stiffness matrix numerically. The aim is to evaluate the accuracy and applicability of the flexibility method when implemented through FEDEM Windpower.

FEDEM is used to create the structure and apply unit loads to all DOFs in the system individually such that resultant displacements of the nodes correspond to the rows in the flexibility matrix. To derive the precise flexibility matrix, the force-displacement relation should be linear, if not, the flexibility and stiffness matrix depend on the load situation. The hypothesis is that the stiffness of the jacket structure is not dependent on the load magnitudes. Hence a study of whether FEDEM gives a utilisable output for this is done. A FEA software such as FEDEM can model non-linear effects. Therefore finding the flexibility matrix by performing load simulations may be sensitive to the properties of the beam and to which DOF is considered. For example, the displacements could be zero depending on the ratio between the stiffness and load, or other non-linear effects can affect the results.

To verify whether these effects occur, the stiffness matrix calculation is examined in two distinct scenarios – one featuring two vertical beams and another with an inclined beam placed on top of a vertical beam. The inclined beam is examined in addition to the vertical beams because the jacket consists of inclined beams, this can therefore better indicate the method’s accuracy concerning the appearance of non-linear effects. FEDEM uses Euler-Bernoulli beam elements in the FEA. Comparing the results to the analytically derived stiffness of an Euler-Bernoulli beam element as defined in Equation 2.10 gives valuable insights into the reliability and practicality of the flexibility method for stiffness matrix determination in FEDEM windpower.

3.1 Numerical stiffness matrix of a vertical beam in 2D

To understand the flexibility method described in Section 2.6, it is performed on a simple structure in 2D of two vertical beams. The DOFs considered are according to a 2D Euler-Bernoulli beam element defined in Section 2.4.1. The stiffness matrix is found for the two upper nodes. The flexibility method can not be used to establish the stiffness matrix of a fixed node because external loads will not give any displacements in a constrained DOF.

3.1.1 Method

Structural properties

The material of the two beams is steel with an E-modulus of 210 GPa and Poisson’s ratio of 0.3. Both beams have a length of 10 m and a tubular cross-section with an outer diameter of 0.5 m and a thickness of 0.05 m. They are connected with a rigid connection, fixed in all DOFs. The shear coefficient is set to zero. The geometrical stiffness was not turned off in these load cases and will have an effect which is addressed later.

Procedure of the flexibility method

Figure 3.1 shows from left to right the structure, which DOF r_i are considered, and how the components in the flexibility matrix column for DOF 2 are obtained. In addition, it visualises the theory of the flexibility method described in Section 2.6.

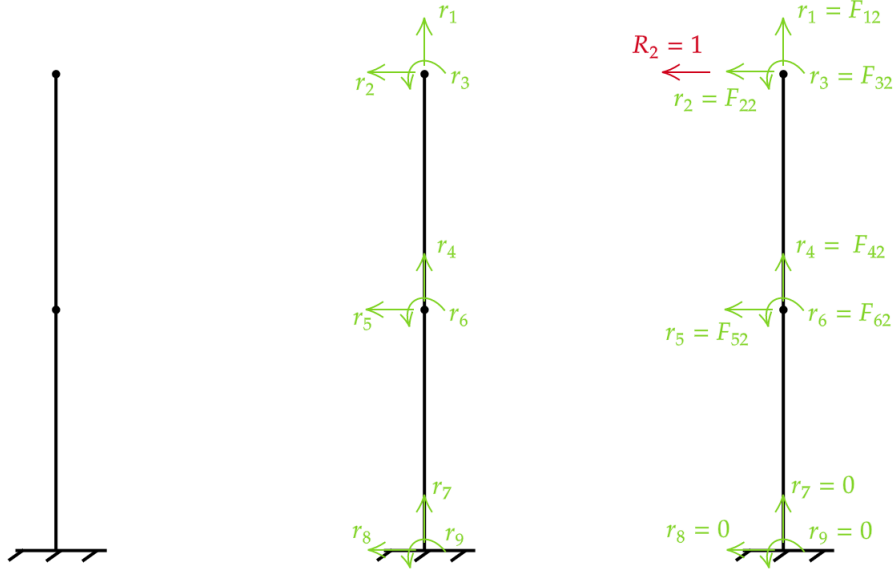


Figure 3.1: Structure of two vertical beams, which DOF r_i are considered, and how the components in the flexibility matrix column for DOF 2 are obtained.

This procedure is applied to all DOFs, and collectively, these constitute a flexibility matrix. Since r_7 , r_8 and r_9 are constrained through the boundary conditions, these will always be zero. The reduced system is shown in Equation 3.1.

$$\begin{bmatrix} r_1 \\ r_2 \\ r_3 \\ r_4 \\ r_5 \\ r_6 \end{bmatrix} = \begin{bmatrix} F_{11} & F_{12} & F_{13} & F_{14} & F_{15} & F_{16} \\ F_{21} & F_{22} & F_{23} & F_{24} & F_{25} & F_{26} \\ F_{31} & F_{32} & F_{33} & F_{34} & F_{35} & F_{36} \\ F_{41} & F_{42} & F_{43} & F_{44} & F_{45} & F_{46} \\ F_{51} & F_{52} & F_{53} & F_{54} & F_{55} & F_{56} \\ F_{61} & F_{62} & F_{63} & F_{64} & F_{65} & F_{66} \end{bmatrix} \begin{bmatrix} R_1 \\ R_2 \\ R_3 \\ R_4 \\ R_5 \\ R_6 \end{bmatrix} \quad (3.1)$$

Load environment

When establishing the flexibility matrix by applying unit loads, the gravity is turned off such that the only load working on the system is the unit load in the applicable DOF. A static structural analysis is performed to obtain the response corresponding to the flexibilities.

Size of loads

When solving this numerically in FEDEM, applying a unit load with magnitude one will not always give reliable results due to numerical approximations of the displacements. Therefore, it is essential to study if the load and displacements have a linear relation. This can be examined by applying unit loads with different factors and comparing the displacements. When using a load or moment larger than 1 N or 1 Nm, the displacement must be divided by the magnitude to give the flexibility elements as shown in Equation 2.16. If the relation is linear, the flexibility components should be the same for all factors. Then all load magnitudes can be used to find the flexibilities. The range where this occurs is called the stable range of flexibility. It is expected that this range will have a slight increase or decrease due to the geometrical stiffness, which is a non-linear effect.

To study the load-displacement relation, unit loads and moments are multiplied by a load factor of 1, 10, 20, 100, 200, 1000, 2000 and 4000 in the DOFs of the upper node. The flexibility components were found and plotted against the applied load magnitude to identify the stable region.

Stiffness matrix

The stiffness matrix is then obtained by choosing flexibility from the stable range for all flexibility columns, constituting the flexibility matrix. The stiffness matrix is then the inverse of this matrix.

3.1.2 Results

The axial, shear and rotational flexibility in node 1 of the upper beam due to axial, shear and rotational loading in node 1 is plotted against each other to determine for which load range the flexibilities are stable. This provides a basis for determining the load size that yields the correct flexibility matrix.

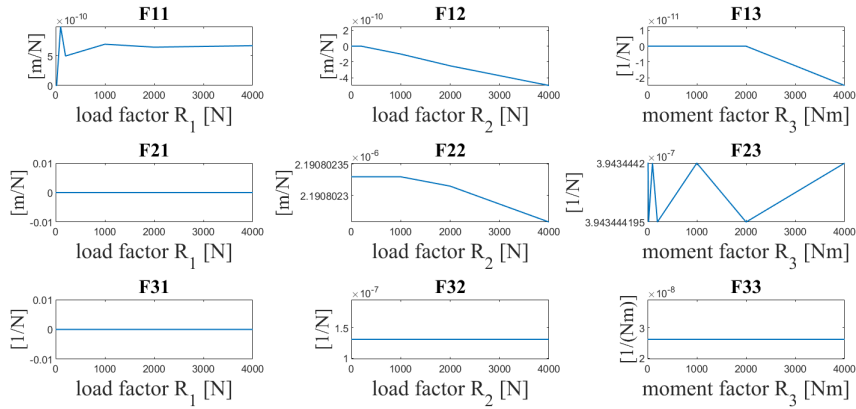


Figure 3.2: Axial, shear and rotational flexibility in node 1 of the upper beam due to axial, shear and rotational loading in node 1. This corresponds to the first 3x3 components of the flexibility matrix.

Based on these stable flexibility ranges and assuming the same ranges hold for node 2, the most accurate numerical stiffness matrix is obtained by combining the flexibility column from 2000 N in R_1 , 1 N in R_2 and 2000 Nm for R_3 . The resultant stiffness matrix is given in Equation 3.2 and compared to the analytical solution of a 2D Euler-Bernoulli beam element in Equation 3.3. The choice of load factors and comparison to the analytical result are provided in the discussion.

$$\mathbf{K}_{numerical} = \begin{bmatrix} 1.4286 & 0 & 0 & -1.4286 & 0 & 0 \\ 0 & 0.0046 & -0.0228 & 0 & -0.0046 & -0.0228 \\ 0 & -0.0228 & 0.1522 & 0 & 0.0228 & 0.0761 \\ -1.4286 & 0 & 0 & 2.9670 & 0 & 0 \\ 0 & -0.0046 & 0.0228 & 0 & 0.0091 & 0 \\ 0 & -0.0228 & 0.0761 & 0 & 0 & 0.3043 \end{bmatrix} * 10^9 \quad (3.2)$$

$$\mathbf{K}_{analytical} = \begin{bmatrix} 1.4844 & 0 & 0 & -1.4844 & 0 & 0 \\ 0 & 0.0046 & -0.0228 & 0 & -0.0046 & -0.0228 \\ 0 & -0.0228 & 0.1522 & 0 & 0.0228 & 0.0761 \\ -1.4844 & 0 & 0 & 2.9688 & 0 & 0 \\ 0 & -0.0046 & 0.0228 & 0 & 0.0091 & 0 \\ 0 & -0.0228 & 0.0761 & 0 & 0 & 0.3043 \end{bmatrix} * 10^9 \quad (3.3)$$

The units of this matrices are [N/m, N/m, Nm, N/m, N/m, Nm] for every row.

3.1.3 Discussion

As the F11 plot in Figure 3.2 shows, applying a unit load of 1 N in the axial direction is too small to give any displacement. The load range where the relation between axial displacement and load is linear is approximately from 1000 N to 4000 N. The plot exhibits a slight increase in the constant interval which as predicted, can be explained by the geometrical stiffness inherent in the system. This can be avoided by excluding the geometrical stiffness in the structural analysis. F21 and F31 plots show no interaction between axial DOF and shear/rotational DOFs for all load factors. This validates the theory of an Euler-Bernoulli beam where there is no interaction between axial and shear stiffness and loads.

The magnitude is essential when applying a shear load R_2 due to this axial and shear interaction. When bending it to fare vertically, it will give a horizontal displacement in the node due to geometrical stiffness. The F12 plot for different load factors of R_2 verifies this. The F22 is also affected by this, giving incorrect flexibility and therefore stiffness. The stable range for the shear load is from 1 N to 100 N.

The same holds for the moment flexibilities where there is no interaction between axial DOF and moment R_3 inside the stable flexibility ranges, from 1 N to 2000 N.

When comparing the analytical and numerical stiffness matrix, it is observed that only the axial stiffness is unequal. The numerical axial stiffness is 96.24 % of the analytical axial stiffness. This means that using the analytical stiffness matrix of a 2D Euler-Bernoulli beam element in the sensitivity analysis would give reasonably accurate results. The disadvantage of using the numerical stiffness matrix is that the flexibility rows are not obtained with the same load factors, such that when having a complex structure of several beams, all DOFs flexibilities should be explored. This is time-consuming, and as the analytical stiffness matrix is almost identical, it will save computational time to use this.

3.2 Finding stiffness matrix and its sensitivity numerically on an inclined beam in 3D

The jacket structure of the X-rotor consists solely of inclined beams. Given this and searching for additional non-linear relationships between loads and displacements within FEDEM, the flexibility method is applied to an inclined beam. This is particularly relevant for the design sensitivity analysis, which requires determining the sensitivity of the stiffness matrix. Hence, this sensitivity is computed for the inclined beam and subsequently compared against the analytical solution. A 3D stiffness matrix is established featuring 6 DOFs in each node, translation and rotation in x-, y- and z-direction as for the Euler-Bernoulli beam element in 3D described in Section 2.4.

3.2.1 Method

Structural properties

The material is the same as the vertical beams, steel with an E-modulus of 210 GPa. As for the vertical beam the gravity and shear reduction coefficients are set to zero. The lower beam has nodes at $(0,0,0)$ and $(0,0,10)$ in the XYZ-coordinate system and a length of 10 m. The upper beam, with a length of approximately 5.1 m, is connected to the lower beam in a rigid connection at $(0,0,10)$ and is free in the top node at $(1,0,15)$. The geometry of the system is shown in Figure 3.3, as well as the definition of the DOFs in the local system in 3D of the inclined beam. The beams only consist of one beam element in the FEA.

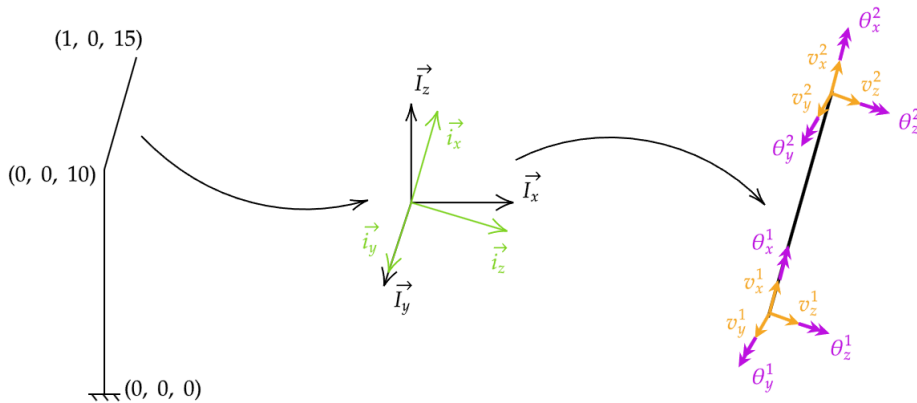


Figure 3.3: Geometry of structure and the angled beam transformed to the local coordinate system.

The beam cross-section is set to be the same as for the braces of the X-rotor, with an outer diameter of 1.00 m and a thickness of 0.06 m. In an inclined beam, the geometrical stiffness could affect the displacements significantly and is therefore turned off. It is then expected to have a linear load-displacement interaction for all load factors unless other non-linear effects are acting.

Load environment

A static analysis is performed as these unit loads should not be affected by any dynamic effect.

Rotation matrix of upper beam

The static analysis provides the global response of the nodes, which is transformed into the local coordinate system of the beam through the transformation matrix as shown in Equation 3.4 dependent on how the local coordinate system is defined.

$$\mathbf{u}_{local} = \mathbf{T}\mathbf{u}_{global} \quad (3.4)$$

For the upper beam, the local x-direction is defined in the length direction of the beam, and the local and global y-axis is equal. From the cross-product of these vectors, the z-axis is defined and the unit vectors, corresponding rotation matrix \mathbf{R} and transformation matrix \mathbf{T} can be obtained. The rotation matrix is shown in Equation 3.5 for the upper beam.

$$\mathbf{R} = \begin{bmatrix} 0.1961 & 0 & 0.9806 \\ 0 & 1 & 0 \\ -0.9806 & 0 & 0.1961 \end{bmatrix} \quad (3.5)$$

Size of loads

The same procedure is followed for the inclined beam as for the vertical beam, where loading factors of 1, 20, 100, 200, 1000, 2000, 10000 and 20000 are applied individually in all DOFs to identify the range of loading factors where the generalized Hooke's law holds. The flexibility components are found according to Section 2.6 in the local coordinate system.

Sensitivity of stiffness matrix

To compare the numerical stiffness matrix to the analytical stiffness matrix, the sensitivity of the stiffness matrix with respect to the thickness is analysed. This results in it only being the contribution from the stiffness of the changed beam that is considered.

Both analytically and numerically, the stiffness matrix of the angled beam is found for a thickness of 0.06 m and 0.05 m. The numerical stiffness matrix is obtained by applying a loading factor of 10000 in all DOFs. To determine the sensitivity of the stiffness matrix with respect to the thickness of the beam, the matrices are subtracted as shown in Equation 3.6.

$$\frac{d\mathbf{K}}{dt} = \frac{\mathbf{K}_{t=0.06} - \mathbf{K}_{t=0.05}}{0.06\text{ m} - 0.05\text{ m}} \quad (3.6)$$

3.2.2 Results

Figure 3.4 shows the flexibility of all DOFs in node 1 is plotted against the load factors of the unit loads in DOF 1 to 3. DOF 1 to 3 are translations in the x-, y-, and z-direction of node 1 and DOF 4 to 6 are rotations in the x-,y- and z-direction of node 1 as defined in Section 2.4.2.

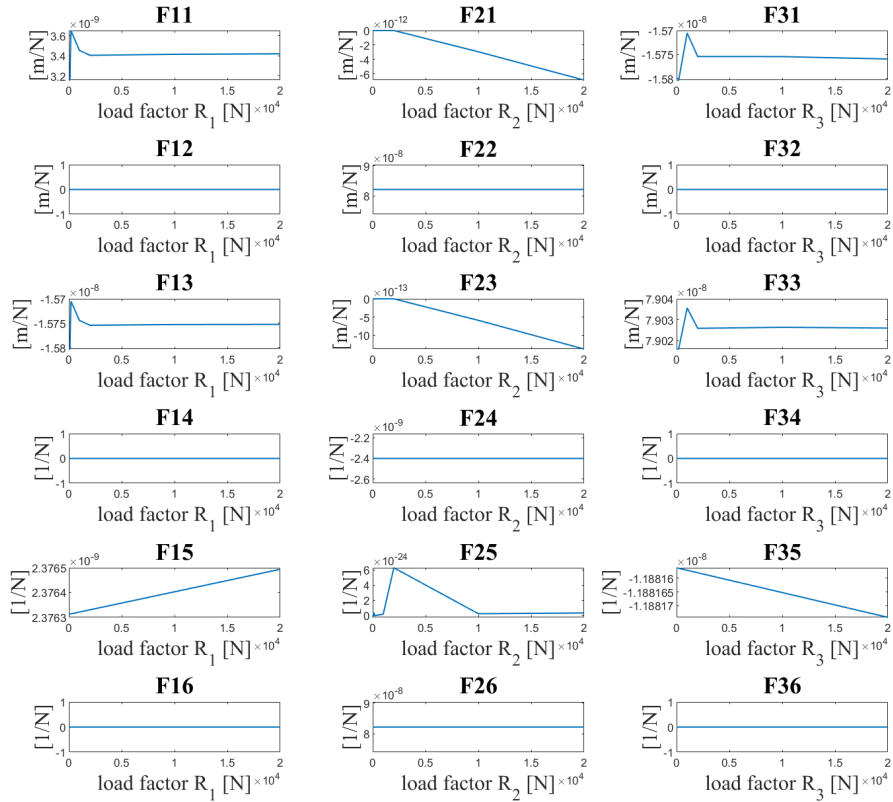


Figure 3.4: Flexibility column of DOF 1 to 3 for DOF 1 to 6, in relationship to the load factor applied.

As F23, F15, and F35 in Figure 3.4 reveals a non-linear affect occurs. All the non-linear flexibility elements are identified and shown for the entire flexibility matrix in Figure 3.5.

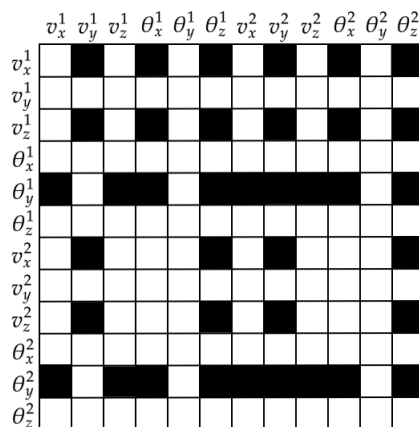


Figure 3.5: Flexibility matrix of the nodes connected to the inclined beam where flexibility elements with a non-linear behaviour are marked in black.

The components that are non-linear exhibit a linear relationship between flexibility and load. Dividing the displacements by the load factor twice, as shown in Equation 3.7, gives a constant relation. This is also illustrated in Figure 3.6 for flexibility component F35.

$$\frac{\mathbf{F}}{|\mathbf{R}|} = \frac{\mathbf{u}}{|\mathbf{R}|^2} = \text{constant} \quad (3.7)$$

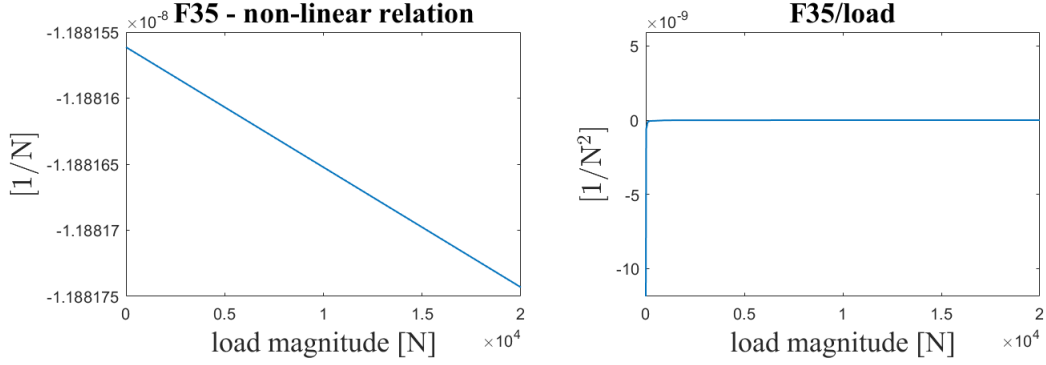


Figure 3.6: Flexibility F35, rotational flexibility in y-direction due to a force in z-direction and the same flexibility component divided by the load factor applied

To compare the analytical and numerical results, the first 7x7 elements of the numerical stiffness matrix sensitivity are shown in Equation 3.8 and the corresponding elements for the sensitivities of the analytical stiffness matrix in Equation 3.9.

$$\frac{d\mathbf{K}_{num}}{dt} = \begin{bmatrix} 1.4335 & 0.0095 & 0.0273 & -0.0005 & -0.0351 & 0.0277 & -1.4032 \\ 0 & 0.0526 & 0 & -0.0000 & 0 & 0.1342 & 0 \\ 0.0030 & -0.0002 & 0.0524 & -0.0000 & -0.1333 & -0.0006 & -0.0027 \\ 0 & 0.0000 & 0 & 0.0877 & 0 & 0.0000 & 0 \\ -0.0077 & -0.0001 & -0.1346 & 0.0000 & 0.4565 & -0.0003 & 0.0070 \\ 0 & 0.1342 & 0 & -0.0000 & 0 & 0.4561 & 0 \\ -1.4337 & -0.0109 & -0.0293 & 0.0005 & 0.0401 & -0.0312 & 1.4033 \end{bmatrix} * 10^{11} \quad (3.8)$$

$$\frac{d\mathbf{K}_{ana}}{dt} = \begin{bmatrix} 1.1515 & 0 & 0 & 0 & 0 & 0 & -1.1515 \\ 0 & 0.0526 & 0 & 0 & 0 & 0.1342 & 0 \\ 0 & 0 & 0.0526 & 0 & -0.1342 & 0 & 0 \\ 0 & 0 & 0 & 0.0877 & 0 & 0 & 0 \\ 0 & 0 & -0.1346 & 0 & 0.4561 & 0 & 0 \\ 0 & 0.1342 & 0 & 0 & 0 & 0.4561 & 0 \\ -1.1515 & 0 & 0 & 0 & 0 & 0 & 1.1515 \end{bmatrix} * 10^{11} \quad (3.9)$$

The units of this matrices are [N/m², N/m², N/m², N, N, N N/m²] for every row.

3.2.3 Discussion

Figure 3.4 and 3.5 show that not all flexibility elements have a stable load range. This means that no matter which load factor is used to find the flexibility components, it will be affected by the magnitude of this factor, which will influence the resultant stiffness matrix. It is observed that the only rows where this appears are DOFs in the XZ plane; this is in the plane where the beam is angled. For the rest of the components, the flexibility in the stable area is unaffected by geometrical stiffness and, therefore, constant.

In the sensitivity of the numerical stiffness matrix, there are many non-zero elements compared to the analytical stiffness matrix of an Euler-Bernoulli beam element. However, as for the flexibilities, only the stiffness sensitivity matrix rows that result in non-zero elements not appearing in the analytical matrix are in the XZ plane. These are most likely coming from the non-linear relation $\mathbf{u} = f(\mathbf{R}^2)$ between loads and displacements. Hence when using the flexibility method to determine the numerical stiffness matrix and its sensitivity in a time history of dynamic loading, the numerical stiffness matrix should be determined for every time step, for the governing time step load case, as the flexibility depends on the loading.

As the stiffness matrix is found from the inverse of the flexibility matrix, it is sensitive to rounding errors due to the inverse found from the division of the elements in the flexibility matrix. Dividing by a small number from numerical or non-linear effects can significantly affect the stiffness matrix.

The non-zero components in the analytical stiffness components are accurate to the corresponding numerical stiffness components, despite the axial stiffness. As for the vertical beam, the axial stiffness is different numerically and analytically. The numerical axial stiffness sensitivity is 124.49 % and 121.86 % of the analytical one for nodes 1 and 2 respectively. This can result in minor displacements, and using the analytical stiffness sensitivity will yield undersized response sensitivities.

3.3 Stiffness matrix sensitivity of the beams in X-rotor jacket structure

X-rotor jacket structure is modelled in FEDEM windpower with Euler-Bernoulli beam elements, using one element for each beam in the FEA, however, as detected when performing the flexibility method on an angled beam in Section 3.2 the stiffness matrix is affected by a non-linear relationship between the loads and displacement and the axial stiffness is different. The same behaviour is expected for the X-rotor stiffness matrix and its sensitivity as it is modelled with the same beam properties. To verify this it is performed on beam 82 which is later considered in the damage sensitivity analysis as a decision basis for how accurately the sensitivities can be determined from the analytical stiffness matrix.

3.3.1 Method

Geometry

Beam 82, one of the lower braces in the jacket structure, is considered. It is shown as the pink beam in Figure 4.1. It has a length of 16.32 m, a diameter of 1.00 m, and a thickness of 0.06 m. The remaining structural properties of the beams are defined in Table 2.1 and Section 2.1.1.

The local coordinate system is defined by the local x-direction in the direction of the beam length and the local y-axis in the plane of the jacket legs. Using the identification of the unit vectors as described in Section 2.7.3 the rotation matrix is established and shown in Equation 3.10.

$$\mathbf{R}_{beam\ 82} = \begin{bmatrix} -0.0373 & -0.9151 & 0.4016 \\ 0.0846 & -0.4033 & -0.9112 \\ -0.9957 & 0.0000 & -0.0925 \end{bmatrix} \quad (3.10)$$

Load environment

The same procedure as for the inclined beam is performed where the geometrical stiffness contribution is not considered and a static analysis is performed. Load factors of 1000 kN and 1000 kNm are applied in the unit loads and moments of all DOFs in the local coordinate system to determine the flexibility matrix.

Sensitivity of stiffness matrix

To compare the sensitivity of the stiffness matrix numerically and analytically it is found with respect to a change in the beam thickness from 0.06 m to 0.05 m according to Equation 3.6.

3.3.2 Results

The resultant numerical and analytical stiffness matrix sensitivity with respect to the thickness is given with one decimal in 10^8 in respectively Equations 3.11 and 3.12.

$$\frac{d\mathbf{K}_{num}}{dt} = \begin{bmatrix} 390.0 & 0.1 & -0.3 & 0.1 & 0.4 & 0.6 & -390.5 & 0.1 & 0.2 & 2.0 & 0.8 & 2.1 \\ 0 & 2.0 & 0 & 0 & -0.2 & 15.0 & 0.1 & -1.8 & 0 & -0.1 & -0.1 & 14.9 \\ 0 & 0 & 2.0 & 0 & -15.0 & 0 & 0 & 0 & -2.0 & 0 & -15.0 & 0.1 \\ 0 & 0 & 0 & 29.7 & 0 & 0 & 0 & 0 & 0 & -29.7 & 0 & 0 \\ 0 & 0 & -15.0 & 0 & 151.6 & 0 & -0.1 & -0.1 & 15.0 & 0 & 74.3 & -0.1 \\ 0 & 15.0 & 0 & 0 & 0 & 151.6 & 0 & -15.0 & 0 & 0 & 0 & 74.3 \\ -390.7 & 0.1 & 0.3 & 0.3 & -0.1 & -1.3 & 389.7 & -1.9 & -0.2 & -3.2 & -0.5 & -4.2 \\ -0.5 & -1.5 & 0 & 0.5 & 0.9 & -16.9 & -2.2 & -3.6 & -0.1 & -3.4 & 1.0 & -20.5 \\ 0.5 & 0 & -2.0 & 0 & 15.1 & -0.4 & -0.6 & -0.6 & 1.9 & 0.7 & 14.8 & -1.3 \\ -0.1 & 0 & 0 & -29.7 & 0 & 0 & 0.1 & 0 & 0 & 29.5 & 0.1 & 0.2 \\ -0.1 & 0 & -15.0 & 0 & 74.3 & 0 & -0.1 & -0.1 & 15.0 & 0.2 & 151.5 & -0.2 \\ 0 & 15.0 & 0 & 0 & -0.4 & 74.3 & 0.1 & -14.9 & 0 & -0.1 & -0.1 & 151.5 \end{bmatrix} \cdot 10^8 \quad (3.11)$$

$$\frac{d\mathbf{K}_{ana}}{dt} = \begin{bmatrix} 390.3 & 0 & 0 & 0 & 0 & 0 & -390.3 & 0 & 0 & 0 & 0 & 0 \\ 0 & 2.0 & 0 & 0 & 0 & 15.4 & 0 & -2.0 & 0 & 0 & 0 & 15.4 \\ 0 & 0 & 2.0 & 0 & -15.4 & 0 & 0 & 0 & -2.0 & 0 & -15.4 & 0 \\ 0 & 0 & 0 & 29.7 & 0 & 0 & 0 & 0 & 0 & -29.7 & 0 & 0 \\ 0 & 0 & -15.4 & 0 & 154.6 & 0 & 0 & 0 & 15.4 & 0 & 77.3 & 0 \\ 0 & 15.4 & 0 & 0 & 0 & 154.6 & 0 & -15.4 & 0 & 0 & 0 & 77.3 \\ -390.3 & 0 & 0 & 0 & 0 & 0 & 390.3 & 0 & 0 & 0 & 0 & 0 \\ 0 & -2.0 & 0 & 0 & 0 & -15.4 & 0 & 2.0 & 0 & 0 & 0 & -15.4 \\ 0 & 0 & -2.0 & 0 & 15.4 & 0 & 0 & 0 & 2.0 & 0 & 15.4 & 0 \\ 0 & 0 & 0 & -29.7 & 0 & 0 & 0 & 0 & 0 & 29.7 & 0 & 0 \\ 0 & 0 & -15.4 & 0 & 77.3 & 0 & 0 & 0 & 15.4 & 0 & 154.6 & 0 \\ 0 & 15.4 & 0 & 0 & 0 & 77.3 & 0 & -15.4 & 0 & 0.7 & 0 & 154.6 \end{bmatrix} \cdot 10^8 \quad (3.12)$$

The units of this matrices are $[\text{N}/\text{m}^2, \text{N}/\text{m}^2, \text{N}/\text{m}^2, \text{N}, \text{N}, \text{N}, \text{N}/\text{m}^2, \text{N}/\text{m}^2, \text{N}/\text{m}^2, \text{N}, \text{N}, \text{N}]$ for every row.

3.3.3 Discussion

The X-rotor jacket structure is composed of numerous inclined beams. Due to the non-linear effects that arise when applying the flexibility method to the inclined beam in FEDEM, as discussed in section 3.2.3, utilizing the analytical stiffness matrix of a 3D Euler-Bernoulli beam element would yield accurate results as it demonstrates strong agreement with the numerical stiffness matrix. However, the axial stiffness differs between numerical and analytical methods, and using the numerical axial stiffness will provide more precise load and stress values, particularly when axial loads are large.

An alternate approach to ascertain the stiffness matrix numerically is the displacement method, often referred to as the stiffness method. Individually applying unit displacements to each DOF determines the stiffness of the system. Nevertheless, its integration within finite element software is not straightforward and can lead to a significant increase in computational demand.

Several factors advocate for using the analytical stiffness matrix to determine the sensitivity of the stiffness matrix in the X-rotor jacket structure. Firstly, calculating the axial stiffness numerically requires the computation of the entire flexibility matrix, which demands considerable computational resources. Secondly, the process for determining sensitivity involves subtracting two stiffness matrices. In theory, this operation should be conducted for each incremental change in the considered variable to ensure accurate results. Therefore, using the analytical stiffness matrix significantly reduces the number of necessary calculations. Lastly, as discussed in Section 3.2.3, employing the numerical stiffness matrix enables the consideration of non-linear effects. However, the computational cost of determining the stiffness matrix at each time step does not justify the marginal increase in precision. This is particularly relevant given the high degree of accuracy the analytical stiffness matrix provides.

4 Stress concentration factors

4.1 Joint classification

Given that the X-rotor undergoes a time series of loads and the joint classification depends on the load conditions, it is necessary to classify the joint for each time step and determine the corresponding SCFs at every time step. In this section, the K-joints at the jacket legs are considered. The classification procedure is outlined in Section 2.8.3 where the criteria for joint classification are defined in Figure 2.9.

Geometry

The brace beams that are classified are the braces connected to the right leg in Figure 4.1, which is either K-, Y- or KY-joints dependent on the load situation.

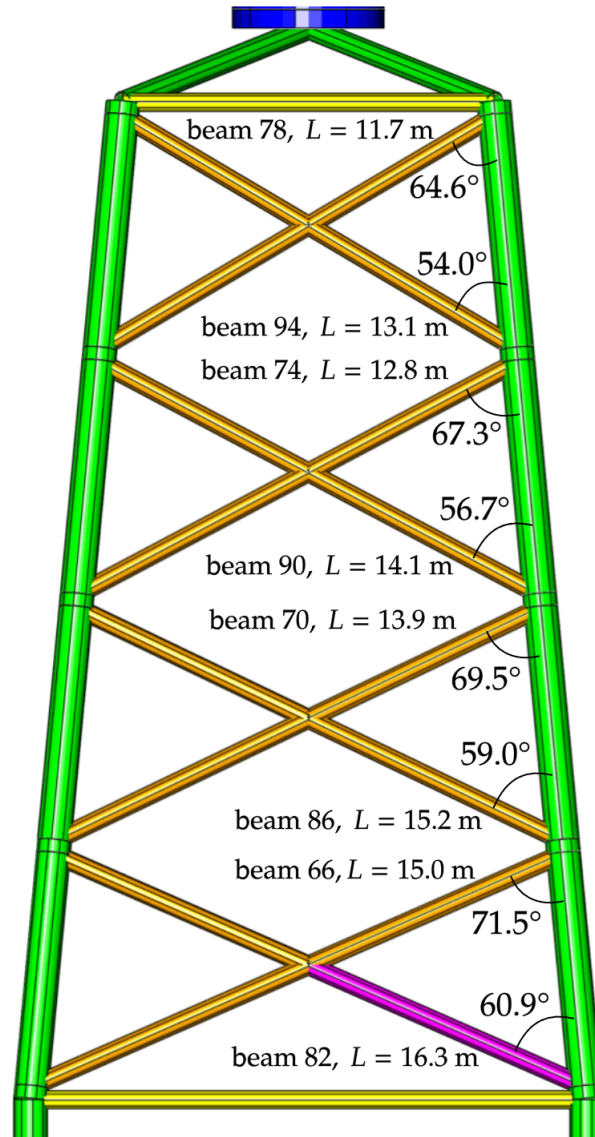


Figure 4.1: The beams considered for joint classification with the corresponding beam length and angle. It is the beams connected to the right leg which is analysed.

Load situation and environment

The structure is exposed to wind, waves, marine growth, and gravity. Two load cases are considered. Firstly a wind speed of 12.0 m/s which is close to the rated wind speed, and secondly, a wind speed of 19.5 m/s, close to the cut-off wind speed. The parameters to define the wind field and wave spectrum for the two load cases are given in Table 4.1 as well as the probability of occurrence p for the load case. As addressed in Section 2.1.1, the damage of the structure is mainly due to wind-induced loads, and the waves are therefore not considered for the high wind speed of 19.5 m/s, such that the water density is set to zero. The wind loads are applied to the structure in the tower top, and the cycles for the different load directions working simultaneously are shown in Figure 5.5 for a time history of 37.7 s, equivalent to 5 rotor rotations. This is the mean wind resultant loading as the turbulence is not considered. The wind loads are provided by Delft University of Technology, a partner in the X-rotor project.

Table 4.1: Variables defining the considered load cases taken from Table 20 in X-rotor design basis - WP4 Design of Mechanical Structure and Analysis [6].

| U_{10} | H_s | T_p | p |
|----------|-------|-------|-------|
| 12 m/s | 2.4 m | 7.3 s | 0.063 |
| 19.5 m/s | 0 | 0 | 0.006 |

The marine growth has a density of 1325 kg/m^3 and a thickness of 60 mm which is applied to all structural members between 2 to 40 meters below mean sea level.

A dynamic structural analysis is performed in FEDEM of 37.7 s. In postprocessing, the brace loads are analysed to determine the percentage of the time steps classified as K-joint. The remaining time steps will then be classified as a KY-joint where the connected brace only partly balances out the load. An example of the beam classification for all timesteps is given in Figure 4.2.

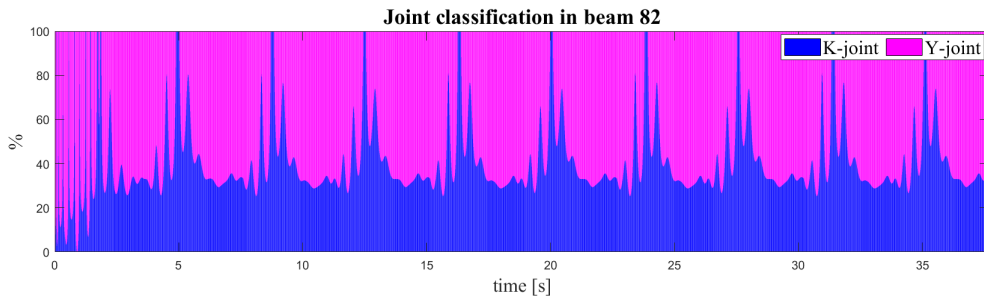


Figure 4.2: Joint classification of beam 82 for a dynamic load case with wind speed 19.5 m/s.

This reveals that for most of the time steps the joint is classified as a KY-joint, as they are a combination of K- and Y-joint. The resultant percentage is presented for all beams in Table 4.2 for the two load cases. Where the percentage includes the overall percentage area of K- and Y-joint in Figure 4.2, such that KY-joint contributes to both K% column and Y% column.

Table 4.2: Joint classification for beams in Figure 4.1 for a wind speed 12.0 m/s and 19.5 m/s

| Beam number | 19.5 m/s | | 12.0 m/s | |
|----------------|----------|-------|----------|-------|
| | K % | Y % | K % | Y % |
| 78 | 96.61 | 3.39 | 97.98 | 2.02 |
| 94 | 73.87 | 26.13 | 58.02 | 41.98 |
| 74 | 72.16 | 27.84 | 90.70 | 9.30 |
| 90 | 69.62 | 30.38 | 75.02 | 24.98 |
| 70 | 79.95 | 20.05 | 83.38 | 16.61 |
| 86 | 62.72 | 37.27 | 62.18 | 37.82 |
| 66 | 78.63 | 21.37 | 73.74 | 26.26 |
| 82 | 40.77 | 59.23 | 21.37 | 78.63 |

The load situations for a K-shaped joint differ in how the load is balanced out as described in Section 2.8.3, if the loads are unbalanced (i.e., not balanced by the connected brace), the tables for the SCFs in Appendix B of DNVGL-RP-C203 refer to the Y-joint SCFs. On the other hand, if they are balanced out, the table offers a K-joint SCF function dependent on the geometry of the connected brace [9].

Table 4.2 reveals that the joints fall into different classes depending on the time step and load case. This should be considered when calculating the HSS for all times and loads. If not, a conservative classification of the joints can be based on the arrangement shown in Equation 4.1 from Appendix B in DNVGL-RP-C203 [9].

$$SCFX > SCFY > SCFK \quad (4.1)$$

The time steps classified as a KY-joint should be considered. As Equation 4.1 shows, this Y-joint classification will yield higher stresses and, therefore damage. The effect of including this will be further analysed for the damage in Section 5.3.

4.2 SCF dependency on the cross-section properties

4.2.1 SCF functions of cross-section properties

The SCFs are functions of the chord thickness T and diameter D , as well as brace thickness t and diameter d . Tables 4.3, 4.4 and 4.5 provide these relations for Y-, X- and K-joints. When these relations are established, all terms that are not powers of the cross-sectional parameter, such as trigonometric functions, are assumed constant. An example of how these are obtained is shown for SCF 2 in Equation 4.2.

$$\begin{aligned}
SCF2(T, t, D, d) &= \gamma^{0.2} \tau (2.65 + 5(\beta - 0.65)^2) + \tau \beta (0.25\alpha - 3) \sin\theta \\
&= \gamma^{0.2} \tau (C + (\beta - C)^2) + \tau \beta (\alpha - C) \\
&= \gamma^{0.2} \tau + \gamma^{0.2} \tau \beta^2 + \gamma^{0.2} \tau \beta + \tau \beta \alpha + \tau \beta \\
&= \frac{D^{0.2} t}{T^{0.2} T} + \frac{D^{0.2} t d^2}{T^{0.2} T D^2} + \frac{D^{0.2} t d}{T^{0.2} T D} + \frac{t d}{T D} + \frac{t d}{T D} \\
&= D^{0.2} T^{-1.2} t + D^{-1.8} T^{-1.2} d^2 t + D^{-0.8} T^{-1.2} d + t T^{-1} D^{-2} d + t T^{-1} D^{-1} d \\
&= f(T^{-1.2}, T^{-1}, t, D^{0.2}, D^{-1.8}, D^{-0.8}, D^{-2}, D^{-1}, d^2, d)
\end{aligned} \quad (4.2)$$

Table 4.3: SCF function dependency on the cross-section properties for Y-joints.

| Stress position | SCF functions of T, t, D, d in Y-joints | SCF |
|--|---|-----|
| Axial load - chord ends fixed | | |
| Chord saddle | $f(T^{-2.1}, t^{1.1}, D, D^{-1}, d, d^2)$ | 1 |
| Chord crown | $f(T^{-1.2}, T^{-1}, t, D^{0.2}, D^{-1.8}, D^{-0.8}, D^{-2}, D^{-1}, d^2, d)$ | 2 |
| Brace saddle | $C + f(T^{-1.52}, t^{0.52}, D^{0.9}, D^{-1.2}, D^{-0.2}, d^{2.1}, d^{1.1})$ | 3 |
| Brace crown | $C + f(T^{-1.2}, T^{-1}, t, D^{1.2}, D^{-0.8}, D^{-2}, D^{-1}, d^2, d)$ | 4 |
| Axial load - general fixity conditions | | |
| Chord saddle | $f(T^{-2.1}, T^{-1}, t^{1.1}, t, D, D^{-3}, D^{-2}, D^{-4}, D^{-1}, d, d^2, d^3)$ | 5 |
| Chord crown | $f(T^{-1.2}, T^{-1}, t, D^{-0.2}, D^{-1.8}, D^{-0.8}, D^{-2}, D^{-1}, d^2, d)$ | 6 |
| Brace saddle | | 3 |
| Brace crown | $C + f(T^{-1.2}, T^{-1}, t, D^{1.2}, D^{-0.8}, D^{-2}, D^{-1}, d^2, d)$ | 7 |
| In-plane bending | | |
| Chord crown | $f(T^{0.68\beta-1.85}, t^{0.85}, D^{-0.68\beta}, d)$ $\stackrel{\beta=0.55}{=} f(T^{-1.48}, t^{0.85}, D^{-0.37}, d)$ | 8 |
| Brace crown | $f(T^{0.77\beta-1.49}, t^{0.4}, D^{0.09-0.77\beta}, d)$ $\stackrel{\beta=0.55}{=} f(T^{-1.07}, t^{0.4}, D^{-0.33}, d)$ | 9 |
| Out-of-plane bending | | |
| Chord saddle | $f(T^{-2}, t, D^{-3}, d, d^4)$ | 10 |
| Brace saddle | $f(T^{-1.41}, t^{0.46}, \dots)$ $\dots D^{-0.05}, D^{-1.05}, D^{-4.05}, D^{-3.05}, D^{-7.05}, d, d^2, d^4, d^5, d^8)$ | 11 |

Table 4.4: SCF function dependency on the cross-section properties for X-joints.

| Stress position | SCF functions of T, t, d, D in X-joints | SCF number |
|--|---|------------|
| Axial load (balanced) | | |
| Chord saddle | $f(T^{-2}, t, D^{-1.8}, d, d^{2.8})$ | 12 |
| Chord crown | $f(T^{-1.2}, T^{-1}, t, D^{0.2}, D^{-1.8}, D^{-0.8}, D^{-1}, d, d^2)$ | 13 |
| Brace saddle | $C + f(T^{-1.5}, t^{0.5}, D^{0.1}, D^{-1.6}, d^{0.9}, d^{2.6})$ | 14 |
| Brace crown | $C + f(T^{-1.2}, D^{1.2}, D^{-0.8}, d^2)$ | 15 |
| In-plane bending | | |
| Chord crown | | 8 |
| Brace crown | | 9 |
| Out-of-plane bending (balanced) | | |
| Chord saddle | $f(T^{-2}, t, D^4, d, d^5)$ | 16 |
| Brace saddle | $f(T^{-1.41}, t^{0.46}, \dots$ $\dots D^{-0.05}, D^{-1.05}, D^{-4.05}, D^{-5.05}, D^{-8.05}, \dots$ $\dots d, d^2, d^5, d^6, d^9)$ | 17 |
| Axial load in one brace only | | |
| Chord saddle | $f(T^{-2.1}, T^{-1}, t^{1.1}, t, \dots$ $\dots D^{-2}, D^{-4}, D^{-3}, D^{-6}, D^{-5}, D^{-7}, D, D^{-1}, \dots$ $\dots d, d^2, d^3, d^4, d^5, d^6)$ | 18 |
| Chord crown | | 6 |
| Brace saddle | $f(T^{-1.52}, t^{0.52} \dots$ $\dots D^{0.9}, D^{-1.2}, D^{-0.2}, D^{-2.1}, D^{-4.2}, D^{-3.2}, \dots$ $\dots d^{2.1}, d^{1.1}, d^3, d^{5.1}, d^{4.1})$ | 19 |
| Brace crown | | 7 |
| Out-of-plane bending on one brace only | | |
| Chord saddle | | 10 |
| Brace saddle | | 11 |

Table 4.5: SCF function dependency on the cross-section properties for K-joints.

| Stress position | SCF functions of T , t , d , D in K-joints | SCF |
|--|--|-----|
| Balanced axial load | | |
| Chord | $f(T^{-1.4}, t^{0.9}, D^{0.5}, D^{-1.5}, D^{-0.5}, D^{0.88}, D^{-1.12}, D^{-0.12}, \dots$ $\dots d, d^2, d^{-0.38}, d^{1.62}, d^{0.62})$ | 20 |
| Brace | $C + f(T^{-1.26}, T^{0.72}, t^{0.76}, t^{-1.22}, \dots$ $\dots D^{0.5}, D^{-1.5}, D^{-0.5}, D^{0.88}, D^{-1.12}, D^{-0.12}, D^{0.25}, \dots$ $\dots D^{-1.75}, D^{-0.75}, D^{0.63}, D^{-1.37}, D^{-0.37}, D^{-1},$ $\dots d, d^2, d^{-0.38}, d^{1.62}, d^{0.62}, d^{0.25}, d^{2.25}, d^{1.25}, d^{-0.13}, d^{1.87}, d^{0.87}, d^{1.5})$ | 21 |
| Unbalanced in-plane bending | | |
| Chord crown | | 8 |
| Brace crown | | 9 |
| Unbalanced out-of-plane bending | | |
| Chord saddle | $f(T^{-2.5}, T^{-2}, t, D^{0.5}, D^{-4}, D^{-3.5}, D^{-0.5}, D^{-4.5}, d, d^4, d^{0.5})$ | 23 |
| Brace saddle | $f(T^{-1.91}, T^{-1.41}, t^{0.46}, \dots$ $\dots D^{-0.05}, D^{-4.05}, D^{0.45}, D^{-3.55}, D^{-0.55}, D^{-4.55}, D^{-1.05}, \dots$ $\dots D^{-5.05}, D^{-1.55}, D^{-5.55}, D^{-8.05}, D^{-7.55}, D^{-8.55}, \dots$ $\dots d, d^4, d^{0.5}, d^2, d^5, d^{1.5}, d^8, d^{4.5})$ | 24 |
| Axial load on one brace only | | |
| Chord saddle | | 5 |
| Chord crown | | 6 |
| Brace saddle | | 3 |
| Brace crown | | 7 |
| In-plane bending on one brace only | | |
| Chord crown | | 8 |
| Brace crown | | 9 |
| Out-of-plane bending on one brace only | | |
| Chord crown | $f(T^{-2.5}, T^{-2}, t, D^{-3}, d, d^4)$ | 25 |
| Brace crown | $f(T^{-1.91}, T^{-1.41}, t^{0.46}, \dots$ $\dots D^{-0.05}, D^{-3.05}, D^{-1.05}, D^{-4.05}, D^{-7.05}, d, d^2, d^4, d^5, d^8)$ | 26 |

4.2.2 Interpretation of SCF plots

The SCFs significantly influence the HSS calculation, and hence, are plotted in relation to the cross-sectional properties which are interesting in the sensitivity analysis. This provides valuable insight into which parameters are primary in optimizing the structure. The specific ranges of brace and chord thickness and radius that are analyzed, are presented in Table 4.6.

Table 4.6: Ranges of cross-section properties used in SCF plots

| Parameter | Symbol | Range minimum | Range maximum | original value |
|-----------------|--------|---------------|---------------|----------------|
| Chord thickness | T | 0.08 m | 0.17 m | 0.11 m |
| Brace thickness | t | 0.03 m | 0.06 m | 0.08 m |
| Chord diameter | D | 1.61 m | 1.90 m | 1.83 m |
| Brace diameter | d | 0.88 m | 1.10 m | 1.00 m |

The SCFs are plotted in relation to these variables to ascertain their influence and direction of impact on the SCFs. Comprehensive plots can be found in Appendix A. Figure 4.3 shows the SCFs for a K-joint with balanced axial loading as a function of brace thickness and diameter.

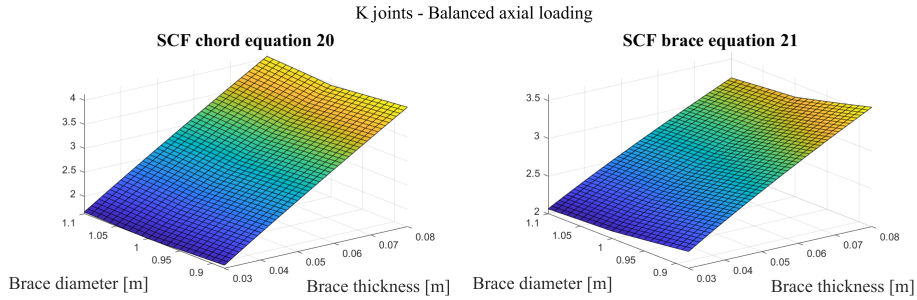


Figure 4.3: K-joint for balanced axial loading as a function of brace thickness and diameter

Each of these plots helps to understand how the functions change when the respective variables increase in value. The details of these changes are shown in Tables 4.7, 4.8, and 4.9.

Table 4.7: SCF slope for Y-joints

| SCF number | D | T | d | t |
|---|------------|------------|------------|------------|
| Axial load - chord ends fixed | | | | |
| 1 | increasing | decreasing | decreasing | increasing |
| 2 | decreasing | decreasing | decreasing | increasing |
| 3 | increasing | decreasing | decreasing | increasing |
| 4 | decreasing | decreasing | decreasing | increasing |
| Axial loading - general fixity conditions | | | | |
| 5 | increasing | decreasing | increasing | increasing |
| 6 | decreasing | decreasing | decreasing | increasing |
| 3 | increasing | decreasing | decreasing | increasing |
| 7 | decreasing | increasing | decreasing | increasing |
| In-plane bending | | | | |
| 8 | increasing | decreasing | increasing | increasing |
| 9 | increasing | decreasing | increasing | increasing |
| Out-of-plane bending | | | | |
| 10 | increasing | decreasing | increasing | increasing |
| 11 | increasing | decreasing | increasing | increasing |

Table 4.8: SCF slope for X-joints

| SCF number | D | T | d | t |
|--|------------|------------|------------|------------|
| Axial load (balanced) | | | | |
| 12 | increasing | decreasing | increasing | increasing |
| 13 | increasing | decreasing | decreasing | increasing |
| 14 | increasing | decreasing | increasing | increasing |
| 15 | decreasing | increasing | decreasing | increasing |
| In-plane bending | | | | |
| 8 | increasing | decreasing | increasing | increasing |
| 9 | increasing | decreasing | increasing | increasing |
| Out-of-plane bending (balanced) | | | | |
| 16 | increasing | decreasing | increasing | increasing |
| 17 | increasing | decreasing | increasing | increasing |
| Axial load in one brace only | | | | |
| 18 | increasing | decreasing | decreasing | increasing |
| 6 | decreasing | decreasing | decreasing | increasing |
| 19 | increasing | decreasing | decreasing | increasing |
| 7 | decreasing | increasing | decreasing | increasing |
| Out-of-plane bending on one brace only | | | | |
| 10 | increasing | decreasing | increasing | increasing |
| 11 | increasing | decreasing | increasing | increasing |

Table 4.9: SCF slope for K-joints

| SCF number | D | T | d | t |
|--|------------|------------|------------|------------|
| Balanced axial loading | | | | |
| 20 | increasing | decreasing | decreasing | increasing |
| 21 | increasing | decreasing | decreasing | increasing |
| Unbalanced in-plane bending | | | | |
| 8 | increasing | decreasing | increasing | increasing |
| 9 | increasing | decreasing | increasing | increasing |
| Unbalanced out-of-plane bending | | | | |
| 23 | increasing | decreasing | increasing | increasing |
| 24 | increasing | decreasing | increasing | increasing |
| Axial load in one brace only | | | | |
| 5 | increasing | decreasing | increasing | increasing |
| 6 | decreasing | decreasing | decreasing | increasing |
| 3 | increasing | decreasing | decreasing | increasing |
| 7 | decreasing | decreasing | decreasing | increasing |
| In-plane bending on one brace only | | | | |
| 8 | increasing | decreasing | increasing | increasing |
| 9 | increasing | decreasing | increasing | increasing |
| Out-of-plane bending on one brace only | | | | |
| 25 | increasing | decreasing | increasing | increasing |
| 26 | increasing | decreasing | increasing | increasing |

To better highlight which variables have the most impact on the functions and compare the variations, the SCF ranges for all variables are plotted in Appendix A. Two of these plots are included here, showing how the K-joint SCFs are affected by the brace thickness and radius, respectively in Figure 4.4 and 4.5.

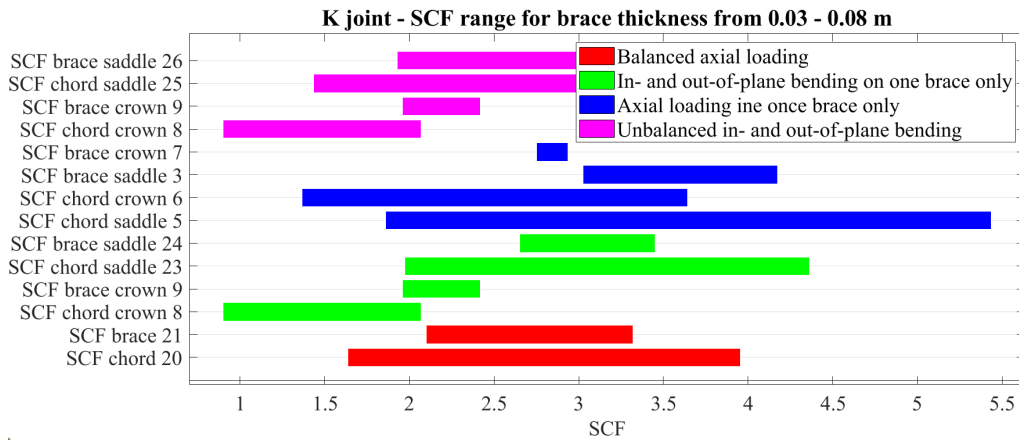


Figure 4.4: K-joint SCF range for brace thickness

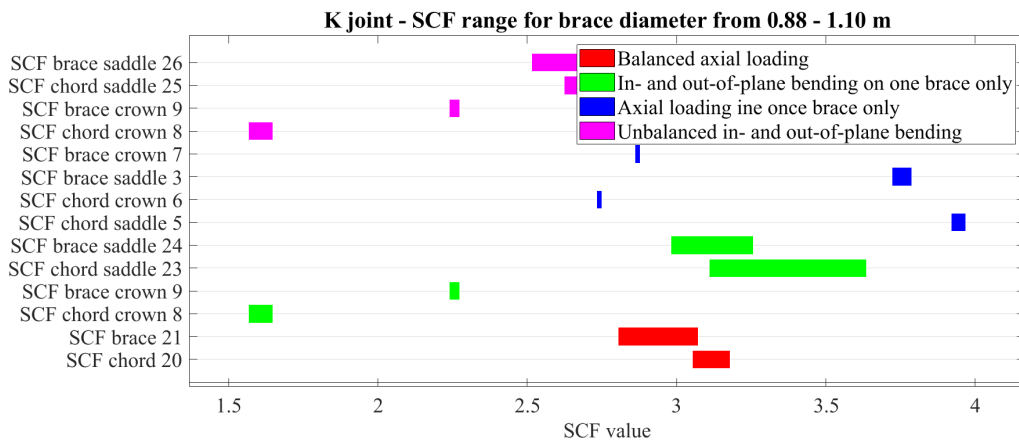


Figure 4.5: K-joint SCF range for brace diameter

Upon plotting all the SCFs, a trend becomes evident: changes in thickness influence the SCFs more significantly than changes in diameter, for both the brace and the chord. This can be attributed to the relatively smaller magnitude of thickness compared to diameter. While an increment of 0.01 m in thickness or diameter alters the mass equally, this increment constitutes a larger fraction of the initial thickness value, hence providing a greater influence to the SCFs.

Furthermore, as indicated in Tables 4.3, 4.4, and 4.5, the chord diameter and thickness usually appear with negative exponents. For instance, Figure 4.6 demonstrates how the function $x^{-1.2}$ varies, with the ranges of diameter and thickness included. This demonstrates that the gradients within the thickness range are noticeably larger than those within the diameter range, which supports the observation that the SCFs exhibit a steeper gradient with respect to thickness than diameter. However, there are some exceptions to this trend.

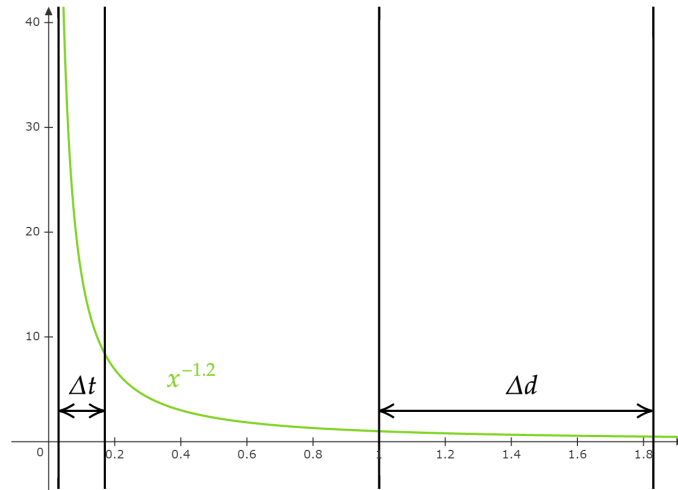


Figure 4.6: Function $x^{-1.2}$ and ranges of thickness and diameter for the X-rotor.

As indicated in Tables 4.7, 4.8, and 4.9, the general trend for SCFs is to increase with the brace thickness and decrease with the chord thickness. Therefore, in order to minimize the SCFs as much as possible, it would be optimal to reduce the thickness ratio, $\tau = \frac{t}{T}$.

5 Design Sensitivity analysis

Changes in the thickness and radius of the tubular beams in the X-rotor jacket will affect the structure's vulnerability to damage. As Figure 5.1 illustrates, these parameters naturally impact the overall mass of the structure. The objective is to establish how these properties indirectly influence the damage through the welded joints. In an optimal design scenario, the structure's mass would be minimized while maintaining low damage probability.

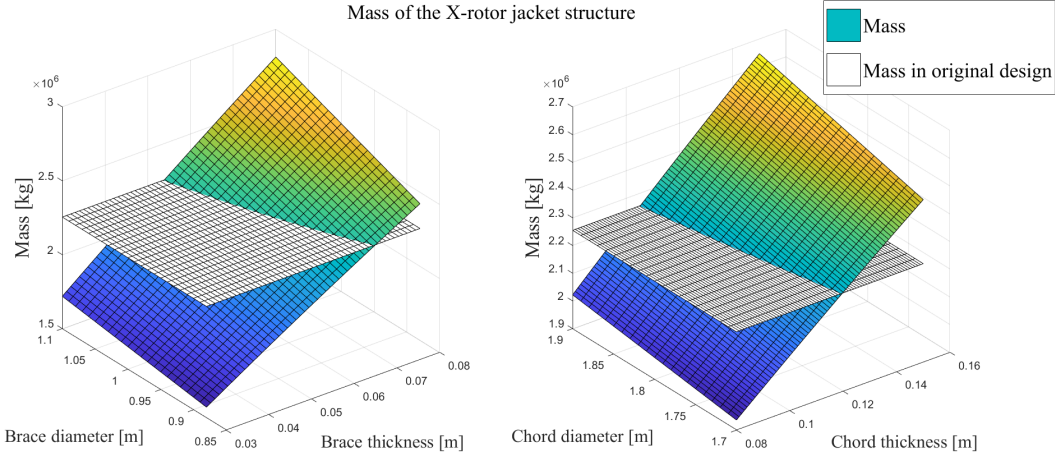


Figure 5.1: Mass of jacket structure varying with chord and brace thickness and diameter

However, damage quantification is complex due to its dependence on a structural analysis of the entire structure. Furthermore, unlike mass, damage cannot be directly correlated with the thickness and diameter of the beams through a straightforward equation. Hence, a design sensitivity analysis employing the direct differentiation method is conducted for the jacket to establish these relations. The assumptions established in Section 2.3 result in a quasi-static pseudo problem which simplifies the computational process, however, these assumptions can introduce certain deviations in the analysis, which are discovered in the following sections. In addition, it is expected that the non-linear effect discovered in Section 3.2 will affect the results.

5.1 Sensitivity of cross-section properties and step length

The damage sensitivity, evaluated across a range of cross-section property values, does not linearly depend on these properties. This requires an examination of the sensitivity of the cross-sectional properties and the level of precision obtained using these sensitivities. To find a predicted suitable step length for the design sensitivity analysis.

5.1.1 Method

Cross-section of a tubular beam

The X-rotor jacket consists of tubular beams with various thicknesses and radii. The cross-section of a tubular beam is shown in Figure 5.2 with an outer radius r and thickness t .

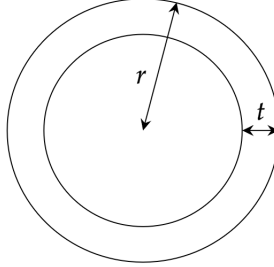


Figure 5.2: Cross-section of a tubular joint with radius r and thickness t .

Equations 5.1 and 5.2 express the area and inertia of a tubular beam in terms of r and t . Notably, due to its double-symmetric cross-section, the beam's inertia is identical about both axis $I = I_z = I_y$, and the St. Venant torsional constant equals the polar moment $I_p = 2I$.

$$A = \pi(r^2 - (r - t)^2) = 2\pi rt - \pi t^2 \quad (5.1)$$

$$I = \frac{\pi}{4}(r^4 - (r - t)^4) \quad (5.2)$$

Differentiating area and inertia

Equations 5.3 to 5.6 provides the differentiation of area and inertia with respect to cross-section properties r and t .

$$\frac{dA}{dt} = 2\pi(r - t) \quad (5.3)$$

$$\frac{dA}{dr} = 2\pi t \quad (5.4)$$

$$\frac{dI}{dt} = \pi(r - t)^3 \quad (5.5)$$

$$\frac{dI}{dr} = \pi(r^3 - (r - t)^3) \quad (5.6)$$

Step length of differentiation variables

Identifying the range over which sensitivity accurately approximates the area and inertia is essential. Considering that the sensitivity of displacements is calculated from the stiffness matrix of the original system and its sensitivity, which are functions as the cross-sectional properties. Therefore the sufficient interval of these parameters will give an indication for a sufficient interval of the

response function sensitivities. The pseudo displacement can be used in the first-order Taylor expansion inside this interval to obtain structural properties. This correlated to how often the pseudo problem should be evaluated for a change in thickness and radius, as the relation is non-linear.

An initial tubular cross-section with $t = 0.06$ m and $r = 1.00$ m is the reference point to indicate a sufficient interval. A linearly approximated area and inertia, A_{linear} and I_{linear} , is outlined in Equations 5.7 and 5.8. This is based on the first-order Taylor expansion.

$$\begin{aligned} A_{linear} &= A_{original} + \frac{dA}{dt} \Delta t \\ A_{linear} &= A_{original} + \frac{dA}{dr} \Delta r \end{aligned} \quad (5.7)$$

$$\begin{aligned} I_{linear} &= I_{original} + \frac{dI}{dt} \Delta t \\ I_{linear} &= I_{original} + \frac{dI}{dr} \Delta r \end{aligned} \quad (5.8)$$

To compare the results, the relative errors for area and inertia, e_A and e_I , are calculated according to Equation 5.9.

$$e_A = \frac{A_{analytical} - A_{linear}}{A_{analytical}} \quad e_I = \frac{I_{analytical} - I_{linear}}{I_{analytical}} \quad (5.9)$$

5.1.2 Result

Comparisons between the linear and analytical area and inertia are performed to establish an appropriate interval where the sensitivity can be used to determine the response functions due to a change in thickness or radius. Figures 5.3 and 5.4 illustrate the degree of precision achievable in calculating the area and inertia using differentiation of the original properties concerning r and t within a Δt -range and Δr -range of $[-0.01, 0.01]$.

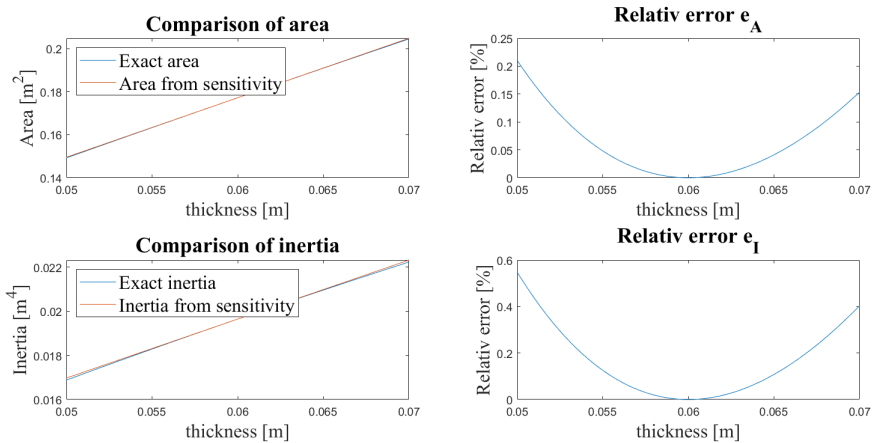


Figure 5.3: To the left: Area and inertia compared analytically and from sensitivity concerning a change in the thickness. To the right: Relative error of the linear area and inertia.

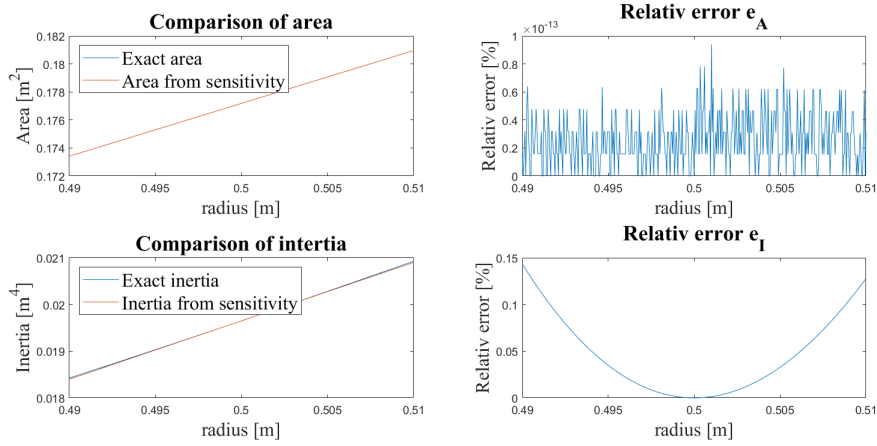


Figure 5.4: To the left: Area and inertia compared analytically and from sensitivity concerning a change in the radius. To the right: Relative error of the linear area and inertia.

5.1.3 Discussion

From Figure 5.3 and 5.4 follows these observation: Since the area is a linear function of the radius, the sensitivity will always give the exact area. The area is a quadratic function of the thickness, so the error amplifies as Δt increases. An interval of ± 0.01 m results in the linear area having a maximum relative error of 0.21 %. With the inertia being a forth-degree polynomial function of the radius and thickness an interval of ± 0.01 m results in the linear inertia having a maximum relative error of 0.55 % and 0.14 % with respect to thickness and radius.

As the relative error of the inertia and area shows the sensitivity, concerning both thickness and radius, can be used inside a range of ± 0.01 m from the original value to find an accurate approximation of the sensitivity. Importantly, this relative error will change as the cross-section dimensions vary, yet the results will remain satisfactory, provided the increment is sufficiently small compared to the original properties.

Further, for response sensitivities derived from these primary ones, such as displacement sensitivity, the impact of the difference between the properties used to derive the sensitivities and the point of interest will be greater. Nevertheless, by examining the linear area and inertia, a reliable interval provides a degree of assurance for the sensitivity calculation of the response functions.

It should be stated that the sufficient interval for the response sensitivities are also affected by the assumptions made in the direct differentiation method, such that this ± 0.01 m is only a prediction and must be validated when the damage sensitivity is found. Only solving the pseudo problem once would be computationally cheap, however, it may not provide the correct slope for large changes in radius and thickness.

5.2 Sensitivity of stresses in the X-rotor

The sensitivities of the response functions are obtained using the direct differentiation method by solving the pseudo problem described in Section 2.3.

5.2.1 Method

Load simulation

The objective is to determine the sensitivity of the structure's stresses to variations in its dimensions by examining a specific load case. The second load case in Table 4.1 with a wind speed of 19.5 m/s and a probability of occurrence at 0.006. Gravity is also considered. The marine growth has a density of 1325 kg/m^3 and a thickness of 0.06 m which is applied to all structural members between 2 to 40 meters below mean sea level. The aerodynamic loads transferred to the structure in the tower top are defined in Figure 5.5 consisting of loads and moments transversal to wind, in wind direction and vertical direction working simultaneously.

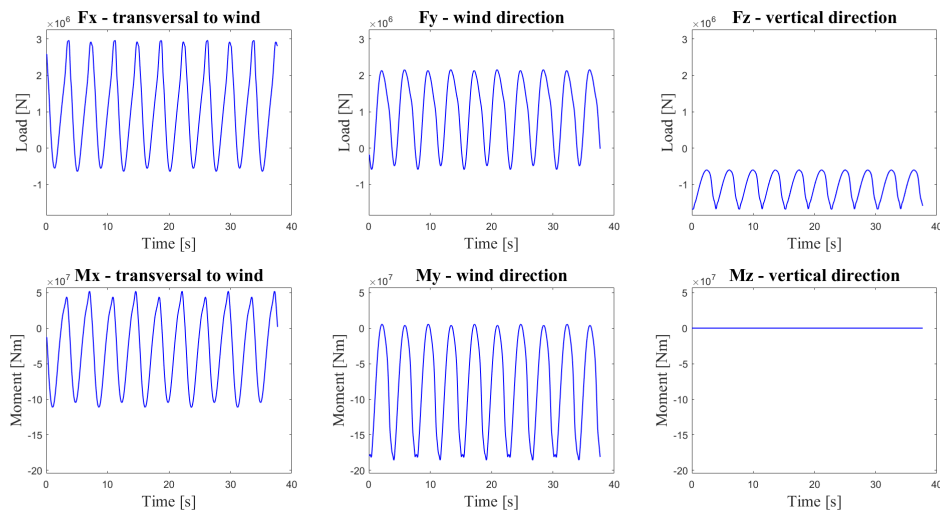


Figure 5.5: The time history of mean wind resultant loading for a windspeed of 19.5 m/s applied to the tower top for all directions.

The jacket model is established in FEDEM by another group member of the NTNU X-rotor project, while all simulation and postprocessing are performed by the author.

A dynamic analysis is performed for the 8 different structures where the brace thickness of beam 82 is 0.03 m, 0.04 m, 0.05 m, 0.06 m, 0.07 m and 0.08 m. The rest of the design variables are then kept constant to the original design defined in Table 2.1. The same procedure is followed for 12 different structures where the brace radius of beam 82 is found for all values inside [0.44 m, 0.55 m] with a change of 0.01 m. The geometrical stiffness is considered in these analyses.

This analysis provides the global coordinates of the nodes. These coordinates are subsequently transformed into the local coordinate system of the adjusted beam using the transformation matrix with the rotation matrix of beam 82 $\mathbf{R}_{beam\ 82}$ established in Equation 3.10.

Differentiated stiffness matrix

The jacket is modelled with FEDEM Windpower using the Euler-Bernoulli beam theory. As the

numerical stiffness matrix of the X-rotor includes non-linear effects and is dependent on the load situation, the analytical stiffness matrix of an Euler-Bernoulli beam element is used as discussed in Section 3.3.3. Differentiation of the stiffness matrix for a tubular beam is provided in Equation 5.11 expressed in terms of the stiffness property sensitivities presented in Equation 5.10 where b is a cross-section property.

$$dA^* = \frac{E \frac{dA}{db}}{L} \quad , \quad dI^* = \frac{E \frac{dI}{db}}{L^3} \quad , \quad dT^* = \frac{2G \frac{dT}{db}}{L} \quad (5.10)$$

$$\frac{d\mathbf{K}}{db} = \begin{bmatrix} dA^* & 0 & 0 & 0 & 0 & 0 & -dA^* & 0 & 0 & 0 & 0 & 0 \\ 0 & 12dI^* & 0 & 0 & 0 & 6LdI^* & 0 & -12dI^* & 0 & 0 & 0 & 6LdI^* \\ 0 & 0 & 12dI^* & 0 & -6LdI^* & 0 & 0 & 0 & -12dI^* & 0 & -6LdI^* & 0 \\ 0 & 0 & 0 & dT^* & 0 & 0 & 0 & 0 & 0 & -dT^* & 0 & 0 \\ 0 & 0 & -6LdI^* & 0 & 4L^2dI^* & 0 & 0 & 0 & 6LdI^* & 0 & 2L^2dI^* & 0 \\ 0 & 6LdI^* & 0 & 0 & 0 & 4L^2dI^* & 0 & -6LdI^* & 0 & 0 & 0 & 2L^2dI^* \\ -dA^* & 0 & 0 & 0 & 0 & 0 & dA^* & 0 & 0 & 0 & 0 & 0 \\ 0 & -12dI^* & 0 & 0 & 0 & -6LdI^* & 0 & 12dI^* & 0 & 0 & 0 & -6LdI^* \\ 0 & 0 & -12dI^* & 0 & 6LdI^* & 0 & 0 & 0 & 12dI^* & 0 & 6LdI^* & 0 \\ 0 & 0 & 0 & -dT^* & 0 & 0 & 0 & 0 & 0 & dT^* & 0 & 0 \\ 0 & 0 & -6LdI^* & 0 & 2L^2dI^* & 0 & 0 & 0 & 6LdI^* & 0 & 4L^2dI^* & 0 \\ 0 & 6LdI^* & 0 & 0 & 0 & 2L^2dI^* & 0 & -6LdI^* & 0 & 0 & 0 & 4L^2dI^* \end{bmatrix} \quad (5.11)$$

The entire global stiffness matrix must be differentiated when looking at a structure consisting of several beams. However, the stiffness matrix of all other beams does not depend on the cross-section properties of the one beam that is changed, and their sensitivity is zero as they are not affected.

Pseudo-problem

The sensitivity of the response is assessed by solving the pseudo-problem in Equation 2.6 using FEDEM Windpower. Where the loads $-\frac{d\mathbf{K}}{db_i} \mathbf{u}$ are implemented in the local system of the examined beam.

To isolate the impact of this load, all other loads are set to zero such that there are no gravity, marine growth, water or wind acting. A quasi-static analysis is performed such that the system behaves as a static load case in each time step, and no dynamic effects occur. The geometrical stiffness effect is not considered for the pseudo-problem.

This is performed for all 8+12 structure configurations where the outcome of this static analysis represents the sensitivity of the initial response, expressed in global coordinates. This result is then converted back into local coordinates using the transformation matrix.

Stress sensitivities

The stresses can be expressed in matrix form in terms of the displacements shown in equation 5.12, which is found by combining the stiffness matrix in Equation 2.10 and the stress formulas in Equation 2.12 in a stress calculation matrix of beam i , \mathbf{S}_i given in Equation 5.13.

$$\begin{bmatrix} \sigma_{N,i}^1 \\ \sigma_{My,i}^1 \\ \sigma_{Mz,i}^1 \\ \sigma_{N,i}^2 \\ \sigma_{My,i}^2 \\ \sigma_{Mz,i}^2 \end{bmatrix} = \boldsymbol{\sigma}_i = \mathbf{S}_i \mathbf{u}_i \quad (5.12)$$

$$\mathbf{S}_i = \begin{bmatrix} \frac{E}{L} & 0 & 0 & 0 & 0 & 0 & -\frac{E}{L} & 0 & 0 & 0 & 0 & 0 \\ 0 & 0 & -\frac{6Er_i}{L^2} & 0 & \frac{4Er_i}{L} & 0 & 0 & 0 & \frac{6Er_i}{L^2} & 0 & \frac{2Er_i}{L} & 0 \\ 0 & \frac{6Er_i}{L^2} & 0 & 0 & 0 & \frac{4Er_i}{L} & 0 & -\frac{6Er_i}{L^2} & 0 & 0 & 0 & \frac{2Er_i}{L} \\ -\frac{E}{L} & 0 & 0 & 0 & 0 & 0 & \frac{E}{L} & 0 & 0 & 0 & 0 & 0 \\ 0 & 0 & -\frac{6Er_i}{L^2} & 0 & \frac{2Er_i}{L} & 0 & 0 & 0 & \frac{6Er_i}{L^2} & 0 & \frac{4Er_i}{L} & 0 \\ 0 & \frac{6Er_i}{L^2} & 0 & 0 & 0 & \frac{2Er_i}{L} & 0 & -\frac{6Er_i}{L^2} & 0 & 0 & 0 & \frac{4Er_i}{L} \end{bmatrix} \quad (5.13)$$

The differentiation of the stresses concerning a cross-section property b_i is found using the chain rule as shown in Equation 5.14.

$$\frac{d\boldsymbol{\sigma}}{db_i} = \frac{\partial \boldsymbol{\sigma}}{\partial b_i} + \frac{\partial \boldsymbol{\sigma}}{\partial \mathbf{u}} \frac{d\mathbf{u}}{db_i} \quad (5.14)$$

Sensitivity concerning the thickness of beam i

When differentiating the stresses in beam i with respect to the thickness of beam i , the first term in equation 5.14 will be zero, $\frac{d\mathbf{S}_i}{dt_i} = \mathbf{0}$, as the stress calculation matrix does not depend on the thickness. Equation 5.15 gives the resultant expression for the stress sensitivity of beam i .

$$\frac{d\boldsymbol{\sigma}_i}{dt_i} = \mathbf{S}_i \frac{d\mathbf{u}_i}{dt_i} \quad (5.15)$$

The sensitivity of all other beams denoted as j is presented in Equation 5.16, due to a change in b_i the other beams will have a change in the displacements due to redistribution of loads throughout the structure.

$$\frac{d\boldsymbol{\sigma}_j}{dt_i} = \mathbf{S}_j \frac{d\mathbf{u}_j}{dt_i} \quad (5.16)$$

Sensitivity with respect to the radius of beam i

Equation 5.17 and 5.18 provides the differentiation of stresses in beam i and all other beams j with respect to r_i , as the stress calculation matrix is dependent on the radius of beam i .

$$\frac{d\boldsymbol{\sigma}_i}{dr_i} = \frac{d\mathbf{S}_i}{dr_i} \mathbf{u}_i + \mathbf{S}_i \frac{d\mathbf{u}_i}{dr_i} \quad (5.17)$$

$$\frac{d\boldsymbol{\sigma}_j}{dr_i} = \mathbf{S}_j \frac{d\mathbf{u}_j}{dr_i} \quad (5.18)$$

Comparison of results

To identify the accuracy the nominal stresses are also determined from the simulation using Equation 2.12. To evaluate the accuracy of the direct differentiation method the first-order Taylor expansion of the stresses using the sensitivities is determined for an interval of $[-0.005, 0.004]$ around the simulation values.

5.2.2 Results

Thickness sensitivity

The stresses from the simulation for a thickness of 0.05 m and 0.06 m of beam 82 are plotted and compared to the stresses obtained through the pseudo problem for a thickness of 0.05 m using the sensitivities at 0.06 m. This indicates how accurately the slope of the stresses is calculated. The validity of employing the direct differentiation method to compute stresses is being assessed within a specific time interval from 31.73 to 35.73 s. This interval falls within the steady-state region of the response. The relative error is for the stresses found for the sensitivities compared to the simulation results for a thickness of 0.05 m.

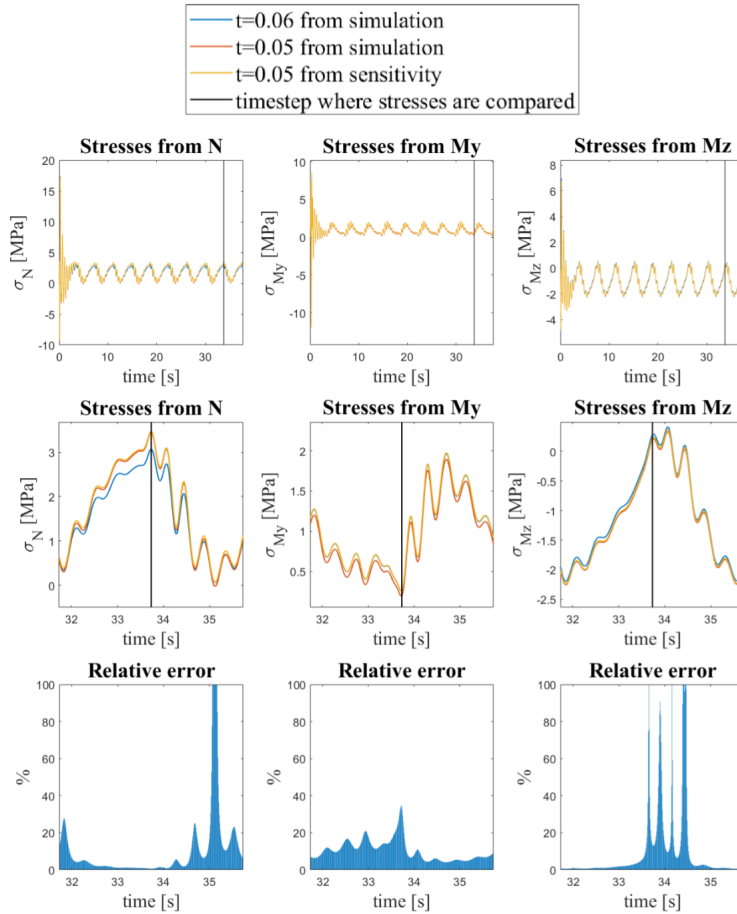


Figure 5.6: Stresses in beam 82 node 1 for a thickness of 0.06 m and 0.05 m from simulation compare to the stress for a thickness of 0.05 m found from the pseudo problem with 0.06 m thickness. The relative error for the stresses from the sensitivity is found for a time interval from 31.73 to 35.73 seconds.

The sensitivities are further investigated at the time step 33.73 s for a brace thickness of 0.03 m to 0.08 m.

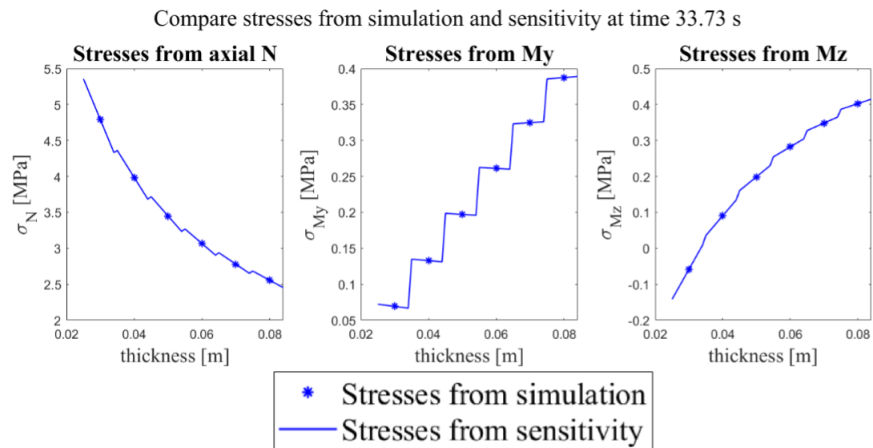


Figure 5.7: Stresses in beam 82 node 1 for different brace thicknesses found from simulation and using the first-order Taylor expansion to determine the stresses a thickness range $[-0.005, 0.004]$ around the simulation values.

Radius sensitivity

The same procedure as the sensitivity with respect to the thickness is followed for a brace radius of 0.5 m and 0.49 m.

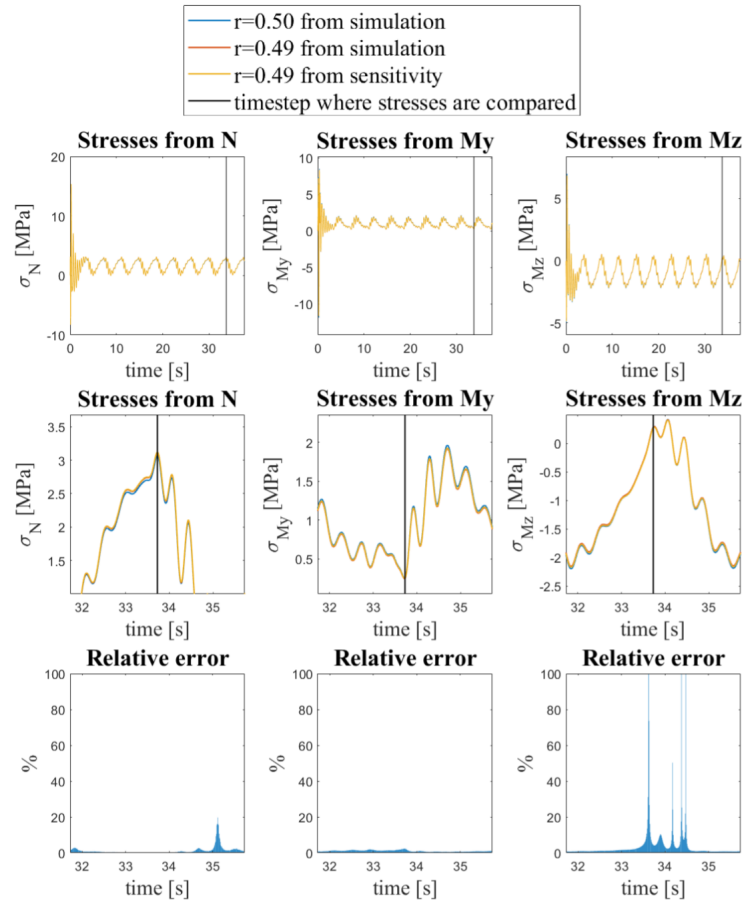


Figure 5.8: Stresses in beam 82 node 1 for a brace radius of 0.50 m and 0.49 m from simulation compare to the stress for a radius of 0.49 m found from the pseudo problem with 0.50 m radius. The relative error for the stresses from the sensitivity is found for a time interval from 31.73 to 35.73 seconds.

The sensitivities are further investigated at the time step 33.73 s for a brace radius of 0.47 m to 0.52 m.

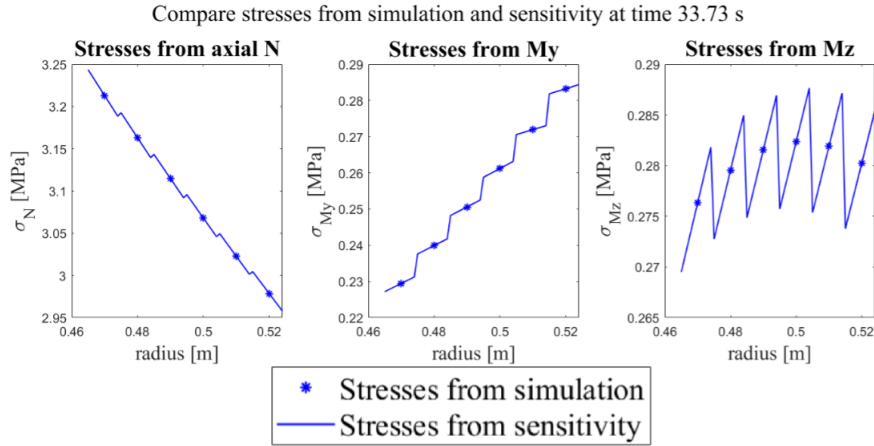


Figure 5.9: Stresses in beam 82 node 1 for different brace radii found from simulation and using the first-order Taylor expansion to determine the stresses a radius range $[-0.005, 0.004]$ around the values from the simulations.

5.2.3 Discussion

Our initial observation in Figures 5.6 and 5.8 highlights that stresses resulting from axial loads exceed those resulting from bending moments. As anticipated, the highest relative error occurs for stresses near zero, as this involves the division of a small number. For the thickness sensitivity, the relative error is the largest for the moments in the y-direction shown in the lower middle plot in Figure 5.6. This can also be observed in Figure 5.7 where the stress from My, $\frac{dM_y}{dt_{82}}$, has a very imprecise slope derived from the sensitivity, even with the wrong gradient sign.

A more significant relative error is observed for thickness changes compared to the radius when assessing stresses using the first-order Taylor expansion. This is likely attributed to the proportion of thickness increment relative to the thickness magnitude exceeding the equivalent ratio for the radius.

The slope of the axial stresses concerning both thickness and radius is quite accurately determined with the direct differentiation method.

For the radius sensitivity, the slope of the stresses from Mz , $\frac{dM_z}{dr_{82}}$, shown in the right plot in Figure 5.8, exhibits the same behaviour as for $\frac{dM_y}{dt_{82}}$. This inaccuracy can be traced back to four potential sources:

- The employment of the Euler-Bernoulli beam element's analytical stiffness matrix instead of the precise numerical stiffness matrix.
- Assumptions incorporated in the pseudo-problem definition include a presumed quasi-static load case and unchanging external loads.
- Not including the change of internal axial loading, which will affect the geometrical stiffness matrix.
- The non-linear effect identified in Section 3 revealing that the load are increasing quadratically with the displacements.

A comparable pattern is observed in flexibility load cases in Chapter 3, where the columns linked to bending flexibility exhibit a non-linear effect. As we conduct a similar simulation with static

analysis for the pseudo-problem, using identical beam elements and joints, it's quite likely that this non-linear effect will occur. This has an impact on pseudo displacements because the correlation between pseudo load and displacements follows the generalized Hooke's law. This law, however, doesn't account for the relationship between these squared loads and displacement. Consequently, the pseudo load creates displacements that don't accurately represent the sensitivity of the response to changes in thickness or radius. Figures 5.7 and 5.9, which display imprecise slopes for the bending moment stresses and accurate stresses from the axial load, advocate the existence of a non-linear effect when performing quasi-static load analysis in FEDEM. This means that even if the flexibility method did not provide an exact stiffness matrix, it provided valuable insight into an important source of error that most likely would not have been discovered otherwise.

The second and third potential source of imprecision in the list above will arise as marine growth, gravity, damping and geometrical stiffness are included in our load cases. Marine growth is a function of the outer diameter, and geometrical stiffness relates to the internal axial load of the beam element. In addition, the mass and dynamical properties are not considered as a quasi-static analysis is assumed. The sensitivity of these relations is neglected in the direct differentiation method and given that the axial stress sensitivity is determined with good accuracy, this assumption appears to be justifiable.

5.3 Sensitivity of damage in the X-rotor

The hypothesis outlines that in offshore jacket structures, the critical design factor is the damage to the welded joints. Accordingly, this chapter aims to delve into the impact of variations in structural properties, notably the cross-section, on the damage using the direct differentiation method. Such an understanding has implications for future structural optimisation, where the objective is to find the perfect equilibrium between minimising damage and maintaining a low mass. The MATLAB scripts to calculate the damage and its sensitivity of the welded joints at the X-rotor legs are provided in Appendix C.

5.3.1 Method

Load case

The damage and its sensitivity are found for the load case considered to determine the stress sensitivities in Section 5.2 with a wind speed of 19.5 m/s and for all 8+12 structure configurations concerning the changes of brace thickness and radius of beam 82. The stress sensitivities obtained in the previous section are used to determine the damage sensitivity.

In addition as stated in Section 4.2 the chord thickness will affect the SCFs significantly, the trend is that increasing the chord thickness will decrease the SCFs. It is expected that with a larger chord cross-section, the legs stiffness will increase and lead to decreasing loads in the braces. To analyse this the brace thickness sensitivity is found for a chord thickness of 0.10 m, 0.11 m and 0.12 m, where all chords are changed.

HSS for damage calculation

As section 2.8 states, the stresses should be evaluated at eight hot spots. Differentiating these is done as stated in Equation 5.19 for all the stress terms superpositioned together.

$$\frac{d\sigma_{hotspot}}{db_i} = \frac{dSCF}{db_i}\sigma + SCF\frac{d\sigma}{db_i} \quad (5.19)$$

The SCFs exhibit intricate relationships with the cross-section properties. Therefore the least square method is employed to create a function of fractional and negative exponent terms of the cross-section properties. However, it's important to note that some SCF functions relate to these properties differently, for example, through a trigonometric function. These properties are then approximated with a power function to include their sensitivity. The obtained expression is then used to find the sensitivity of the SCFs by derivating them. The flow chart in Figure 5.10 shows the procedure used for all SCFs. This shortens the computational time and, by streamlining the process, reduces the potential for errors.

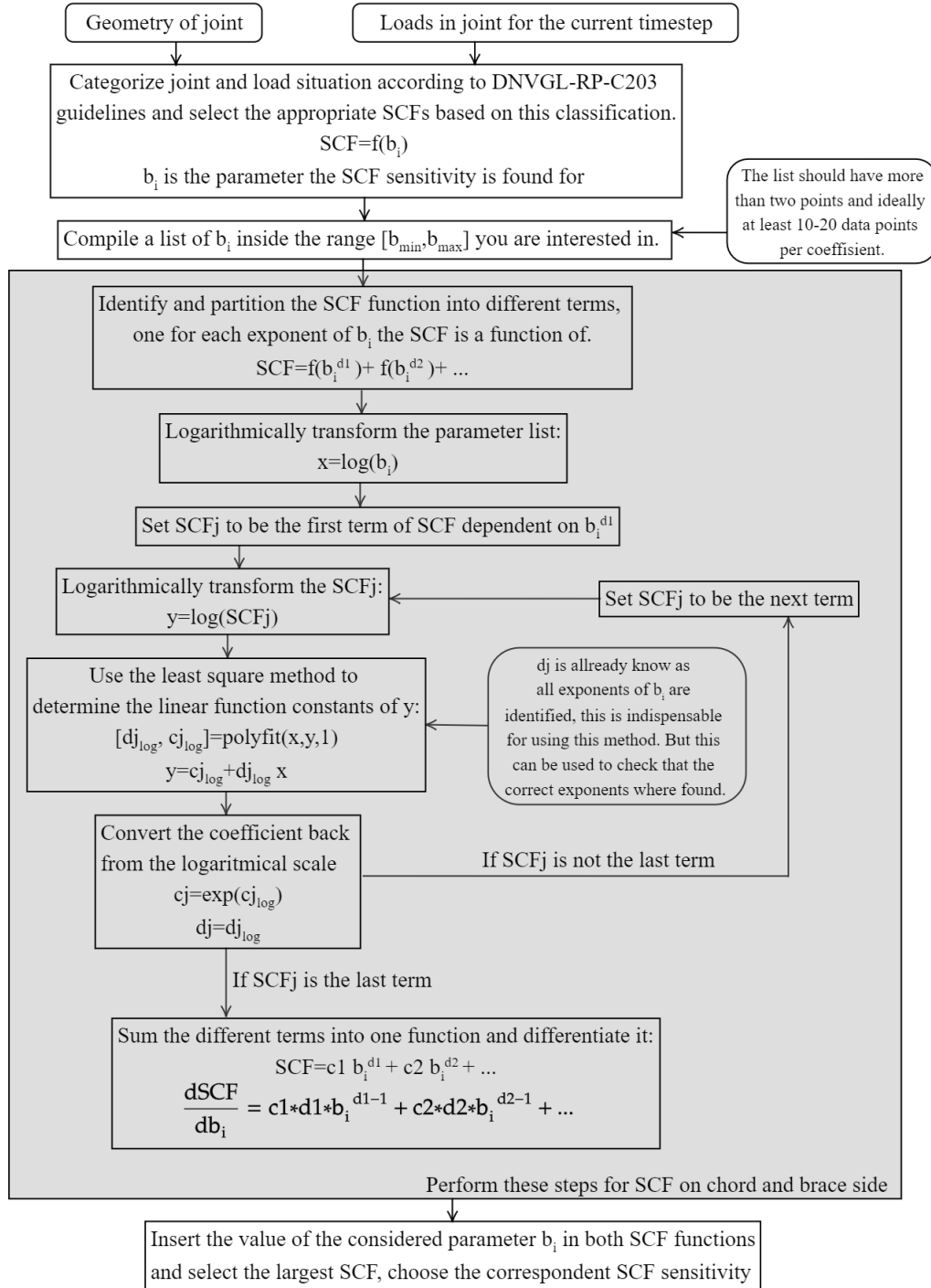


Figure 5.10: Flow chart for determining the SCF and its sensitivity of a welded joint.

An example of the steps in the flow chart in Figure 5.10 is given for SCF 5, axial load - general fixity conditions in the chord saddle, and how it depends on the brace thickness in the Appendix D.

In the evaluation of the SCFs, the following geometrical assumptions are made:

- Chord-end fixity parameter for Y-joints is defined as $C = 0.7$.
- No short chords in the jacket geometry.
- The parameter L is defined as half of the chord length above and half of the chord length below, hence $L=12.7$ m for all K-joints at the legs. The reason for this is that no joint caps are considered in the model.

To establish the HSS in beam 82, the pink beam in Figure 4.1, node 1 connected to the X-rotor leg, the joint classification and corresponding SCFs found in Section 4.1 are used.

Sensitivity of stress ranges

As the pseudo problem is assumed to be a quasi-static load case, the cyclic shape of the stress will not change as the parameter b_i changes. This means that all stress peaks and valleys does not change position. Furthermore, as the stress ranges are determined solely by the stress cycle's peak and valley values, the stress ranges' sensitivity similarly depends exclusively on these extremes.

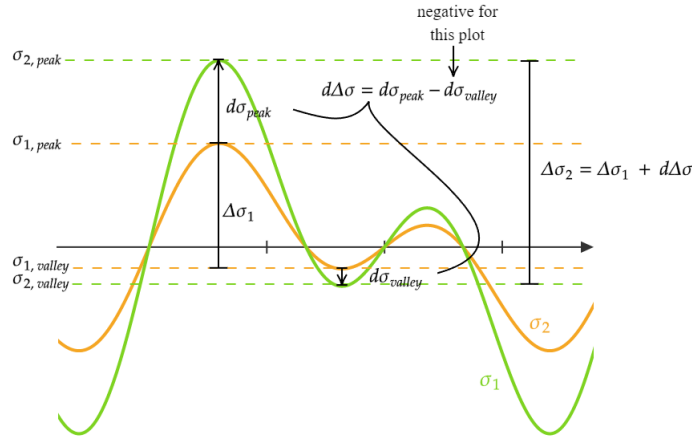


Figure 5.11: Sketch of stress ranges and the change in stress ranges for a quasi-static stress cycle.

Figure 5.11 illustrates how the sensitivity of the stress ranges is established. Where σ_1 and σ_2 is two time dependent stress series where the parameter b_i is different. The difference between the two stress ranges $\Delta\sigma_1$ and $\Delta\sigma_2$ are $d\Delta\sigma$ which are due to a change in a parameter b_i . This change is found as Equation 5.20 shows by subtracting the change of the peak stress and valley stress in the stress cycle.

$$d\Delta\sigma = d\sigma_{peak} - d\sigma_{valley} \quad (5.20)$$

As Equation 5.21 [27] states, to make this into a sensitivity, the change in the stress ranges $d\Delta\sigma$ is divided by the difference in the considered parameter db_i .

$$\frac{d\Delta\sigma}{db_i} = \frac{d\sigma_{peak}}{db_i} - \frac{d\sigma_{valley}}{db_i} \quad (5.21)$$

Damage sensitivity

In the expression of the damage given in Equation 2.27, the only term dependent on the cross-section properties is the stresses in terms of the stress ranges. This results in the sensitivity provided in Equation 5.22.

$$\frac{dD}{db_i} = \frac{DFF \cdot m}{\bar{a}} \sum_{j=1}^k d_j n_j (\Delta\sigma_j)^{m-1} \frac{d\Delta\sigma_j}{db_i} \quad (5.22)$$

Table 2-3 S-N curves for tubular joints in DNVGL-RP-C203 give the S-N curve parameters. The environment for the jacket beams is seawater with cathodic protection, and the curve for a number of cycles larger than $1.8 \cdot 10^6$ to failure is used for all stress ranges. This implies $\log \bar{a}$ of 16.13 and m of 5.0 [9]. To be conservative DFF is set to 3, which corresponds to "Non-accessible areas, areas not planned to be accessible for inspection and repair during operation" according to Table 1 Design fatigue factors in DNVGL-OS-C101 [8].

As the loads series is 37.7 s long, this must be scaled to hold for 20 years, the design lifetime. The scaling factor d_i is calculated as shown in Equation 5.23, where $d_i = d$ is the same for all cycles. This scaling parameter also considers the probability of occurrence of that load case p .

$$d = p \cdot \frac{20 \text{ years} \cdot 365 \frac{\text{days}}{\text{year}} \cdot 24 \frac{\text{hours}}{\text{day}} \cdot 60 \frac{\text{minutes}}{\text{hour}} \cdot 60 \frac{\text{seconds}}{\text{minute}}}{37.7 \text{ seconds}} \quad (5.23)$$

The stress ranges and cycle counts are calculated using rainflow counting according to the flow chart in Figure 2.12, and the corresponding sensitivity of the individual stress ranges is calculated according to Equation 5.21.

To identify the method's accuracy, the simulation damage is found from Equation 2.27. Then, the first-order Taylor expansion is used to find the damage from the sensitivities for a range of [-0.005, 0.004] around the simulation damage points.

Damage of other beams affected by a change in beam 82

A modification to beam 82 results in a redistribution of loads within the jacket structure. The beams connected to the same leg as beam 82 at the same jacket side are investigated to capture this effect. These are shown in Figure 4.1. The damage of these joints and their sensitivity are determined in the same way considering the change of stresses in these beams due to a change in the thickness of beam 82 as provided in Equation 5.16. The SCFs of these beams remain constant, and all the joints are assumed to be Y-joints to be conservative. In assessing HSS, chord stresses are not considered for hot spots 1 and 5.

This provides an indication of how accurately the pseudo problem captures the redistribution of loads and hence the damage sensitivity, due to the modification of beam 82, on the overall structure. This is also interesting from an optimizing perspective, to quantify how much other beams are affected by changing beam 82. To quantify these effects the relative damage change of beam j is found according to Equation 5.24 and the percent damage change relative to the change in beam 82 according to Equation 5.25. Both of them are comparing all changes related to the original design with a thickness of 0.06 m. These relative changes are obtained from the simulation values, not including the sensitivities.

$$\Delta D_{j,relative} = \frac{|D_{j,HSS} - D_{j,HSS,t=0.06m}|}{D_{j,HSS,t=0.06m}} \quad (5.24)$$

$$\% \Delta D_{j,relative} = \frac{|D_{j,HSS} - D_{j,HSS,t=0.06m}|}{|D_{82,HSS} - D_{82,HSS,t=0.06m}|} \quad (5.25)$$

5.3.2 Results

Thickness sensitivity

The thickness range from 0.03 m to 0.08 m, is considered. The damage and its sensitivity are found for beam 82 node 1. To compare the joint classified as a K- and Y-joint, the damage is found for both cases in Figure 5.12. However, Section 4.1 states that the joint is 40.77 % K-joint and 59.23 % Y-joint in the 37.7 s, the resultant damage is also included in Figure 5.12.

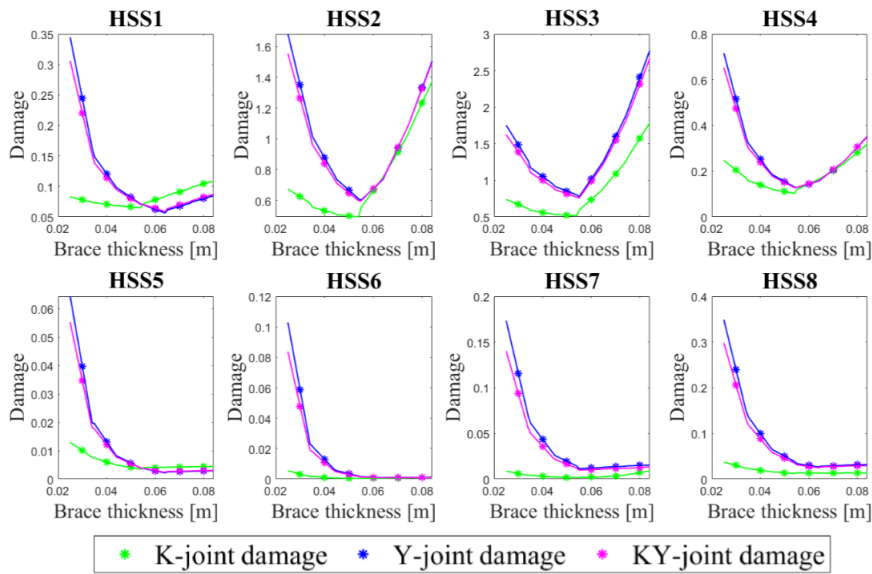


Figure 5.12: Damage in beam 82 node 1 for different brace thicknesses found from the simulation and using the first-order Taylor expansion to determine the stresses, in a thickness increment range $[-0.005, 0.004]$ around the simulation values, from the sensitivity. Joint classified as a K-joint, as a Y-joint and at each time step according to the percentage established in Section 2.1.1.

As stated in Section 4.2 the chord thickness will affect the SCFs significantly, therefore the damage sensitivity with respect to the brace thickness of beam 82 node 1 for a thickness range from 0.03 m to 0.08 m is found for a chord thickness of 0.10 m, 0.11 m and 0.12 m in Figure 5.13.

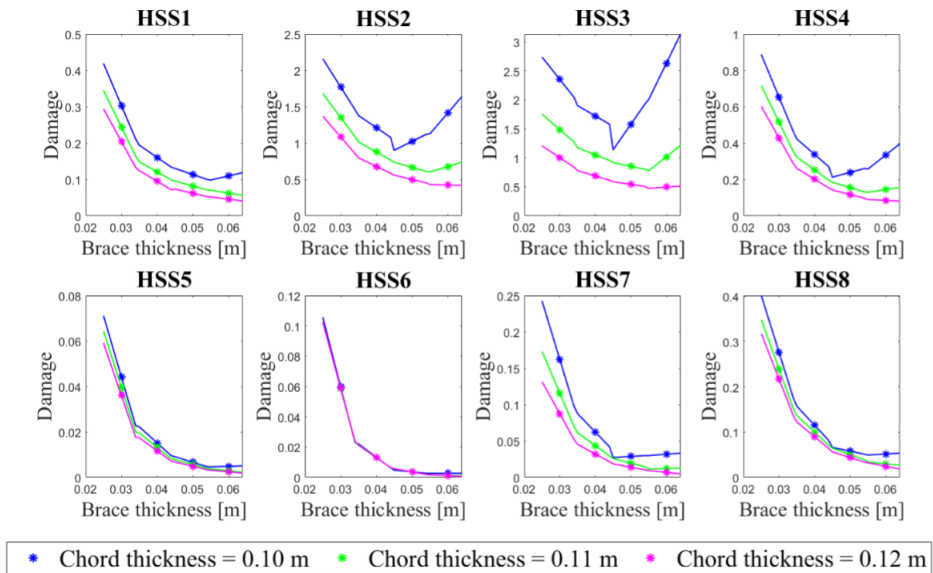


Figure 5.13: Joint classified as a Y-joint. Damage in beam 82 node 1 for different brace thicknesses found from the simulation and using the first-order Taylor expansion to determine the stresses, in a thickness increment range $[-0.005, 0.004]$ around the simulation values, from the sensitivity. Damage found for a chord thickness of 0.10 m, 0.11 m and 0.12 m.

The slope of the damage of the braces above beam 82 found from the direct differentiation method is shown for HSS1 in Figure 5.14. All HSS damages can be found in Appendix B. In addition, the relative damage change of beam j and the percent damage change relative to the change in beam 82 is shown in Figure 5.15.

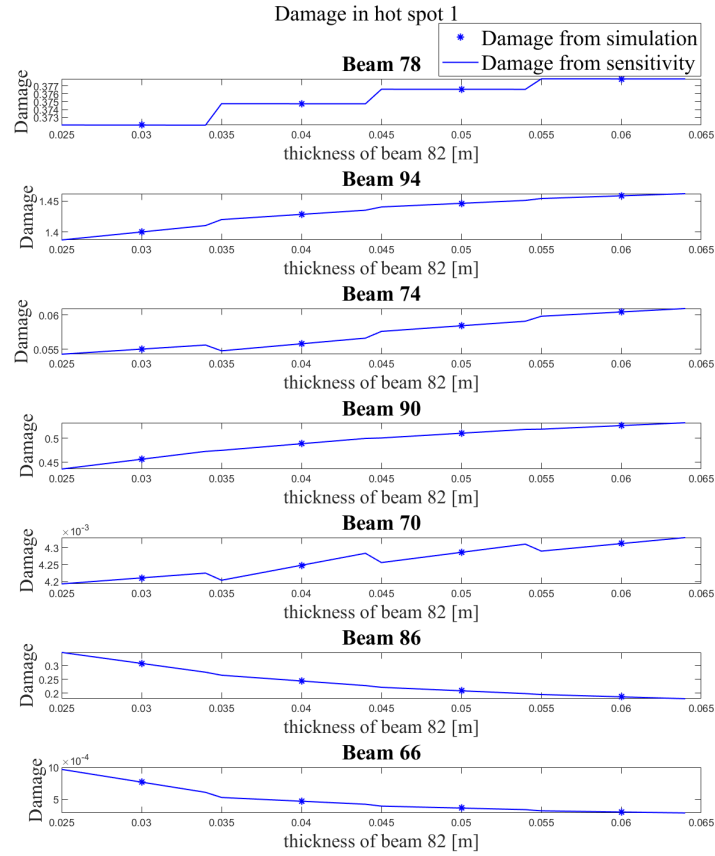


Figure 5.14: Damage in HSS1 in beams shown in Figure 4.1 for different brace thicknesses of beam 82 found from simulation and using the first-order Taylor expansion to determine the stresses in a thickness increment range $[-0.005, 0.004]$ around the values from the simulations. All joints are classified as Y-joints.

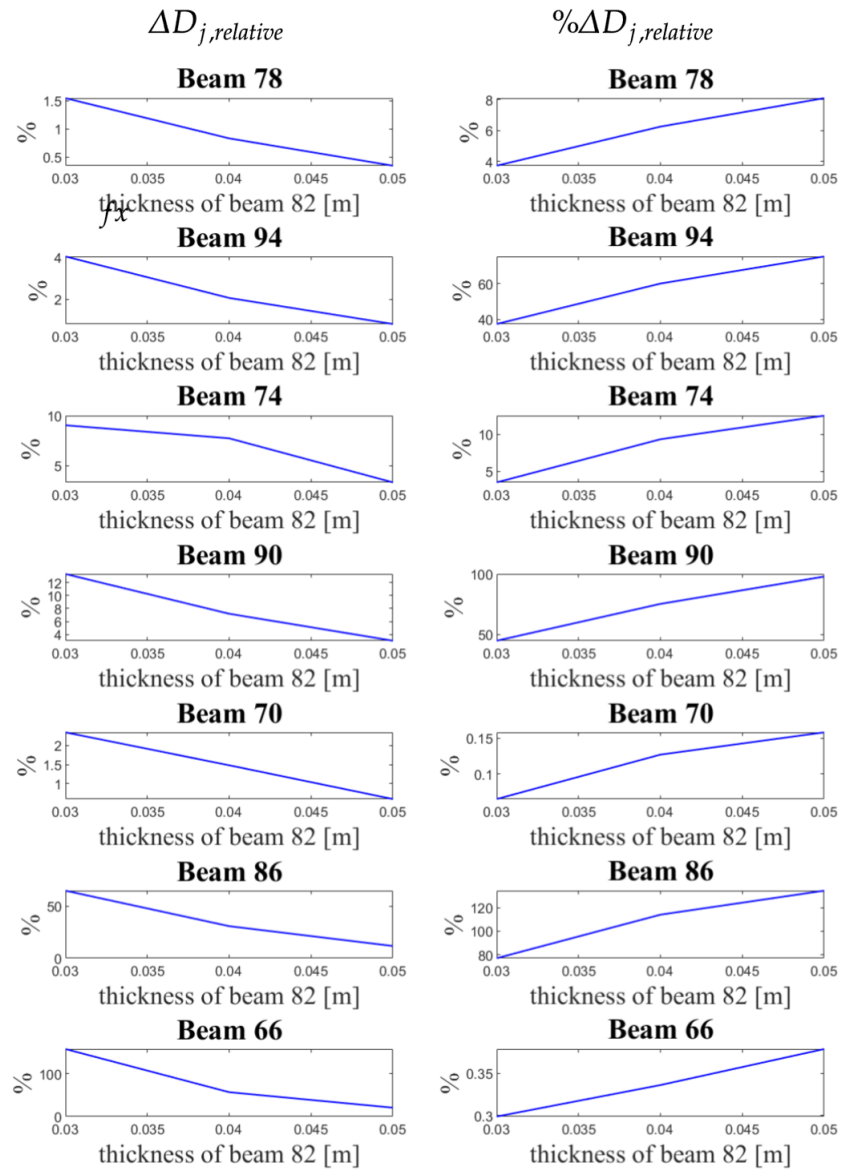


Figure 5.15: Left: Relative change in damage of HSS1 of the beams in Figure 4.1 compared to the damage of the original design with a thickness of 0.06 m. All joints are classified as Y-joints. Right: Magnitude of change in damage of HSS1 of the beams in Figure 4.1 compared to the damage change of beam 82. All joints are classified as Y-joints.

Radius sensitivity

The radii considered are from 0.44 m to 0.55 m, a range around the original radius of 0.50 m. The damage and its sensitivity are found for beam 82 node 1, classified as a K-joint, in Figure 5.16. This is not conservative but provides an insight to how accurately the direct differentiation method can be used to determine the damage sensitivity with respect to the radius.

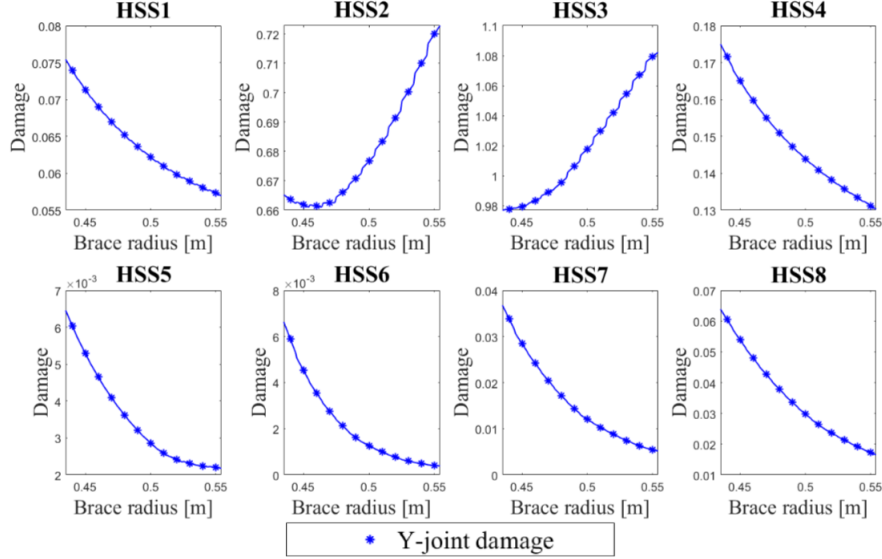


Figure 5.16: Damage in beam 82 node 1 for different brace radii found from simulation and using the first-order Taylor expansion to determine the stresses in a radius increment $[-0.005, 0.004]$ around the values from the simulations. Joint classified as a K-joint.

5.3.3 Discussion

Figures 5.12 and 5.16 show that using the direct differentiation method can accurately determine damage sensitivity with respect to the cross-section properties of the X-rotor jacket structure. A variable step of 0.01 m proves to be an appropriate interval, given that the damage is a non-linear function of both thickness and radius. For effective optimisation, it is important to ascertain whether the pseudo-problem requires evaluation at multiple points for extensive alterations in thickness and radius. For instance, for HSS2 in Figure 5.12 relying on the damage gradient at $t=0.04$ m to predict the damage at $t=0.07$ m would result in inaccurate damage estimations.

The damage appears to be more sensitive to alterations in thickness than in radius. This is reasonable as the percentage change for thickness is greater than for radius. Notably, a modification of 0.01 m in either of these cross-sectional properties leads to a nearly identical impact on the structure's mass, as evidenced in Figure 5.1. Given these observations, it becomes clear that thickness is the prior parameter in optimisation. Figure 5.13 emphasizes the discussion in Section 4.2.2 stating that in order to minimize the SCFs as much as possible, it would be optimal to reduce the thickness ratio τ . This also holds for the damage and increasing the chord thickness while reducing the brace thickness will reduce the mass until a certain τ ratio.

Though the bending stress sensitivities were not precisely calculated through the pseudo problem, as outlined in Section 5.2.3, the damage sensitivity is provided accurately. This is likely due to the dominant role of axial load stresses, which are less affected by this non-linear effect. Given that axial loads are the primary stress on the beams in a jacket structure, the direct differentiation

method can be effectively performed in FEDEM for accurate damage sensitivity determination. However, it's important to note that this method may not yield precise results in cases such as monopiles, where stresses are primarily attributed to bending rather than axial loads [16].

In Figure 5.16, the damage slopes for hot spots 2 and 3 appear too gentle. A possible reason for this is that the SCFs are influenced by the radius through exponential or trigonometric terms, leading to a potential imprecision in determining SCFs using the least square method. A more accurate slope might be attained by conducting the SCF differentiation analytically. If this method would be used for the chord damage sensitivity, the SCFs are intricately related to the chord cross-section properties as Tables 4.3, 4.4, and 4.5 reveal. Differentiation concerning these properties becomes difficult, and the least square method can be used directly without the logarithmic scale to save computational time.

Figure 5.12 compares the joint in beam 82 connected to the leg classified as a K- and a Y-joint. Equation 4.1 generally holds as evident from Figure 5.12, suggesting that a conservative choice would be to categorise it as a Y-joint. As the thickness decreases, it becomes essential to classify the joint correctly, as this can significantly differ the damage levels under the same loading conditions. An overly conservative joint classification may lead to an unnecessarily costly design.

The damage sensitivity of the overlying beams is evaluated with varying degrees of precision. This variation in outcomes might be attributable to the assumptions integrated into the pseudo problem, as this does not capture the dynamic changes in the structure due to a modification of beam 82. The relative change in damage of the beam compared to the original damage of the structure varies from 0 to above 100 percent as shown in Figure 5.15, this also holds for the other hot spots. The relative change compared to the damage in beam 82 in Figure 5.15 exhibits the same. Ideally, this should be considered in optimization which often simplifies the problem, positing that the optimisation of beam 82 occurs independently without considering damage shifts in other elements. However, the direct differentiation method does not provide the correct load redistribution throughout the structure, likely due to the simplifications made. When optimizing the accuracy achieved by including dynamical sensitivities must be justified by the computational cost required to incorporate these dynamic effects into the pseudo-problem.

Although this thesis does not delve into optimisation, a commonality across most hot spots is observing a minimum damage point occurring at a thickness of approximately 0.055 m. This minimum is due to the SCFs increasing with the thickness while the axial stresses are decreasing with the thickness, together creating a parabolic curve. However, the damage in beam 82 concerning the radius and the overlying beams in relation to the thickness of beam 82 do not exhibit an explicit minimum. The gradient signs in these depend on the considered hot spot.

6 Conclusion

For the final discussion, it is natural to restate the research question defined in Section 1.3:

Q: Can the direct differentiation method, in conjunction with the flexibility method, accurately ascertain the damage sensitivity of the welded joints in the X-rotor jacket?

Validation of the flexibility method in FEDEM revealed that the stiffness is nonlinear as the force-displacement response gets a distinct "square" characteristic in static structural analysis. The generalised Hooke's law $\mathbf{F}=\mathbf{K}\mathbf{u}$ does not capture this non-linear effect. Hence the flexibility method demands more computational resources than the marginal accuracy achieved. According to Kollbein Bell [4], using the flexibility method to calculate the stiffness matrix is sensitive to rounding errors. This issue arises even when determining the stiffness matrix for even a single element within a complex structure. Hence, the direct differentiation method utilizes the analytical stiffness matrix derived from an Euler-Bernoulli beam, given its significant resemblance to the numerical matrix. Even though the flexibility method did not yield a precise stiffness matrix, it uncovered a critical source of error in the direct differentiation method, a discovery that may have been detected otherwise. This underlines the method's utility in providing valuable insights beyond its primary purpose.

Since jacket structures primarily experience axial loading in the beams, the direct differentiation method reliably estimates the sensitivities. However, FEDEM does not correctly calculate stress sensitivities for bending moments due to the non-linear effect discussed above affecting the quasi-static pseudo problem. This may significantly impact the results for structures like monopiles, where bending moment stresses are significant [16].

SCFs are essential in defining the HSS and, consequently, the damage. As such, initiating the optimisation process by reducing SCFs can be beneficial. The thickness has a more significant influence on SCFs than the radius, and a decrease in brace thickness leads to a decrease in SCFs. In contrast, increasing chord thickness decreases the SCFs; an optimal design approach would aim to reduce the ratio between brace and chord thickness τ . This will also reduce the mass until a certain balance resulting in a feasible design with both low mass and damage.

The assumptions made within the direct differentiation method harmonise computational efficiency with the precision in damage sensitivity estimation, confirming it as feasible. However, it is found that the redistribution of loads in the structure due to modification of one beam is captured to a certain extent by the pseudo displacements. When optimizing the accuracy achieved by including dynamical sensitivities must be justified by the computational cost required to incorporate these dynamic effects into the pseudo-problem.

In conclusion, the direct differentiation method, using the analytical stiffness matrix, successfully determines the damage sensitivity of the welded joints in the X-rotor jacket. This enables achieving a feasible design without needing load recalculation during optimisation. However, one must remember that the relationship between damage and cross-sectional properties is non-linear. This becomes vital when deciding how frequently the pseudo-problem should be evaluated. Relying on the damage gradient to predict damage for larger variable steps can sometimes result in inaccuracies. Being aware of and accounting for this fact will improve the accuracy of future damage predictions.

6.1 Possibilities for future research

The design sensitivity analysis conducted in this thesis paves the way for a wide range of future research opportunities, most notably, it lays a foundation for the optimisation of the X-rotor jacket structure. In addition, several aspects of the design sensitivity analysis could be further investigated and are outlined in the list below.

- Create an interface between MATLAB and FEDEM. This would increase the computational speed significantly.
- Include the sensitivity of the external load, such as the wave load and marine growth, which depends on the diameter of the jacket beams.
- Examine whether incorporating dynamic sensitivities might more accurately represent the load redistribution within the structure in the pseudo problem. This should be weighed against the implications on computational resources.
- Identifying the sensitivities of additional boundary constraints, such as those from ultimate limit state conditions and frequency analysis of the beams within the jacket structure, which is critical for the effective optimization of the jacket aiming for a truly feasible design.
- Find damage sensitivity due to other parameters of the jacket, such as the angle of the legs, which will affect the length and angle of the beams.
- Research further the non-linear effect in FEDEM. And include the shear coefficients both in the analytical or numerical stiffness matrix to account for the shear deformation and warping effects in thin-walled beams.
- Enhancing the robustness of the joints by increasing the thickness and diameter around the joints, incorporating joint caps, and determining the impact of this strengthening on damage sensitivity.

Bibliography

- [1] Abbas Kazemi Amiri and James Carroll. *X-Rotor, an Innovative Offshore Wind Turbine. Background and Draft Design Configurations*. Tech. rep. Glasgow: University of Strathclyde, 2021.
- [2] ASTM International. *ASTM E1049-85(2017) Standard Practices for Cycle Counting in Fatigue Analysis*. 2017.
- [3] O. A. Bauchau and J. I. Craig. *Euler-Bernoulli beam theory*. 2009. DOI: 10.1007/978-90-481-2516-6_5.
- [4] Kolbein Bell. *Matrisestatikk*. 4th ed. Vol. 1. Bergen: Fagbokforlaget, 2018.
- [5] Anil K. Chopra. *Dynamics of Structures, Theory and Applications to Earthquake Engineering*. Vol. 5. 1. 2020.
- [6] Adriana Correia da Silva and Michael Muskulus. *X-rotor Design basis - WP4 Design of Mechanical Structure and Analysis*. Tech. rep. Trondheim: Norwegian University of Science and Technology NTNU, 2021.
- [7] DNV. *DNV-RP-C205 Environmental Conditions and Environmental Loads*. 2010.
- [8] DNV GL. *DNVGL-OS-C101: Design of Offshore Steel Structures, General - LRFD Method*. 2015.
- [9] DNV GL. *DNVGL-RP-C203: Recommended Practice - Fatigue design of offshore steel structures*. 2016.
- [10] C.H. Edwards and Penney David E. *Elementary linear algebra*. Englewood Cliffs, N.J: Prentice Hall, 1988.
- [11] Fedem Technology AS. *Fedem Release 7.2.1 User's Guide*. Tech. rep. Trondheim, 2016.
- [12] Fedem Technology AS. *FEDEM Windpower R7.2.2*. 2018.
- [13] T. Fischer, W.E. De Vries and B. Schmidt. *Upwind design basis (WP4: Offshore foundations and support structures)*. Tech. rep. Stuttgart, Germany: Project Upwind, 2011.
- [14] Benedicte Hexeberg Hammerstad, Sebastian Schafhirt and Michael Muskulus. ‘On Fatigue Damage Assessment for Offshore Support Structures with Tubular Joints’. In: *Energy Procedia 94* (2016), pp. 339–346. DOI: 10.1016/j.egypro.2016.09.193.
- [15] K. Hasselmann et al. *Measurements of wind-wave growth and swell decay during the joint North Sea wave project (JONSWAP)*. 1973.
- [16] Saleh Jalbi and Subhamoy Bhattacharya. ‘Concept design of jacket foundations for offshore wind turbines in 10 steps’. In: *Soil Dynamics and Earthquake Engineering 139* (2020). DOI: 10.1016/j.soildyn.2020.106357.
- [17] Aslam Kassimali. *Matrix Analysis of Structures*. Vol. 1. Carbondale: Cengage Learning, 1999, pp. 451–483.
- [18] Jaan Kiusalaas. *Numerical Methods in Engineering with MATLAB®*. New York: Cambridge University Press, 2005. DOI: 10.1017/cbo9780511614682.
- [19] William Leithead et al. ‘The X-Rotor Offshore Wind Turbine Concept’. In: *Journal of Physics: Conference Series 1356*. 2019. DOI: 10.1088/1742-6596/1356/1/012031.
- [20] Lin Li, Zhen Gao and Torgeir Moan. ‘Joint Distribution of Environmental Condition at Five European Offshore Sites for Design of Combined Wind and Wave Energy Devices’. In: *Journal of Offshore Mechanics and Arctic Engineering 137.3* (2015). DOI: 10.1115/1.4029842.
- [21] Michael E. McCormick. *Ocean engineering mechanics: With applications*. 2009, pp. 137–145. DOI: 10.1017/CBO9780511812309.

- [22] Milton A. Miner. ‘Cumulative Damage in Fatigue’. In: *Journal of Applied Mechanics, Transactions ASME* 12 (1945), pp. 71–105. DOI: 10.1115/1.4009458.
- [23] Yukitaka Murakami et al. ‘Essential structure of S-N curve: Prediction of fatigue life and fatigue limit of defective materials and nature of scatter’. In: *International Journal of Fatigue* 146 (2021). ISSN: 01421123. DOI: 10.1016/j.ijfatigue.2020.106138.
- [24] Bui Duc Nha. *Mathcha Website*. 2022. URL: <https://www.mathcha.io/editor>.
- [25] Jacob Oest et al. ‘On gradient-based optimization of jacket structures for offshore wind turbines’. In: *Wind Energy* 21.11 (2018), pp. 953–967. DOI: 10.1002/we.2206.
- [26] Jacob Oest et al. ‘Structural optimization with fatigue and ultimate limit constraints of jacket structures for large offshore wind turbines’. In: *Structural and Multidisciplinary Optimization* 55.3 (2017), pp. 779–793. DOI: 10.1007/s00158-016-1527-x.
- [27] Lars Einar Sørensen Stieng. ‘Optimal design of offshore wind turbine support structures under uncertainty - Towards a framework for practical reliability-based design optimization’. PhD thesis. Trondheim: NTNU, 2020.
- [28] The MathWorks Inc. *MATLAB (R2020b)*. 2020.
- [29] The MathWorks Inc. *Rainflow - rainflow counts for fatigue analysis*. 2017. URL: <https://se.mathworks.com/help/signal/ref/rainflow.html>.
- [30] Kurt E. Thomsen. *OFFSHORE WIND A Comprehensive Guide to Successful Offshore Wind Farm Installation*. 2014, pp. 272–274.
- [31] D. A. Tortorelli and P. Michaleris. ‘Design sensitivity analysis: Overview and review’. In: *Inverse Problems in Engineering* 1 (1994). DOI: 10.1080/174159794088027573.

Appendix

- Appendix A: Stress concentration factors
- Appendix B: Damage sensitivity in hot spots of other brace beams as beam 82 is changed
- Appendix C: Damage sensitivity with respect to brace thickness
- Appendix D: Linear regression to find SCF sensitivity for SCF 5

A Stress concentration factors

A.1 SCF 3D-plots dependent on cross-section properties

Y-joint

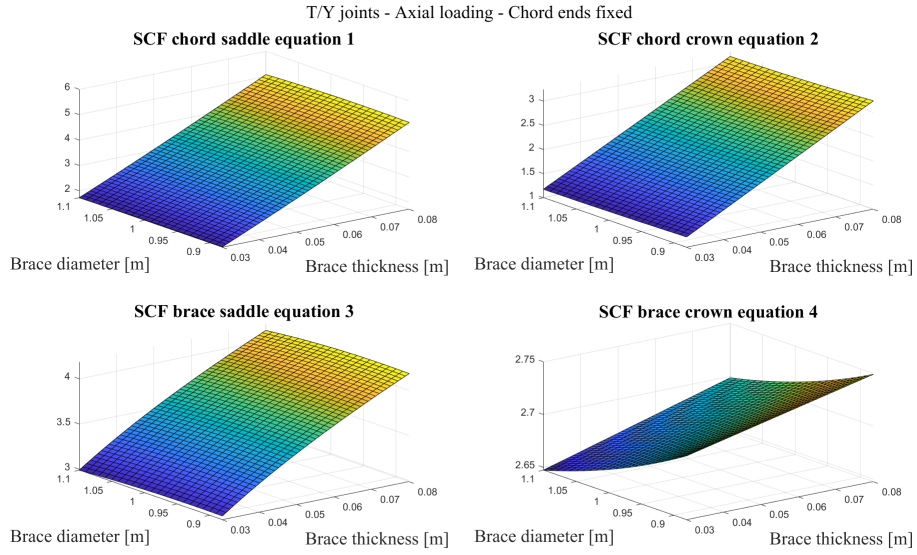


Figure B.1: T/Y-joint for axial loading with chord ends fixed as a function of brace thickness and diameter

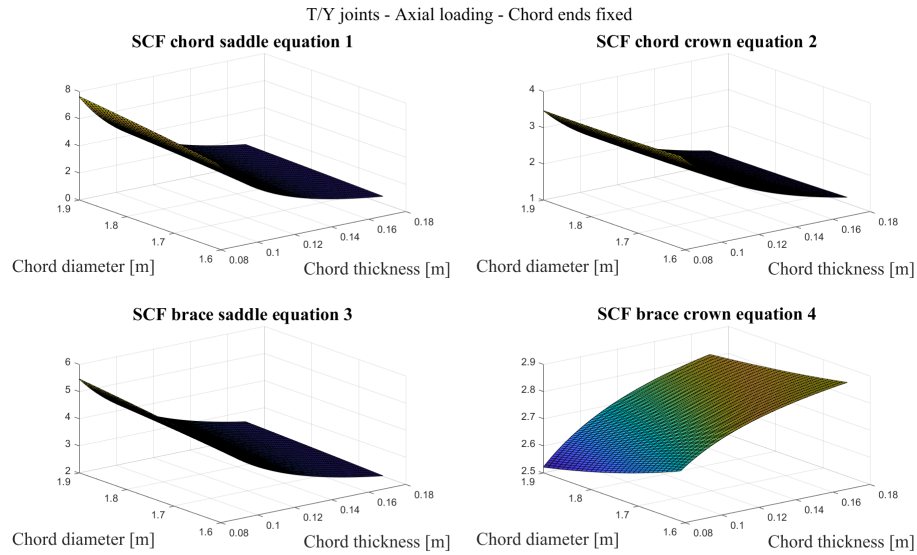


Figure B.2: T/Y-joint for axial loading with chord ends fixed as a function of chord thickness and diameter

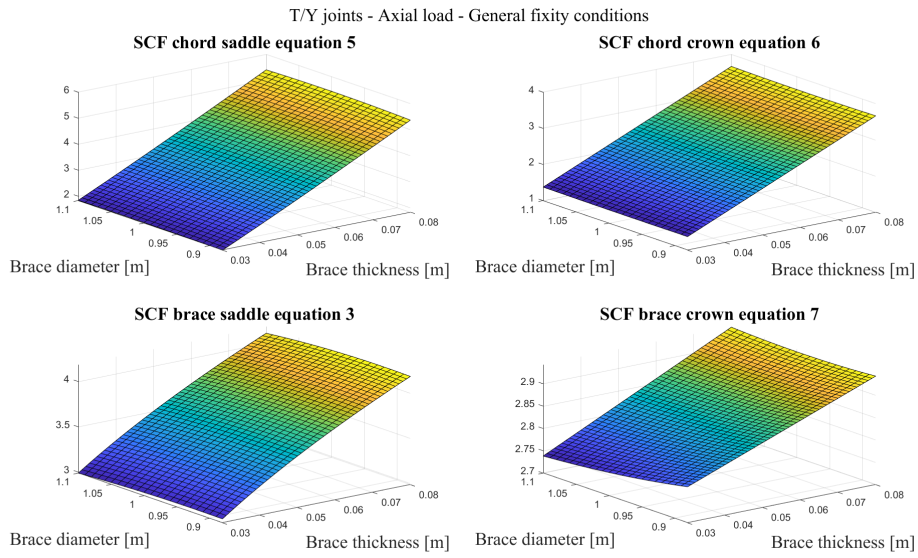


Figure B.3: T/Y-joint for axial loading with general fixity conditions as a function of brace thickness and diameter

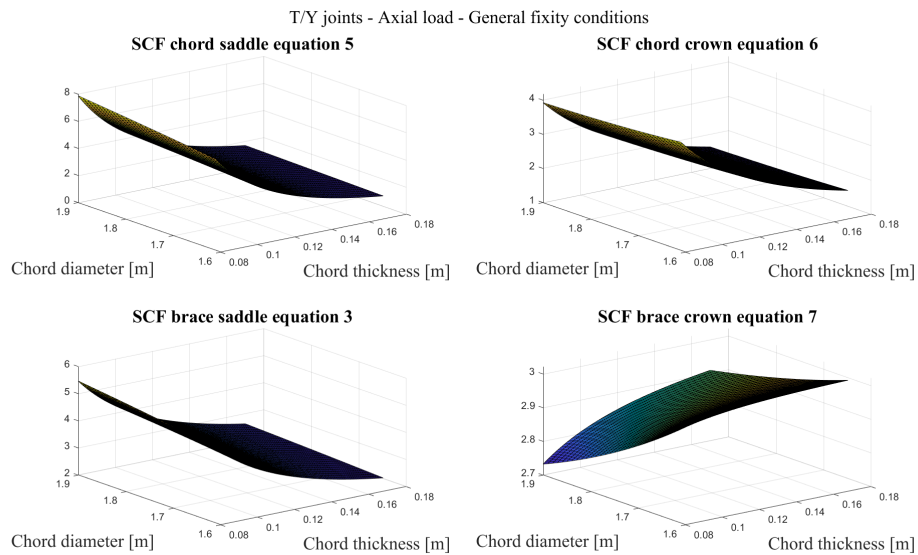


Figure B.4: T/Y-joint for axial loading with general fixity conditions as a function of chord thickness and diameter

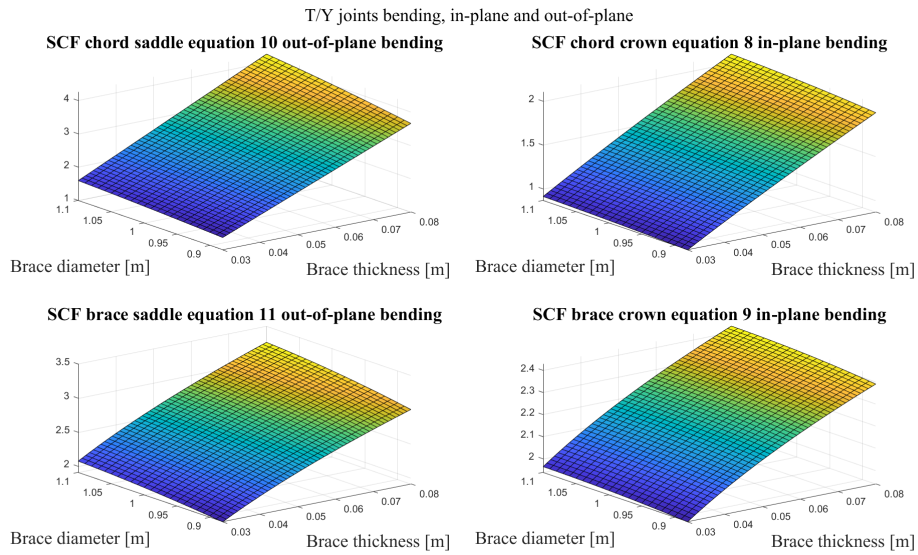


Figure B.5: T/Y-joint for bending, in-plane and out-of-plane, as a function of brace thickness and diameter

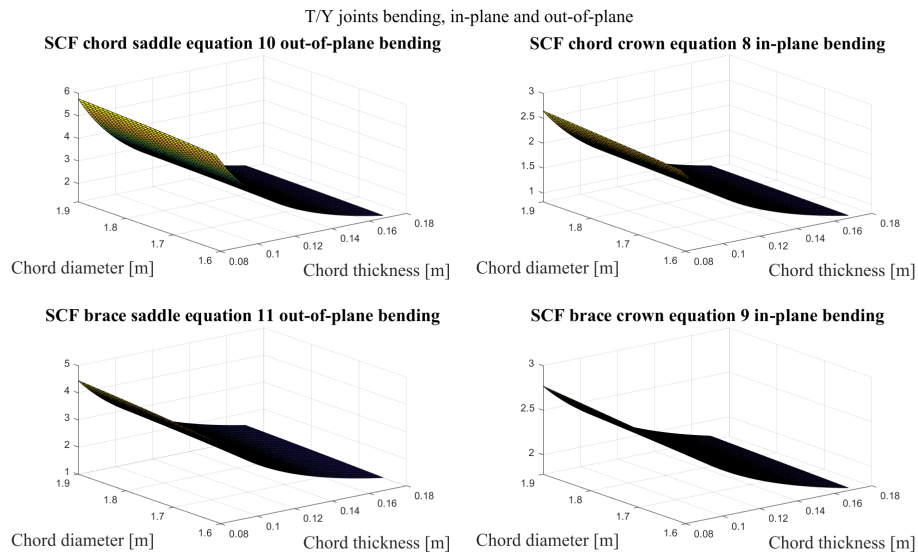


Figure B.6: T/Y-joint for bending, in-plane and out-of-plane, as a function of chord thickness and diameter

X-joint

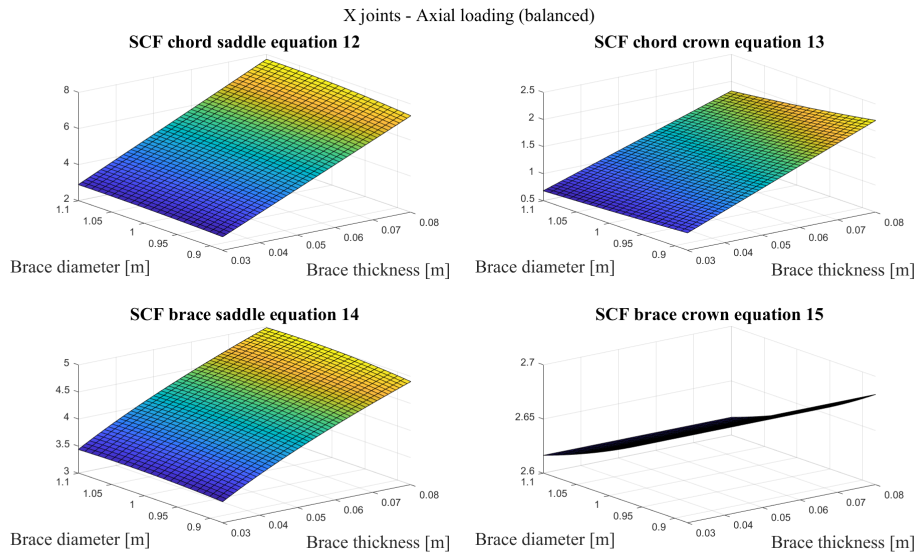


Figure B.7: X-joint for balanced axial loading as a function of brace thickness and diameter

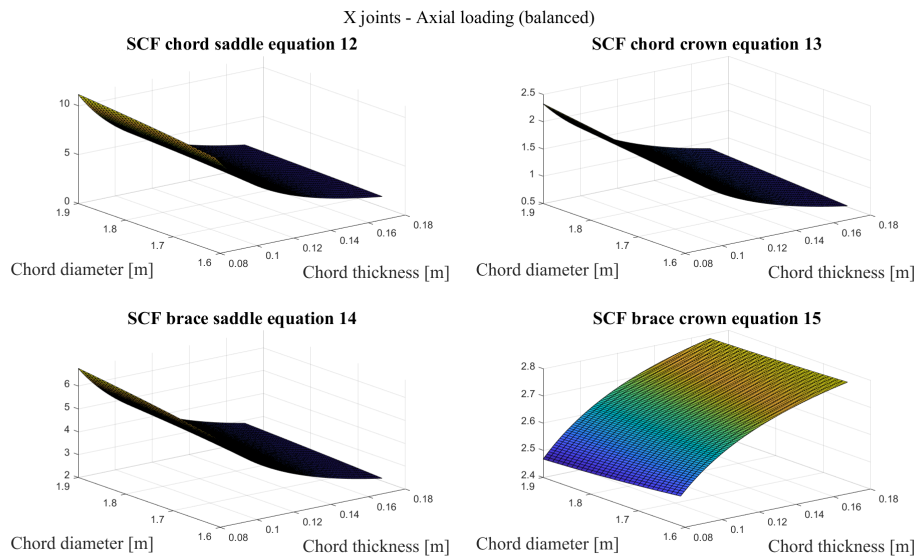


Figure B.8: X-joint for balanced axial loading as a function of chord thickness and diameter

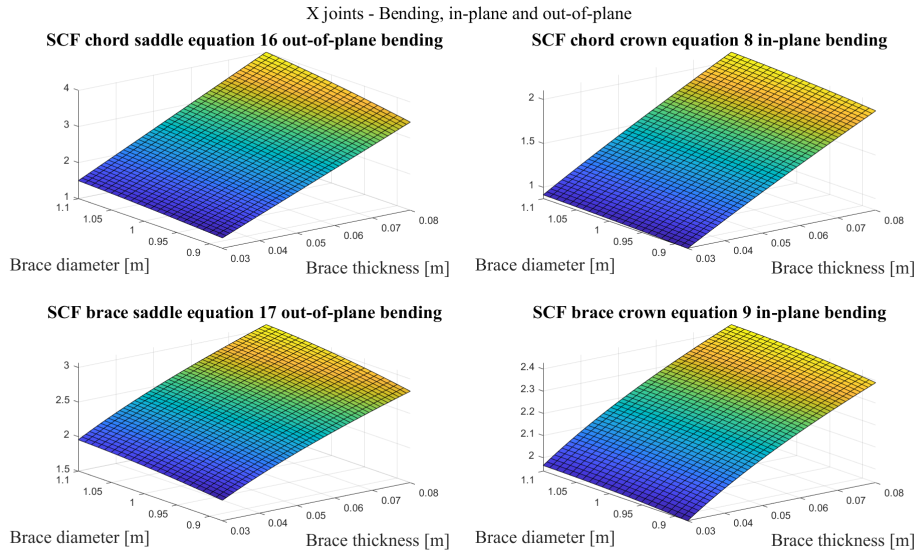


Figure B.9: X-joint for bending, in-plane and out-of-plane, as a function of brace thickness and diameter

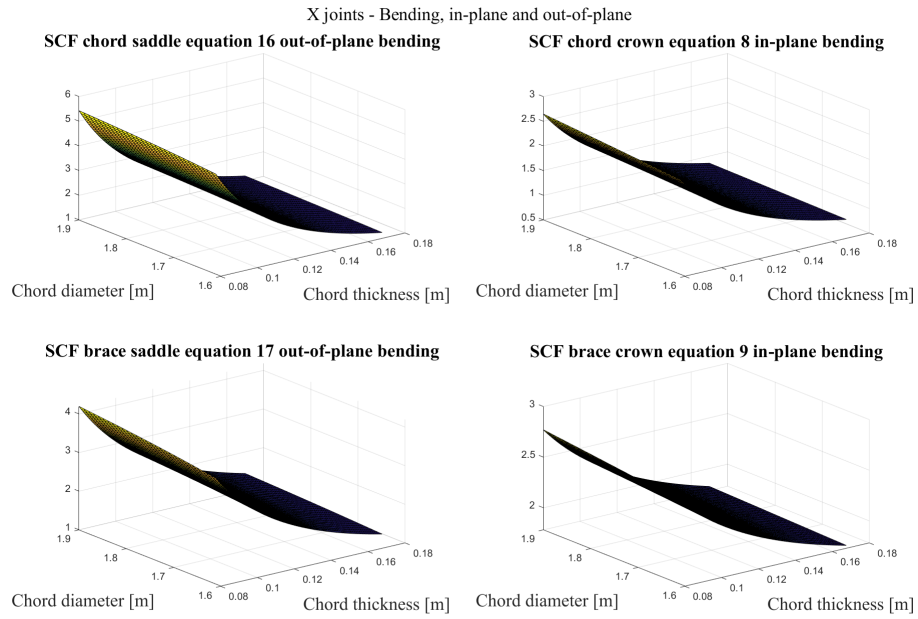
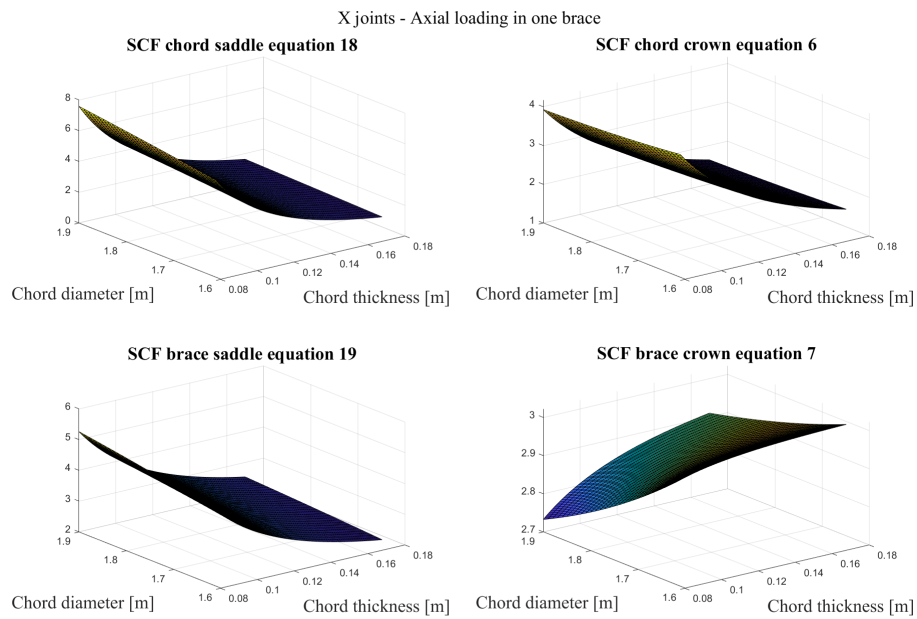
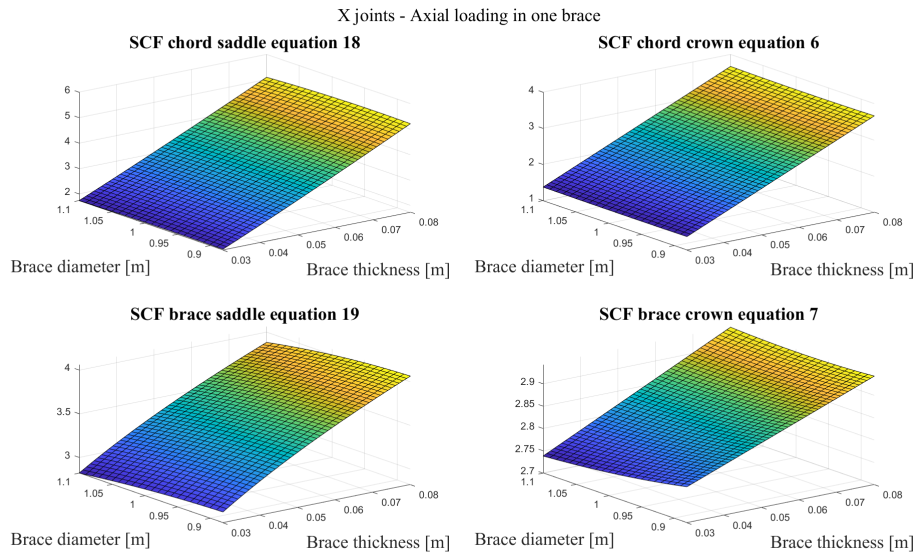


Figure B.10: X-joint for bending, in-plane and out-of-plane, as a function of chord thickness and diameter



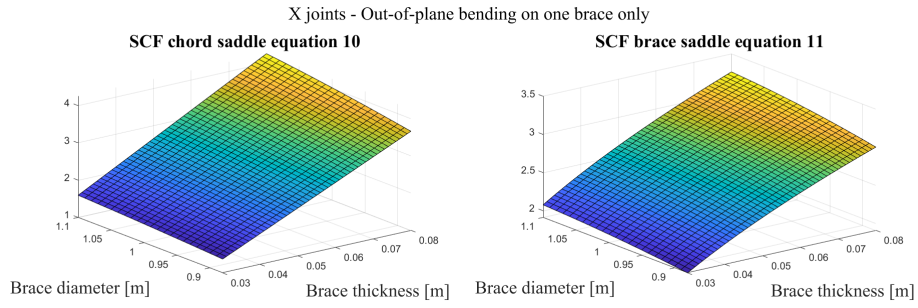


Figure B.13: X-joint for out-of-plane bending on one brace as a function of brace thickness and diameter

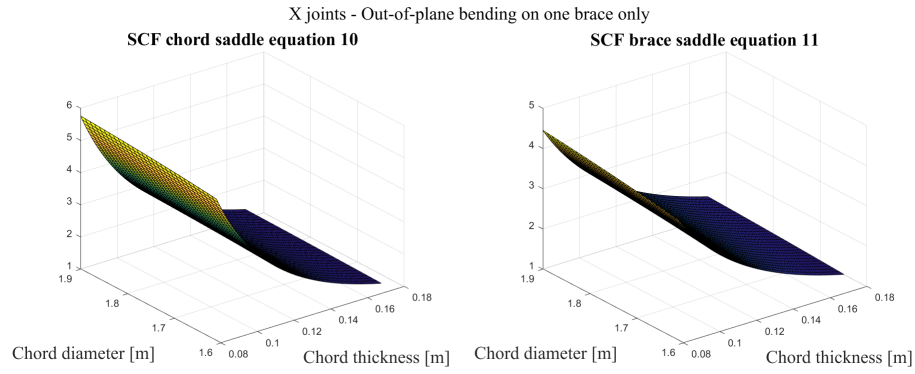


Figure B.14: X-joint for out-of-plane bending on one brace as a function of chord thickness and diameter

K-joint

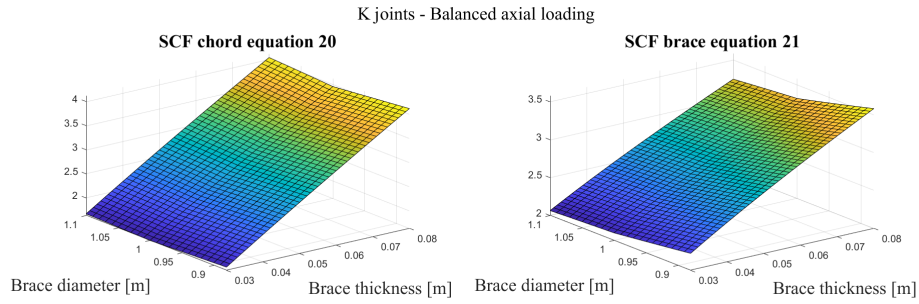


Figure B.15: K-joint for balanced axial loading as a function of brace thickness and diameter

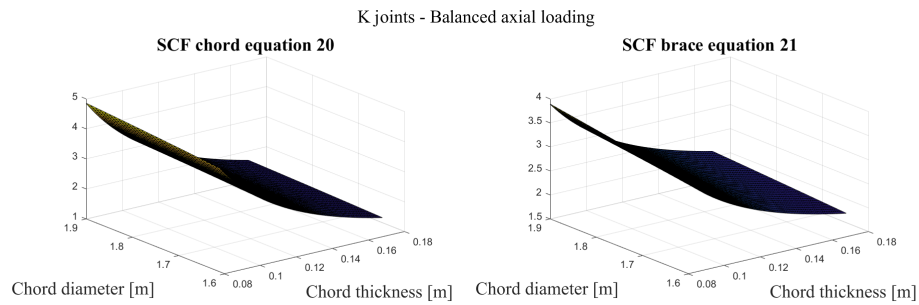


Figure B.16: K-joint for balanced axial loading as a function of chord thickness and diameter

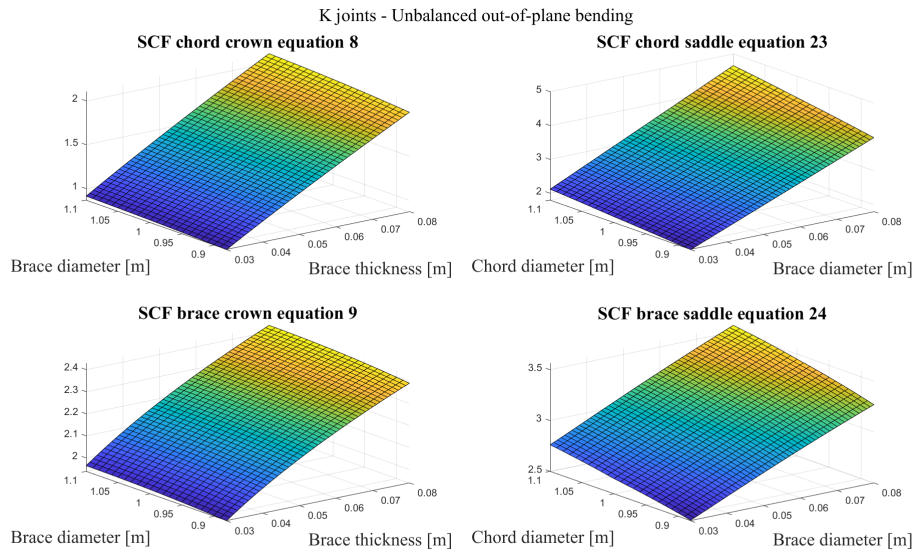


Figure B.17: K-joint for unbalanced bending, in-plane and out-of-plane, as a function of brace thickness and diameter

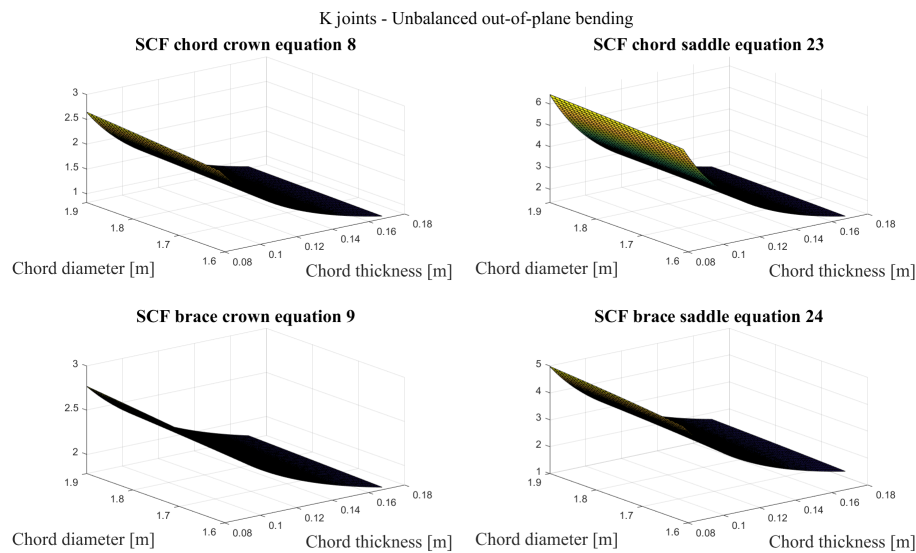


Figure B.18: K-joint for unbalanced bending, in-plane and out-of-plane, as a function of chord thickness and diameter

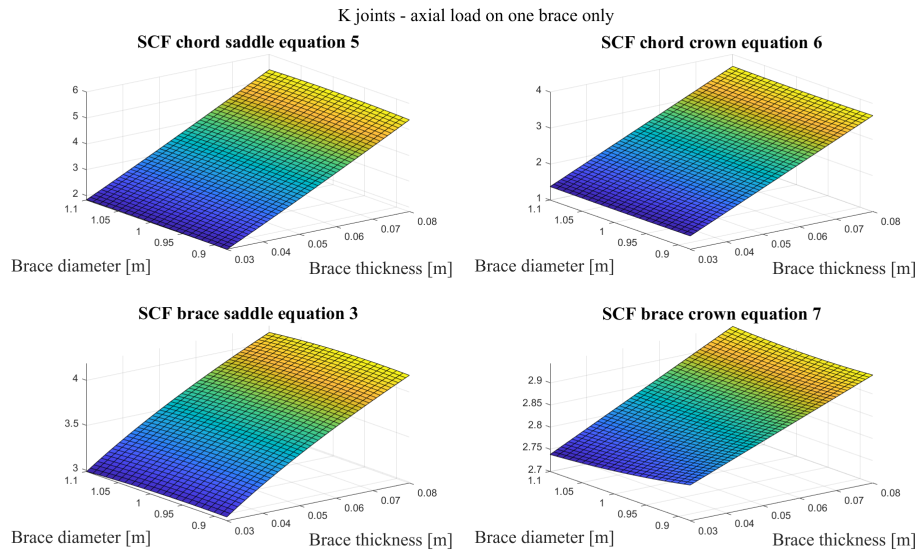


Figure B.19: K-joint for axial loading in one brace as a function of brace thickness and diameter

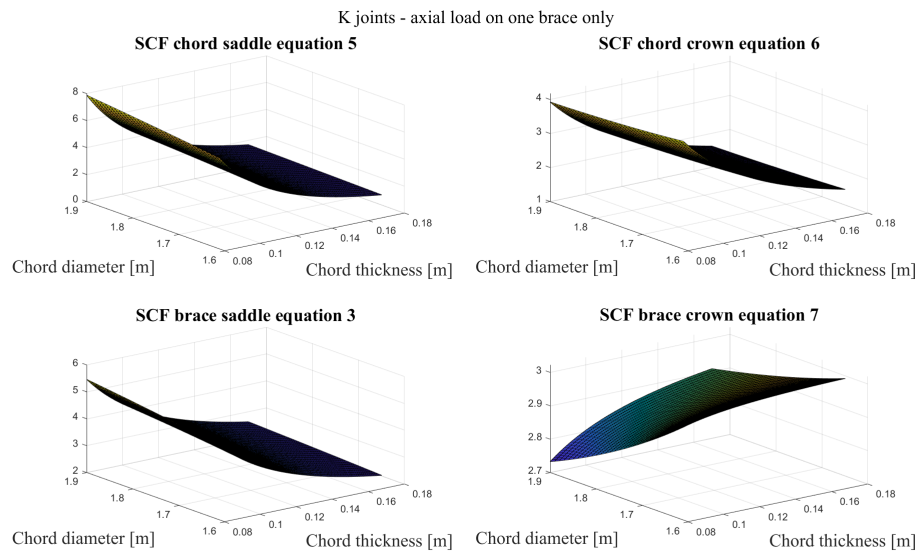
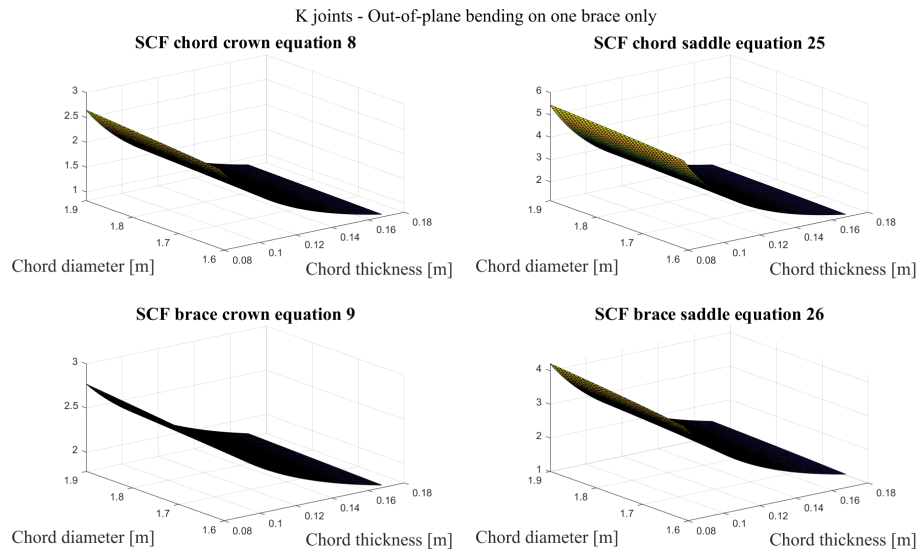
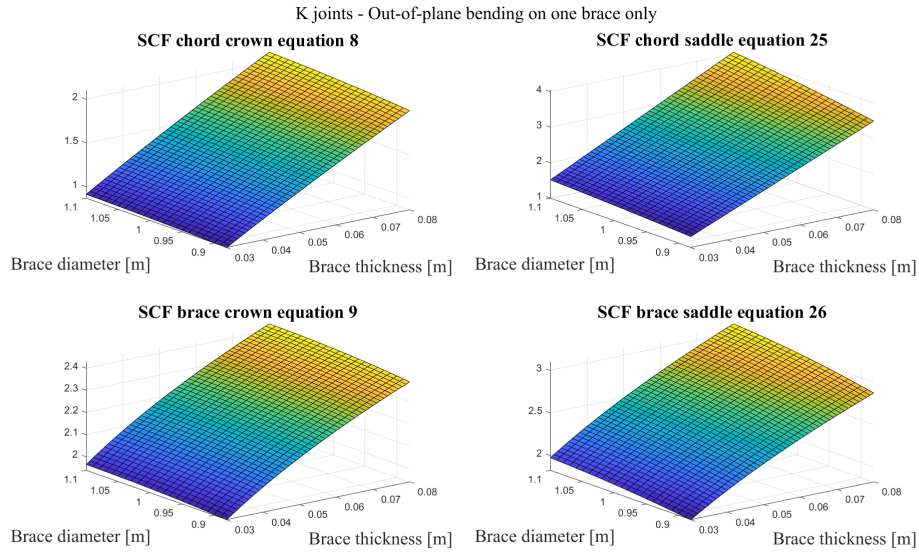


Figure B.20: K-joint for axial loading in one brace as a function of chord thickness and diameter



A.2 SCF range plots dependent on cross-section properties

Y-joint

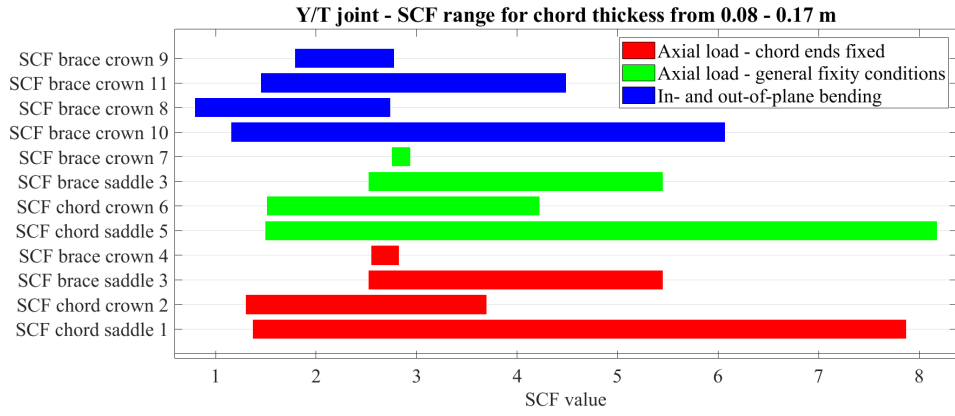


Figure B.23: Y-joint SCF range for chord thickness

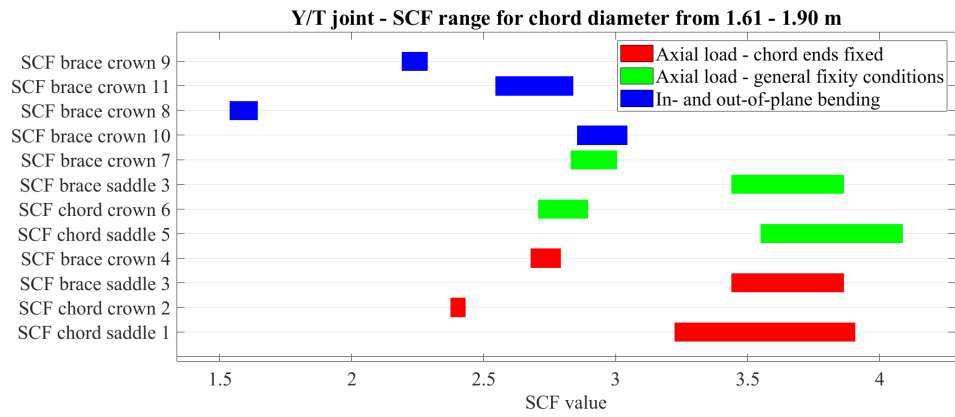


Figure B.24: Y-joint SCF range for chord diameter

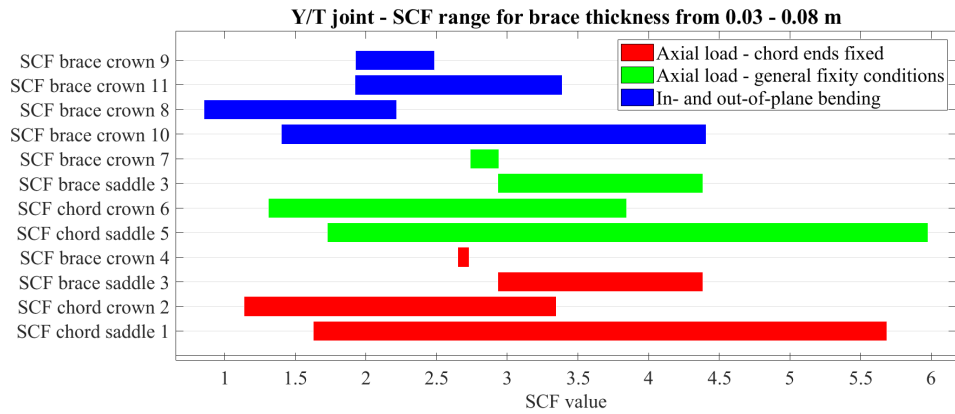


Figure B.25: Y-joint SCF range for brace thickness

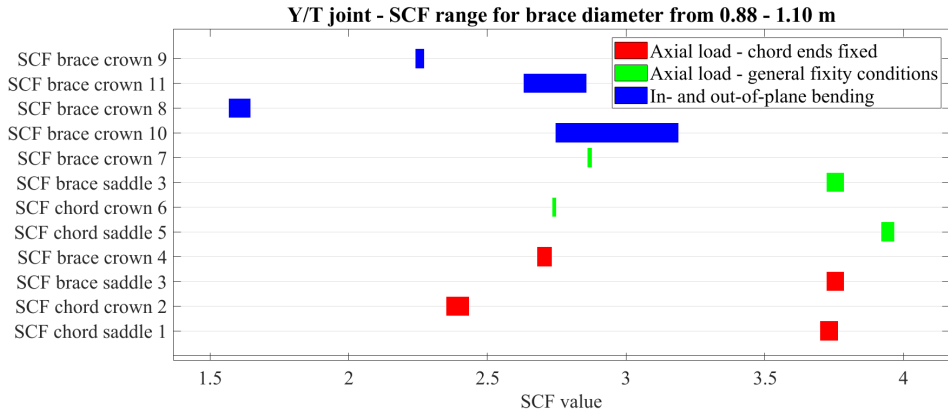


Figure B.26: X-joint SCF range for brace diameter

X-joint

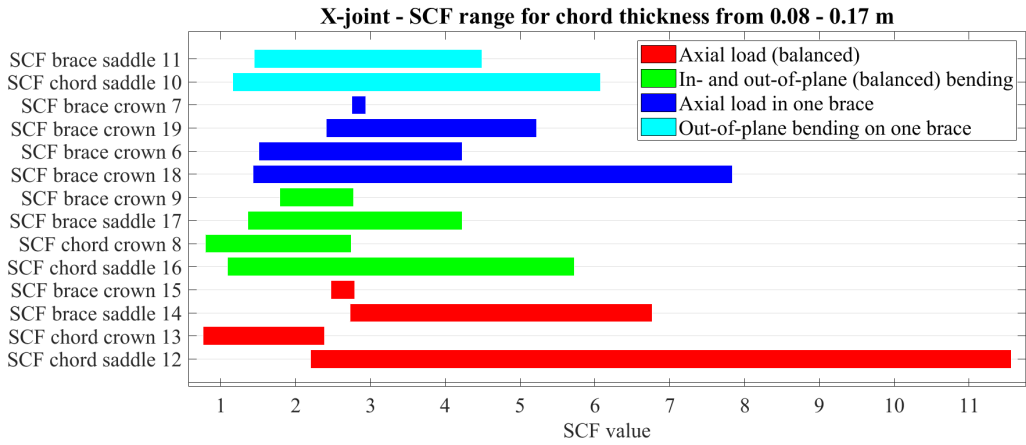


Figure B.27: X-joint SCF range for chord thickness

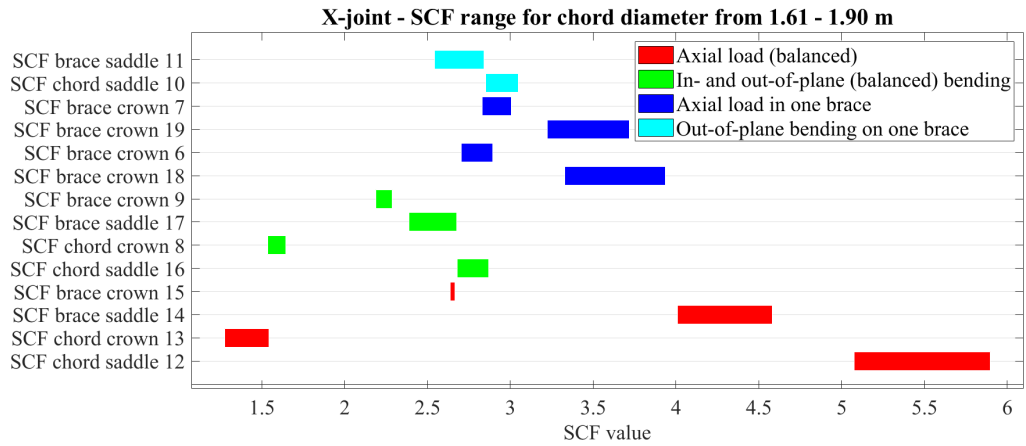


Figure B.28: X-joint SCF range for chord diameter

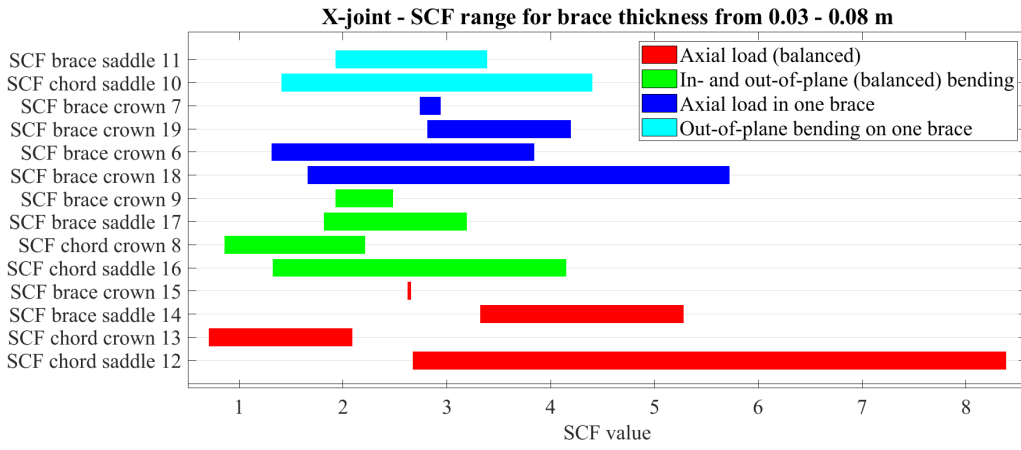


Figure B.29: X-joint SCF range for brace thickness

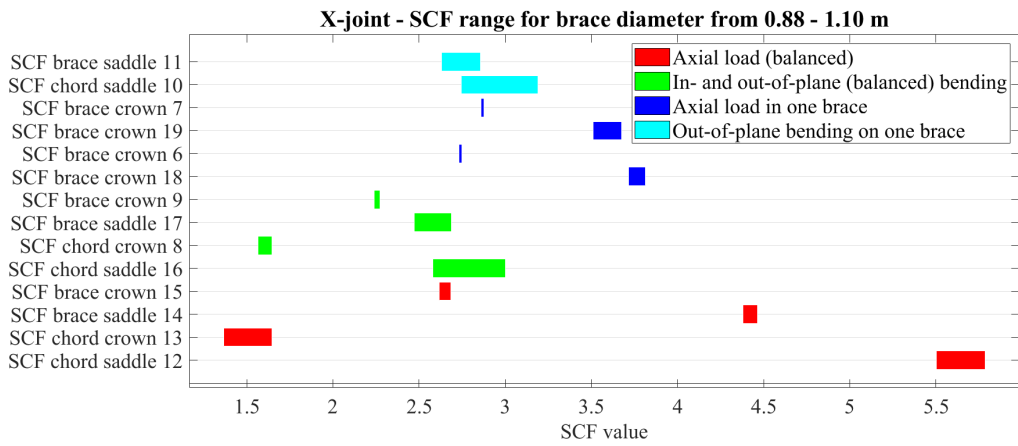


Figure B.30: X-joint SCF range for brace diameter

K-joint

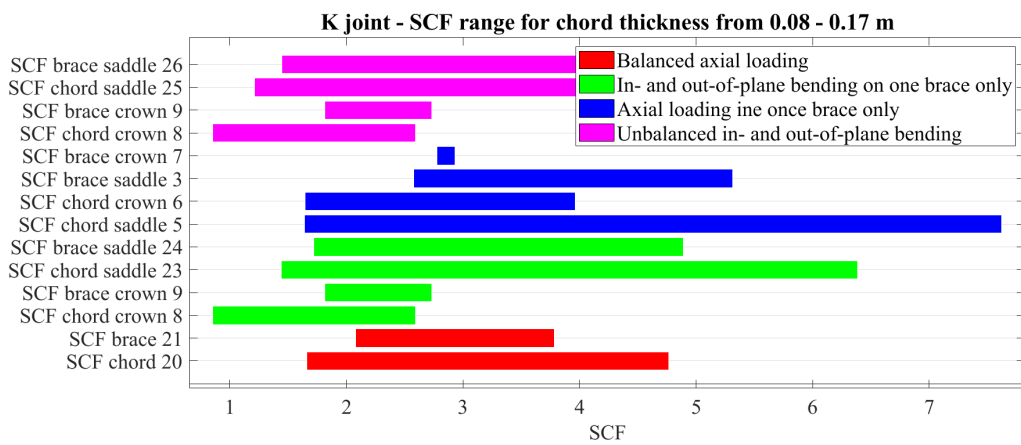


Figure B.31: K-joint SCF range for chord thickness

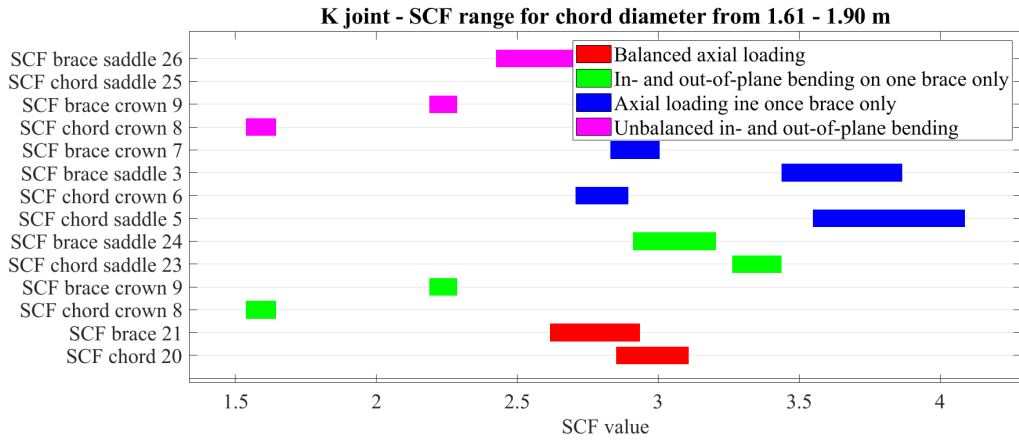


Figure B.32: K-joint SCF range for chord diameter

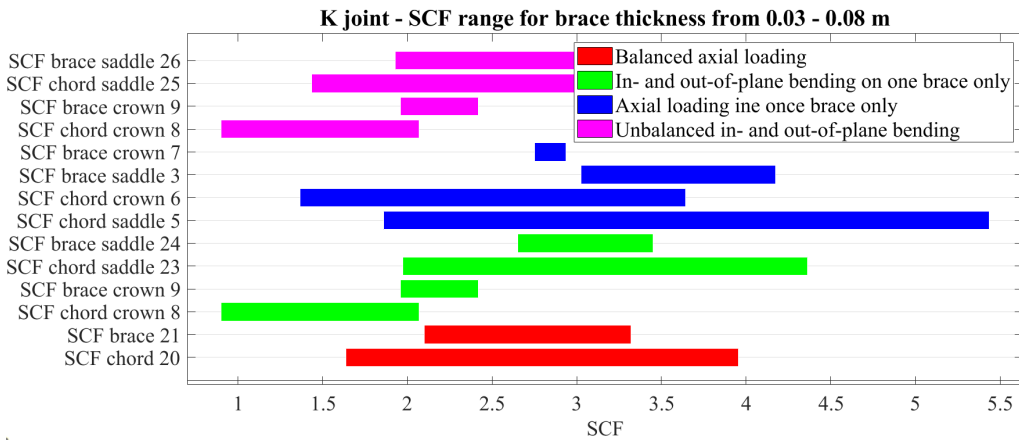


Figure B.33: K-joint SCF range for brace thickness

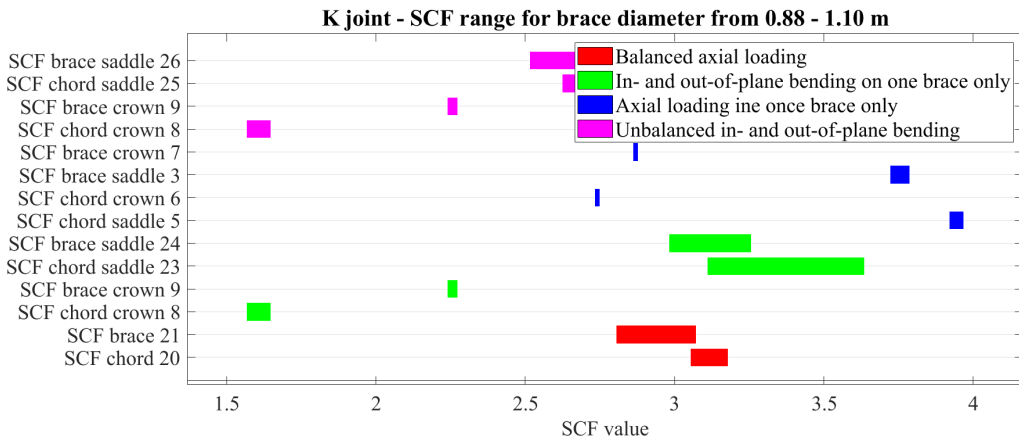


Figure B.34: K-joint SCF range for brace diameter

B Damage sensitivity in hot spots of other brace beams as beam 82 is changed

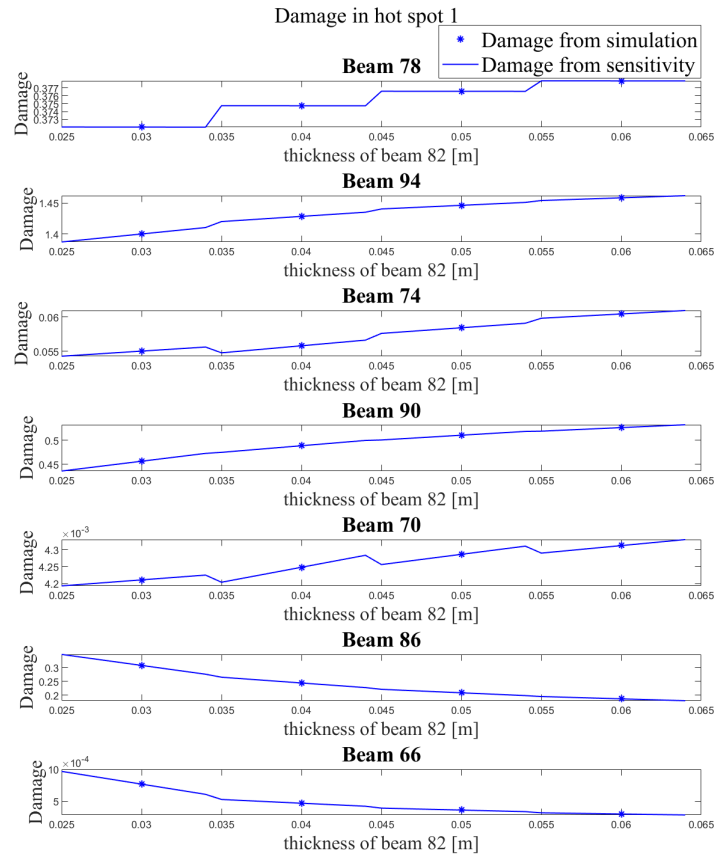


Figure C.1: Damage and damage sensitivity of HSS1 in beams shown in Figure . The joint considered are the joint connected to the leg.

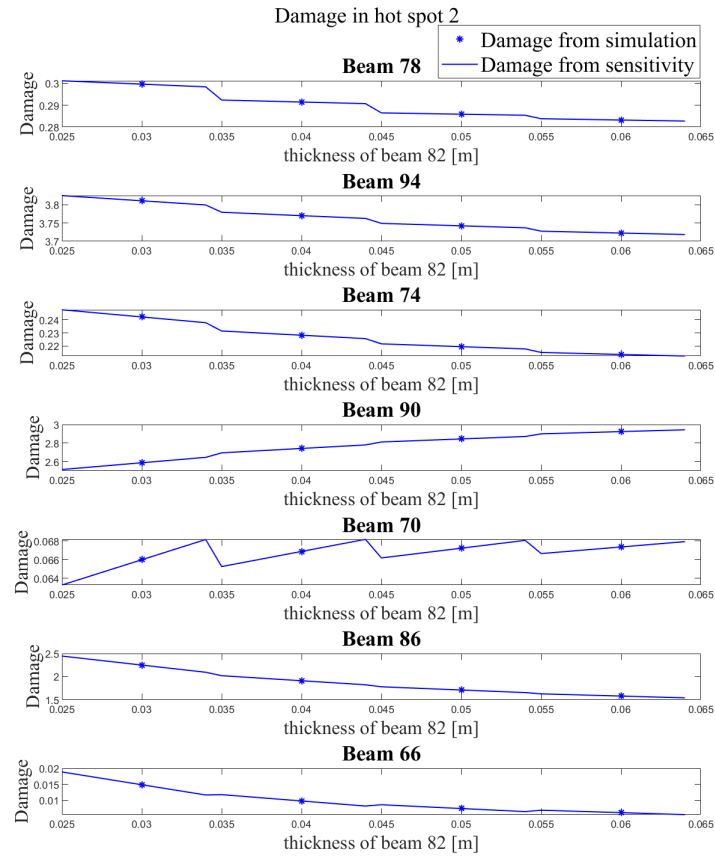


Figure C.2: Damage and damage sensitivity of HSS2 in beams shown in Figure . The joint considered are the joint connected to the leg.

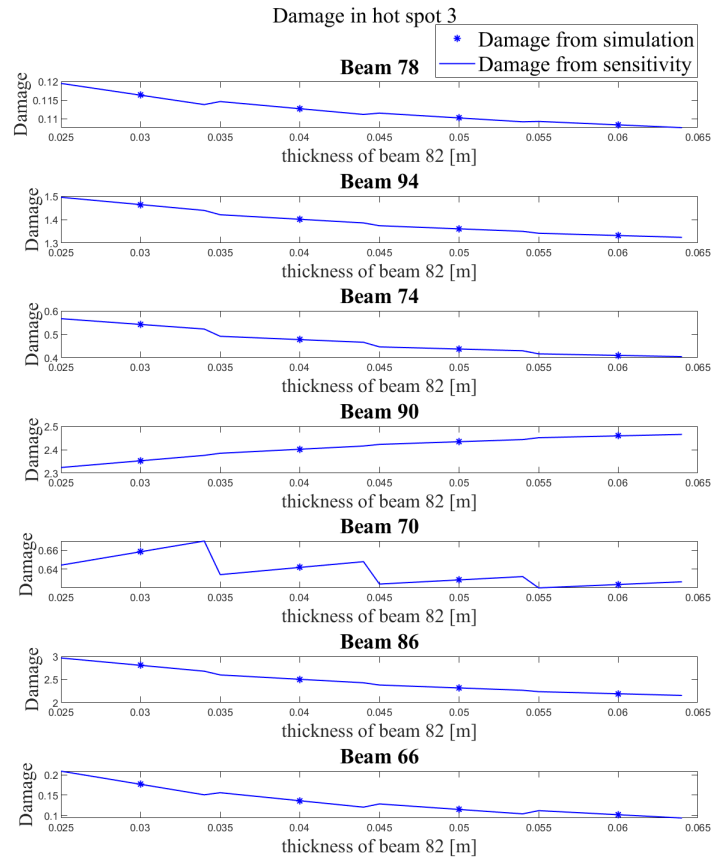


Figure C.3: Damage and damage sensitivity of HSS3 in beams shown in Figure . The joint considered are the joint connected to the leg.

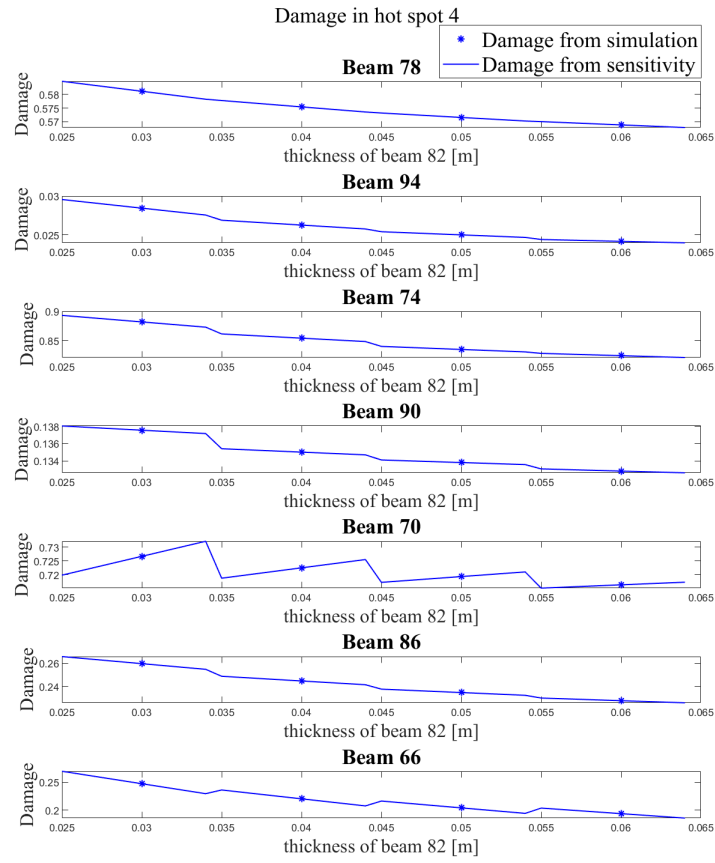


Figure C.4: Damage and damage sensitivity of HSS4 in beams shown in Figure . The joint considered are the joint connected to the leg.

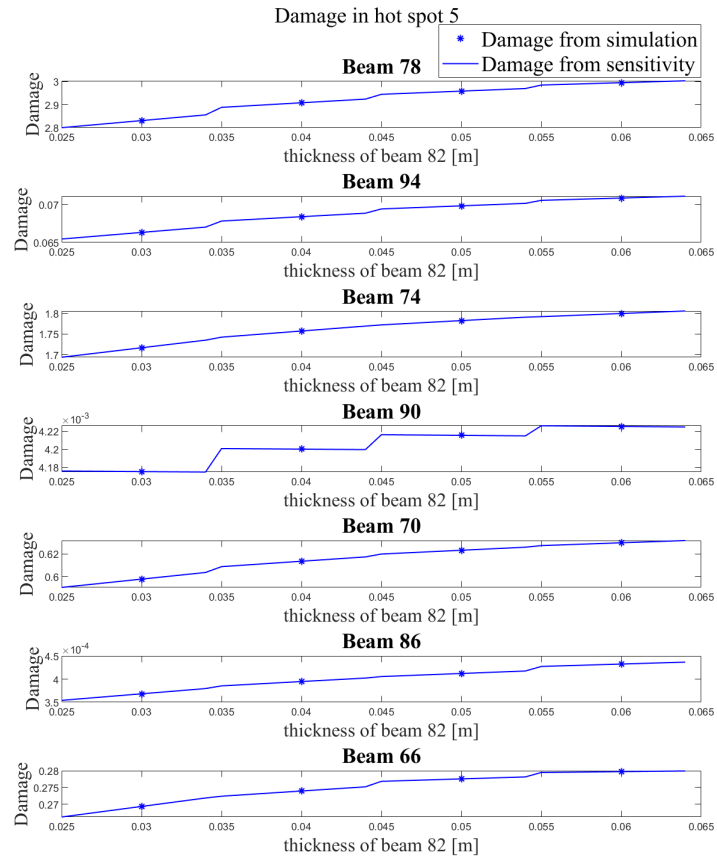


Figure C.5: Damage and damage sensitivity of HSS5 in beams shown in Figure . The joint considered are the joint connected to the leg.

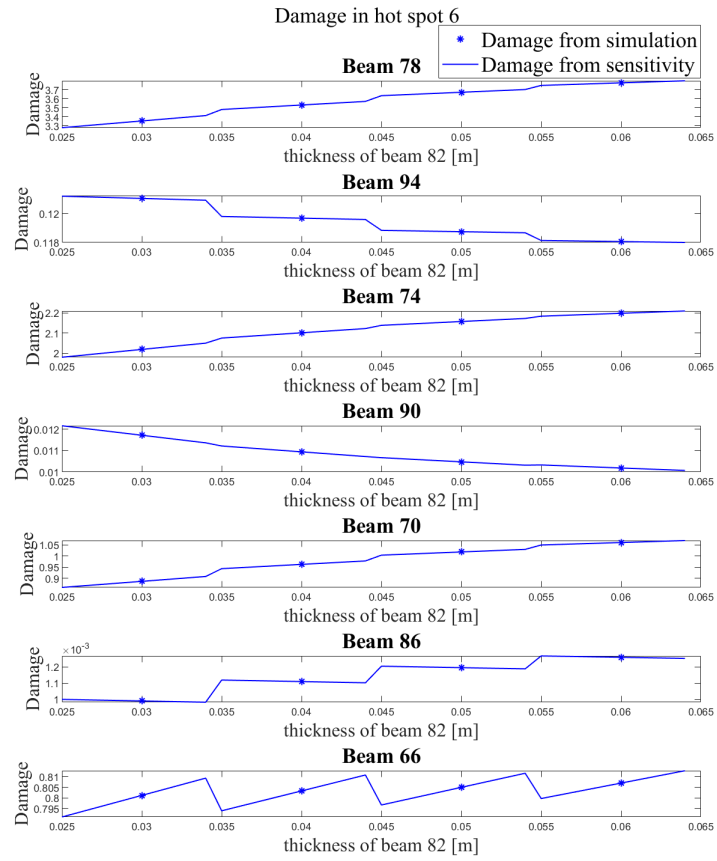


Figure C.6: Damage and damage sensitivity of HSS6 in beams shown in Figure . The joint considered are the joint connected to the leg.

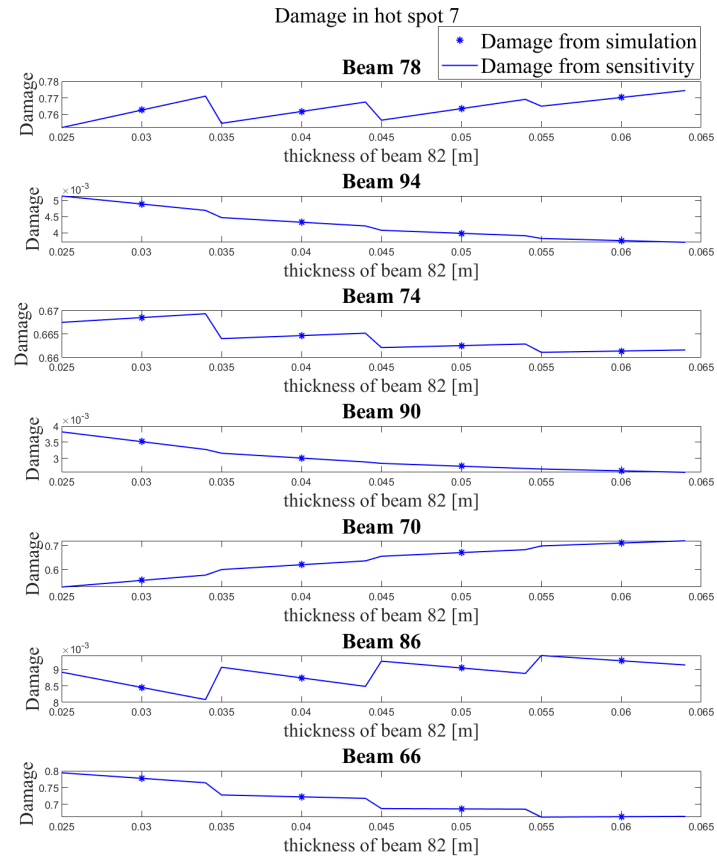


Figure C.7: Damage and damage sensitivity of HSS7 in beams shown in Figure . The joint considered are the joint connected to the leg.

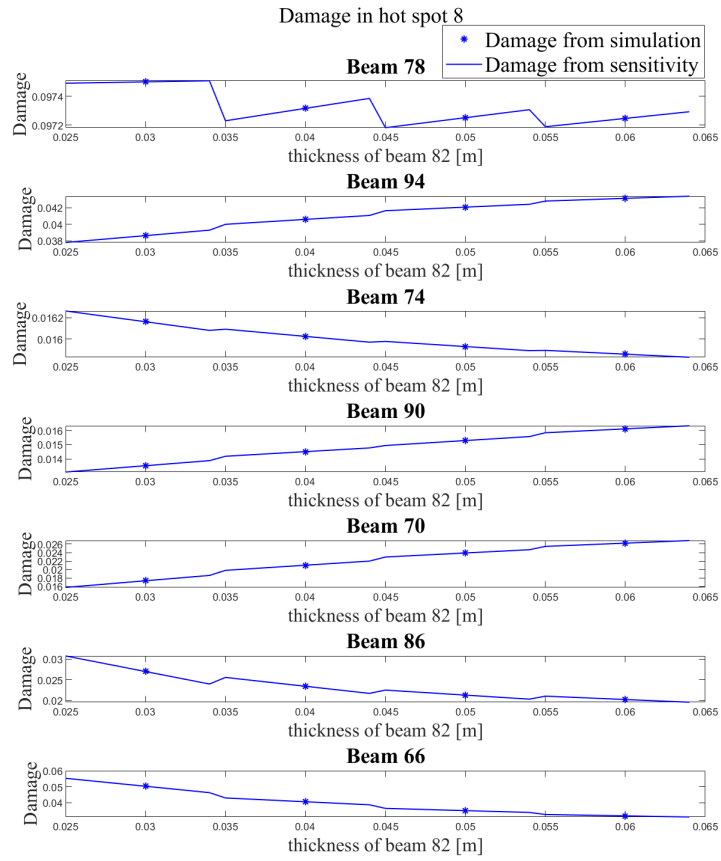


Figure C.8: Damage and damage sensitivity of HSS8 in beams shown in Figure . The joint considered are the joint connected to the leg.

C Damage sensitivity with respect to brace thickness

```

%% geometry of beam 82

triad11 = [ 14.935558, 14.935558, 2.9440421]; % node where joint
         is dimensioned, node 1 of beam 82
triad46 = [ 14.327, 0, 9.498]; % node 2 of beam 82
triad15 = [ 13.766111, 13.766111, 15.538989]; % node 2 of
         connected chord

vec1 = triad46-triad11;
vec2 = triad15-triad11;

theta = rad2deg(acos(dot(vec1, vec2)/(norm(vec1)*norm(vec2)))) %
        angled of joint, used in SCF calculation

%% rotation matrix

triad1 = triad11
triad2 = triad46
z = [-696.02687, 0.0010365615, -64.626159]; % local z-axis defined
        in FEDEM

[R, L] = rotationmatrix(z,triad1,triad2) % returns the rotation
        matrix and length of beam

%% cross-section parameters, the sensitivity of damage found with
        respect to a change in brace thickness
t = [0.03:0.01:0.08]; % brace thickness
T = 0.11; % chord thickness
d = 1.00; % brace diameter
D = 1.83; % chord diameter

%calculating the pseudo load for thickness and radius sensitivity
        in the local coordinate system and making load files for the
        thickness pseudo loads as this is considered here.

for i=1:length(t)
    [Pr, Pt, time] = pseudo_load(d,t(i),L,R,82,T); %calculates the
        pseudo load from the stiffness sensitivity using the Euler-
        Bernoulli stiffness matrix: Pt and Pr has 12 rows
        corresponding to the 12 DOFs and as many columns as time
        steps
    for k=1:12 % makes a file for every DOF
        tname = round(t(i)*100);
        Tname = round(T*100);
        rname = round(d/2);
    end
end

```

```

        filename = sprintf('beam82_Pt%d_t0%d_r%d_T%d.txt',k ,tname
            , rname, Tname); % making a filename including the
            dimensions considered.
        fileID = fopen(filename, 'w');
        fprintf(fileID,'%6.2f %12.8f\n',[time; Pt(k,:)]); % the
            file has two columns, the first one is all timesteps
            and the second one is the pseudo load of DOF k
    end
end

%% find damage sensitivity

for i=1:length(t)
    [sN, sMy, sMz, dsNdt, dsMydt, dsMzdt] = stress_sensitivities
        (82, d, t(i), L, R, T); % imports the response sensitivity
        found with FEDEM and computes the stress sensitivities using
        the stress calculation matrix. Every output parameter has
        two rows corresponding to the value in node 1 and 2.

    [SCF, dSCF] = Kjoint_SCF_sensitivity(D, T, d, t(i), theta); %
        using K-joint SCF and using the least square method to
        calculate the values and sensitivities. These values are
        only valid for node 1 as node 2 is a X-joint. Dimensions: [[
        SCF_AC; SCF_AS; SCF_MIP; SCF_MOP], [dSCF_AC; dSCF_AS;
        dSCF_MIP; dSCF_MOP]]

    [dHSSdt_triad1, HSS_triad1] = HSS_sensitivities(SCF, dSCF,
        dsNdt, dsMydt, dsMzdt, sN, sMy, sMz); % finding the HSS
        sensitivities of node 1 by combining stresses and SCFs.
        Dimensions: [8xtimesteps, 8xtimesteps]

    [HSS_triad1, dHSSdt_triad1] = connected_chord(11, t(i), d, T, D
        , dHSSdt_triad1, HSS_triad1); % include the stresses from
        chord which have beam number 11. Dimensions: [8xtimesteps, 8
        xtimesteps]

    [dDdt(i,:), D(i,:)] = damage_sensitivity(HSS_triad1,
        dHSSdt_triad1); % find the damage and its sensitivity for
        all hot spots. Dimensions: [1x8, 1x8]

    multiplierList = [-0.005:0.001:0.004]; % thickness increment
        for taylor expansion

    Dnum = [];
    tnum = [];

    % Multiply the element with the multiplier list and append to
        the combined list
    Dnum = [Dnum, D(i,:)+dDdt(i,:).*multiplierList];

```

```
tnum = [tnum, t(i)+multiplierList];  
end
```

```
function [R, length] = rotationmatrix(z, triad1, triad2)

x = triad2-triad1; % x-axis in the direction of the beam
x = x/norm(x);
z = z/norm(z);
y = cross(x,z);

R = [x;y;z];
length = norm(triad2-triad1);
```

```

function [Pr, Pt, time] = pseudo_load(d,t,L,R,beamnumber, T)

%% material

E = 2.1e11;
G = 8.0769231e10;

%% geometry

r = d/2;
ri = r-t;

%% load files

tname = round(t*100);
rname = round(r*100);
Tname = round(T*100);

filename = sprintf('u_beam%d_t%d_r%d_T%d.txt', beamnumber, tname,
    rname, Tname);
fid = fopen(filename, 'r');
u = fscanf(fid, '%f', [13,inf]);
time = u(1,:);
u_global = u(2:end,:)-u(2:end,1); % as FEDEM gives the global
    position of the nodes, must subtract the initial position

%% transform displacements from global to local
u1 = R*u_global(1:3,:);
r1 = R*u_global(4:6,:);
u2 = R*u_global(7:9,:);
r2 = R*u_global(10:12,:);

u_local = [u1; r1; u2; r2];

%% stiffness sensitivity with respect to thickness
dAdt = 2*pi*ri;
dIdt = pi*ri^3;
dIpdt = dIdt*2;

% stiffness matrix
Ak = E*dAdt/L;
Ik = E*dIdt/(L^3);
Ipk = G*dIpdt/L;

dKdt = [Ak 0 0 0 0 0 -Ak 0 0 0 0 0; ...
    0 12*Ik 0 0 0 6*L*Ik 0 -12*Ik 0 0 0 6*L*Ik; ...

```

```

0 0 12*Ik 0 -6*L*Ik 0 0 0 -12*Ik 0 -6*L*Ik 0; ...
0 0 0 Ipk 0 0 0 0 -Ipk 0 0; ...
0 0 -6*L*Ik 0 4*L2*Ik 0 0 0 6*L*Ik 0 2*L2*Ik 0; ...
0 6*L*Ik 0 0 0 4*L2*Ik 0 -6*L*Ik 0 0 0 2*L2*Ik; ...
-Ak 0 0 0 0 0 Ak 0 0 0 0 0; ...
0 -12*Ik 0 0 0 -6*L*Ik 0 12*Ik 0 0 0 -6*L*Ik; ...
0 0 -12*Ik 0 6*L*Ik 0 0 0 12*Ik 0 6*L*Ik 0; ...
0 0 0 -Ipk 0 0 0 0 0 Ipk 0 0; ...
0 0 -6*L*Ik 0 2*L2*Ik 0 0 0 6*L*Ik 0 4*L2*Ik 0; ...
0 6*L*Ik 0 0 0 2*L2*Ik 0 -6*L*Ik 0 0 0 4*L2*Ik];

%% pseudo load with respect to thickness

Pt = -dKdt*u_local;

%% stiffness sensitivity with respect to the radius

dAdr = 2*pi*t;
dIdr = pi*(r3-ri3);
dIpdr = dIdt*2;

% stiffness matrix
Ak = E*dAdr/L;
Ik = E*dIdr/(L3);
Ipk = G*dIpdr/L;

dKdr = [Ak 0 0 0 0 0 -Ak 0 0 0 0 0; ...
0 12*Ik 0 0 0 6*L*Ik 0 -12*Ik 0 0 0 -6*L*Ik; ...
0 0 12*Ik 0 -6*L*Ik 0 0 0 -12*Ik 0 -6*L*Ik 0; ...
0 0 0 Ipk 0 0 0 0 -Ipk 0 0; ...
0 0 -6*L*Ik 0 4*L2*Ik 0 0 0 6*L*Ik 0 2*L2*Ik 0; ...
0 6*L*Ik 0 0 0 4*L2*Ik 0 -6*L*Ik 0 0 0 2*L2*Ik; ...
-Ak 0 0 0 0 0 Ak 0 0 0 0 0; ...
0 -12*Ik 0 0 0 -6*L*Ik 0 12*Ik 0 0 0 -6*L*Ik; ...
0 0 -12*Ik 0 6*L*Ik 0 0 0 12*Ik 0 6*L*Ik 0; ...
0 0 0 -Ipk 0 0 0 0 0 Ipk 0 0; ...
0 0 -6*L*Ik 0 2*L2*Ik 0 0 0 6*L*Ik 0 4*L2*Ik 0; ...
0 6*L*Ik 0 0 0 2*L2*Ik 0 -6*L*Ik 0 0 0 4*L2*Ik];

%% pseudo load with respect to the radius

Pr = -dKdr*u_local;

```

```

function [sN, sMy, sMz, dsNdt, dsMydt, dsMzdt] =
    stress_sensitivities(beamnumber, d,t, L, R, T)

%% material
E = 2.1e11;
G = 8.0769231e10;

%% geometry
r = d/2;

%% load files

tname = round(t*100);
rname = r*100;
Tname = T*100;

% displacements
filename = sprintf('u_beam%d_t%d_r%d_T%d.txt', beamnumber, tname,
    rname, Tname);
fid = fopen(filename, 'r');
u = fscanf(fid, '%f', [13,inf]);
time = u(1,:);
u = (u(2:end,:) - u(2:end,1)); % as FEDEM gives the global position
    of the nodes, must subtract the initial position

% translate to local system
u1 = R*u(1:3,:);
r1 = R*u(4:6,:);
u2 = R*u(7:9,:);
r2 = R*u(10:12,:);
u = [u1; r1; u2; r2];

% displacement sensitivities
filename = sprintf('dudt_beam%d_t%d_r%d_T%d.txt', beamnumber, tname,
    ,rname, Tname);
fid = fopen(filename, 'r');
dudt = fscanf(fid, '%f', [13,inf]);
time = dudt(1,:);
dudt = (dudt(2:end,:) - dudt(2:end,1)); % as FEDEM gives the global
    position of the nodes, must subtract the initial position

% translates to the local system
u1 = R*dudt(1:3,:);
r1 = R*dudt(4:6,:);
u2 = R*dudt(7:9,:);
r2 = R*dudt(10:12,:);

dudt = [u1; r1; u2; r2];

```

```

%% stresses

Ak = E/L;
Ik = E/(L^3)*r;
Ipk = 0; % not of interest, does not consider the torsional load
        and therefore neither its sensitivity

s_Kmatrix = [Ak 0 0 0 0 0 -Ak 0 0 0 0 0; ...
             0 12*Ik 0 0 0 6*L*Ik 0 -12*Ik 0 0 0 6*L*Ik; ...
             0 0 12*Ik 0 -6*L*Ik 0 0 0 -12*Ik 0 -6*L*Ik 0; ...
             0 0 0 Ipk 0 0 0 0 0 -Ipk 0 0; ...
             0 0 -6*L*Ik 0 4*L^2*Ik 0 0 0 6*L*Ik 0 2*L^2*Ik 0; ...
             0 6*L*Ik 0 0 0 4*L^2*Ik 0 -6*L*Ik 0 0 0 2*L^2*Ik; ...
             -Ak 0 0 0 0 0 Ak 0 0 0 0 0; ...
             0 -12*Ik 0 0 0 -6*L*Ik 0 12*Ik 0 0 0 -6*L*Ik; ...
             0 0 -12*Ik 0 6*L*Ik 0 0 0 12*Ik 0 6*L*Ik 0; ...
             0 0 0 -Ipk 0 0 0 0 0 Ipk 0 0; ...
             0 0 -6*L*Ik 0 2*L^2*Ik 0 0 0 6*L*Ik 0 4*L^2*Ik 0; ...
             0 6*L*Ik 0 0 0 2*L^2*Ik 0 -6*L*Ik 0 0 0 4*L^2*Ik];

% This matrix can not be used to determine the stresses due to
% shear or torsion, as the transversal stress formula is not
% considered. This matrix can only be used for the elements
% considered below.

s = s_Kmatrix*u;
sN = [s(1,:);s(7,:)];
sMy = [s(5,:);s(11,:)];
sMz = [s(6,:);s(12,:)];

%% stress sensitivities with respect to thickness

dsdt = s_Kmatrix*dudt;

dsNdt = [dsdt(1,:);dsdt(7,:)];
dsMydt = [dsdt(5,:);dsdt(11,:)];
dsMzdt = [dsdt(6,:);dsdt(12,:)];

%% stress sensitivities with respect to the radius

Ak = 0;
Ik = E/(L^3);
Ipk = 0; % not of interest, does not consider the torsional load
        and therefore neither its sensitivity

dsdr_Kmatrix = [Ak 0 0 0 0 0 -Ak 0 0 0 0 0; ...
                0 12*Ik 0 0 0 6*L*Ik 0 -12*Ik 0 0 0 6*L*Ik; ...
                0 0 12*Ik 0 -6*L*Ik 0 0 0 -12*Ik 0 -6*L*Ik 0; ...
                0 0 0 Ipk 0 0 0 0 0 -Ipk 0 0; ...
                0 0 -6*L*Ik 0 4*L^2*Ik 0 0 0 6*L*Ik 0 2*L^2*Ik 0; ...
                0 6*L*Ik 0 0 0 4*L^2*Ik 0 -6*L*Ik 0 0 0 4*L^2*Ik];

```



```
0 6*L*Ik 0 0 0 4*L2*Ik 0 -6*L*Ik 0 0 0 2*L2*Ik; ...
-Ak 0 0 0 0 0 Ak 0 0 0 0 0; ...
0 -12*Ik 0 0 0 -6*L*Ik 0 12*Ik 0 0 0 -6*L*Ik; ...
0 0 -12*Ik 0 6*L*Ik 0 0 0 12*Ik 0 6*L*Ik 0; ...
0 0 0 -Ipk 0 0 0 0 0 Ipk 0 0; ...
0 0 -6*L*Ik 0 2*L2*Ik 0 0 0 6*L*Ik 0 4*L2*Ik 0; ...
0 6*L*Ik 0 0 0 2*L2*Ik 0 -6*L*Ik 0 0 0 4*L2*Ik];
% This matrix can not be used to determine the stresses due to
shear or torsion, as the transversal stress formula is not
considered. This matrix can only be used for the elements
considered below.

dsdr = dsdr_Kmatrix*u + s_Kmatrix*dudr;

dsNdr = [dsdr(1,:);dsdr(7,:)];
dsMydr = [dsdr(5,:);dsdr(11,:)];
dsMzdr = [dsdr(6,:);dsdr(12,:)];
% these are not taken out of this function as thickness sensitivity
is considered here, but this can easily be changed by defining
the function output as [sN, sMy, sMz, dsNdr, dsMydr, dsMzdr].
```

```
function [SCF, dSCF]=Kjoint_SCF_sensitivity(D,T,d,t,theta)

%% SCF20
[c,a,b,da,db]=SCF20t(D,T,d,theta);

SCF20=c;
dSCF20=0;
for i=1:length(a)
    SCF20=SCF20+a(i)*t^(b(i));
end
for i=1:length(a)
    dSCF20=dSCF20+da(i)*t^(db(i));
end

%% SCF21
[c,a,b,da,db]=SCF21t(D,T,d,theta);

SCF21=c;
dSCF21=0;
for i=1:length(a)
    SCF21=SCF21+a(i)*t^(b(i));
end
for i=1:length(a)
    dSCF21=dSCF21+da(i)*t^(db(i));
end

%% SCF_AC og dSCF_AC
SCF_AC=max([SCF20, SCF21]);

for i=1:length(SCF_AC)
    if SCF_AC(i)==SCF20(i)
        dSCF_AC(i)=dSCF20(i);
    else
        dSCF_AC(i)=dSCF21(i);
    end
end

%% SCF_AS and dSCF_AS balanced load has the same SCF here
SCF_AS=SCF_AC;
dSCF_AS=dSCF_AC;

%% SCF 8
[c,a,b,da,db]=SCF8t(D,T,d,theta);

SCF8=c;
```

```
dSCF8=0;
for i=1:length(a)
    SCF8=SCF8+a(i)*t^(b(i));
end
for i=1:length(a)
    dSCF8=dSCF8+da(i)*t^(db(i));
end

%% SCF 9
[c,a,b,da,db]=SCF9t(D,T,d,theta);

SCF9=c;
dSCF9=0;
for i=1:length(a)
    SCF9=SCF9+a(i)*t^(b(i));
end
for i=1:length(a)
    dSCF9=dSCF9+da(i)*t^(db(i));
end

%% SCF_MIP and dSCF_MIP
SCF_MIP=max([SCF8, SCF9]);

for i=1:length(SCF_MIP)
    if SCF_MIP(i)==SCF8(i)
        dSCF_MIP(i)=dSCF8(i);
    else
        dSCF_MIP(i)=dSCF9(i);
    end
end

%% SCF 23
[c,a,b,da,db]=SCF23t(D,T,d,theta);

SCF23=c;
dSCF23=0;
for i=1:length(a)
    SCF23=SCF23+a(i)*t^(b(i));
end
for i=1:length(a)
    dSCF23=dSCF23+da(i)*t^(db(i));
end

%% SCF 26
[c,a,b,da,db]=SCF24t(D,T,d,theta);

SCF24=c;
dSCF24=0;
for i=1:length(a)
    SCF24=SCF24+a(i)*t^(b(i));
```

```
end
for i=1:length(a)
    dSCF24=dSCF24+da(i)*t^(db(i));
end

%% SCF_MOP and dSCF_MOP
SCF_MOP=max([SCF23, SCF24]);

for i=1:length(SCF_MIP)
    if SCF_MOP(i)==SCF23(i)
        dSCF_MOP(i)=dSCF23(i);
    else
        dSCF_MOP(i)=dSCF24(i);
    end
end

SCF = [SCF_AC; SCF_AS; SCF_MIP; SCF_MOP];
dSCF = [dSCF_AC; dSCF_AS; dSCF_MIP; dSCF_MOP];
```

```

function [dHSS_triad1, HSS_triad1] = HSS_sensitivities(SCF, dSCF,
    dsNdx, dsMydx, dsMzdx, sN, sMy, sMz)

SCF_AC = SCF(1);
SCF_AS = SCF(2);
SCF_MIP = SCF(3); % z-moment, must be consistent with model
SCF_MOP = SCF(4); % y-moment, must be consistent with model

dSCF_AC = dSCF(1);
dSCF_AS = dSCF(2);
dSCF_MIP = dSCF(3); % z-moment
dSCF_MOP = dSCF(4); % y-moment

dHSS1dx = SCF_AC*dsNdx + SCF_MIP*dsMzdx + dSCF_AC*sN + dSCF_MIP*sMz
    ;

dHSS2dx = 1/2*(SCF_AC+SCF_AS)*dsNdx + sqrt(2)/2*SCF_MIP*dsMzdx -
    sqrt(2)/2*SCF_MOP*dsMydx + 1/2*(dSCF_AC+dSCF_AS)*sN + sqrt(2)/2*
    dSCF_MIP*sMz - sqrt(2)/2*dSCF_MOP*sMy;

dHSS3dx = SCF_AS*dsNdx - SCF_MOP*dsMydx + dSCF_AS*sN - dSCF_MOP*sMy
    ;

dHSS4dx = 1/2*(SCF_AC+SCF_AS)*dsNdx - sqrt(2)/2*SCF_MIP*dsMzdx -
    sqrt(2)/2*SCF_MOP*dsMydx + 1/2*(dSCF_AC+dSCF_AS)*sN - sqrt(2)/2*
    dSCF_MIP*sMz - sqrt(2)/2*dSCF_MOP*sMy;

dHSS5dx = SCF_AC*dsNdx - SCF_MIP*dsMzdx + dSCF_AC*sN - dSCF_MIP*sMz
    ;

dHSS6dx = 1/2*(SCF_AC+SCF_AS)*dsNdx - sqrt(2)/2*SCF_MIP*dsMzdx +
    sqrt(2)/2*SCF_MOP*dsMydx + 1/2*(dSCF_AC+dSCF_AS)*sN - sqrt(2)/2*
    dSCF_MIP*sMz + sqrt(2)/2*dSCF_MOP*sMy;

dHSS7dx = SCF_AS*dsNdx + SCF_MOP*dsMydx + dSCF_AS*sN + dSCF_MOP*sMy
    ;

dHSS8dx = 1/2*(SCF_AC+SCF_AS)*dsNdx + sqrt(2)/2*SCF_MIP*dsMzdx +
    sqrt(2)/2*SCF_MOP*dsMydx + 1/2*(dSCF_AC+dSCF_AS)*sN + sqrt(2)/2*
    dSCF_MIP*sMz + sqrt(2)/2*dSCF_MOP*sMy;

dHSS_triad1=[dHSS1dx(1,:); dHSS2dx(1,:); dHSS3dx(1,:); dHSS4dx(1,:)
    ; dHSS5dx(1,:); dHSS6dx(1,:); dHSS7dx(1,:); dHSS8dx(1,:)];

HSS1 = SCF_AC*sN + SCF_MIP*sMz;

HSS2 = 1/2*(SCF_AC+SCF_AS)*sN + sqrt(2)/2*SCF_MIP*sMz - sqrt(2)/2*
    SCF_MOP*sMy;

```

```
HSS3 = SCF_AS*sN - SCF_MOP*sMy;

HSS4 = 1/2*(SCF_AC+SCF_AS)*sN - sqrt(2)/2*SCF_MIP*sMz - sqrt(2)/2*
      SCF_MOP*sMy;

HSS5 = SCF_AC*sN - SCF_MIP*sMz;

HSS6 = 1/2*(SCF_AC+SCF_AS)*sN - sqrt(2)/2*SCF_MIP*sMz + sqrt(2)/2*
      SCF_MOP*sMy;

HSS7 = SCF_AS*sN + SCF_MOP*sMy;

HSS8 = 1/2*(SCF_AC+SCF_AS)*sN + sqrt(2)/2*SCF_MIP*sMz + sqrt(2)/2*
      SCF_MOP*sMy;

HSS_triad1 = [HSS1(1,:); HSS2(1,:); HSS3(1,:); HSS4(1,:); HSS5(1,:)
              ; HSS6(1,:); HSS7(1,:); HSS8(1,:)];
```

```
function [HSS_triad1, dHSSdt_triad1] = connected_chord_11(
    beamnumber, t_b, d_b, t_c, d_c, dHSSdt_triad1, HSS_triad1)

%% geometry
r_b = d_b/2;

%% rotation matrix of beam 11
z = [-1.0283055e-07, - 125.94947, -11.694473];

triad1 = [14.935558, 14.935558, 2.9440421];
triad2 = [13.766111, 13.766111, 15.538989];

[R_chord, L_chord] = rotationmatrix(z, triad1, triad2);

%% stress and its sensitivities of chord
[sN, sMy, sMz, dsNdt, dsMydt, dsMzdt] = stress_sensitivities_chord(
    beamnumber, d_b, t_b, L_chord, R_chord, d_c, t_c);

%% include the chord stresses in hot spot 1 and 5 with SCF=1.20
HSS_contribution_triad1 = 1.2*(sN(1,:) + sMy(1,:))
    .* [1; 0; 0; 0; 1; 0; 0; 0];
dHSSdt_contribution_triad1 = 1.2*(dsNdt(1,:) + dsMydt(1,:))
    .* [1; 0; 0; 0; 1; 0; 0; 0];

HSS_triad1 = HSS_triad1 + HSS_contribution_triad1;
dHSSdt_triad1 = dHSSdt_triad1 + dHSSdt_contribution_triad1;
```

```

function [sN, sMy, sMz, dsNdt, dsMydt, dsMzdt] =
    stress_sensitivities_chord(beamnumber, d_b, t_b, L_chord,
        R_chord, d_c, t_c)

%% material
E = 2.1e11;
G = 8.0769231e10;

%% geometry
r = d_b/2;
r_c = d_c/2;

%% load displacement files and sensitivities

tname = round(t_b*100);
rname = round(r*100);
Tname = round(t_c*100);
filename = sprintf('u_beam%d_t0%d_r%d_T%d.txt', beamnumber, tname,
    rname, Tname);
fid = fopen(filename, 'r');
u = fscanf(fid, '%f', [13,inf]);
time = u(1,:);
u = u(2:end,:)-u(2:end,1);

% transform from global to the local system
u1 = R_chord*u(1:3,:);
r1 = R_chord*u(4:6,:);
u2 = R_chord*u(7:9,:);
r2 = R_chord*u(10:12,:);

u = [u1; r1; u2; r2];

filename = sprintf('dudt_beam%d_t0%d_r%d_T%d.txt', beamnumber, tname
    ,rname, Tname);
fid = fopen(filename, 'r');
dudt = fscanf(fid, '%f', [13,inf]);
time = dudt(1,:);
dudt = (dudt(2:end,:)-dudt(2:end,1));

% transform from global to the local system
u1 = R_chord*dudt(1:3,:);
r1 = R_chord*dudt(4:6,:);
u2 = R_chord*dudt(7:9,:);
r2 = R_chord*dudt(10:12,:);

dudt = [u1; r1; u2; r2];

%% stresses in chord

Ak = E/L_chord;

```



```

Ik = E/(L_chord^3)*r_c;
Ipk = 0; % not of interest, does not consider the torsional load
and therefore neither its sensitivity

s_Kmatrix = [Ak 0 0 0 0 0 -Ak 0 0 0 0 0; ...
 0 12*Ik 0 0 0 6*L_chord*Ik 0 -12*Ik 0 0 0 6*L_chord*Ik; ...
 0 0 12*Ik 0 -6*L_chord*Ik 0 0 0 -12*Ik 0 -6*L_chord*Ik 0; ...
 0 0 0 Ipk 0 0 0 0 0 -Ipk 0 0; ...
 0 0 -6*L_chord*Ik 0 4*L_chord^2*Ik 0 0 0 6*L_chord*Ik 0 2*
 L_chord^2*Ik 0; ...
 0 6*L_chord*Ik 0 0 0 4*L_chord^2*Ik 0 -6*L_chord*Ik 0 0 0 2*
 L_chord^2*Ik; ...
 -Ak 0 0 0 0 0 Ak 0 0 0 0 0; ...
 0 -12*Ik 0 0 0 -6*L_chord*Ik 0 12*Ik 0 0 0 -6*L_chord*Ik; ...
 0 0 -12*Ik 0 6*L_chord*Ik 0 0 0 12*Ik 0 6*L_chord*Ik 0; ...
 0 0 0 -Ipk 0 0 0 0 0 Ipk 0 0; ...
 0 0 -6*L_chord*Ik 0 2*L_chord^2*Ik 0 0 0 6*L_chord*Ik 0 4*
 L_chord^2*Ik 0; ...
 0 6*L_chord*Ik 0 0 0 2*L_chord^2*Ik 0 -6*L_chord*Ik 0 0 0 4*
 L_chord^2*Ik];

% This matrix can not be used to determine the stresses due to
shear or torsion, as the transversal stress formula is not
considered. This matrix can only be used for the elements
considered below.

s = s_Kmatrix*u;
sN = [s(1,:);s(7,:)];
sMy = [s(5,:);s(11,:)];
sMz = [s(6,:);s(12,:)];

dsdt = s_Kmatrix*dudt;

dsNdt = [dsdt(1,:);dsdt(7,:)];
dsMydt = [dsdt(5,:);dsdt(11,:)];
dsMzdt = [dsdt(6,:);dsdt(12,:)];

```

```

function [dDdx, D] = damage_sensitivity(HSS, dHSS)

HSS = HSS*10^(-6); %MPa
dHSS = dHSS*10^(-6); %MPa

%% S-N curve parameters
m = 5;
loga = 16.13;
a = 10^(loga);
simtime = 37.7; %simulation time in seconds

%% scaling to the entire lifetime
d = 0.006*3*20*365*24*60*60./simtime; %including the probability of
    occurrence of the load case

%% find the change in stress ranges
% The rainflow function in MATLAB just give the start and end point
    not which one is the peak and which is the valley, therefore
    these must be identified such that the stress range sensitivity
    gets the correct sign

for i=1:8 % all 8 HSS
    HSS_rf=rainflow(HSS(i,:)); % using the rainflow count
        implemented in MATLAB
    n=HSS_rf(:,1); % number of cycles
    deltas=HSS_rf(:,2); % stress range
    maximum=0;
    minimum=0;
    for j=1:length(HSS_rf(:,1))
        start=HSS_rf(j,4); %start index of stress cycle
        slutt=HSS_rf(j,5); %end index of stress cycle
        if HSS(i,start+1)<HSS(i,start)
            maximum(j)=start;
            minimum(j)=slutt;
        else
            maximum(j)=slutt;
            minimum(j)=start;
        end
    end
    end

    ddeltasdx=(dHSS(i,toppunkt)-dHSS(i,bunnpunkt))'; % the stress
        range sensitivity

%% Damage sensitivity and damage from simulation
    dDdx(i)=m*d/a*sum(n.*(deltas).^ (m-1) .*ddeltasdx);
    D(i)=d/a*sum(n.*(deltas).^ (m));

end

```

D Linear regression to find SCF sensitivity for SCF 5

```

function [c,a,b,da,db]=SCF5t(D,T,d,theta)
% SCF5t is a function that takes in the constant geometry of the
  joint.
% It returns 5 lists that contain the constants in the exponential
  function and its derivative

% chord-end-fixity parameter
C=0.7;
C1=2*(C-0.5);

L=12.7; % chord length

t=[0.03:0.0001:0.06]; % variable considered for differentiation,
  inside the range we are interested in

% geometry parameters
beta=d./D;
alpha=2*L./D;
gamma=D./(2*T);
tau=t./T;

% As SCF5 depends on t with two different exponents, the least
  square methods are performed on these terms individually

SCF1 = gamma.*tau.^1.1.*(1.11-3*(beta-0.52).^2).*sind(theta).^1.6;
  % term 1
SCF2=C1*(0.8.*alpha-6).*tau.*beta.^2.*(1-beta.^2).^0.5.*sind(2.*
  theta).^2; % term 2

y1=log(SCF1); % logarithmic SCF1 y-data
y2=log(SCF2); % logarithmic SCF2 y-data

x=log(t); %logarithmic time x-data

p1=polyfit(x,y1,1); % polyfit determines the a1 and b1 in this
  linear function: log(SCF1)=log(a1)+b1*log(t)
a1=exp(p1(2)); % remove the logarithmic scale of a1
p2=polyfit(x,y2,1); % determines the a2 and b2 in this linear
  function: log(SCF2)=log(a2)+b2*log(t)
a2=exp(p2(2)); % remove the logarithmic scale of a2

c=0; % as there is no constant term in SCF5 this constant term is
  zero

% creating a list of the coefficients such that they can be
  combined to one function at a later point: SCF5=a1*t^b1+a2*t^b2
a=[a1,a2];
b=[p1(1), p2(1)];

```

```
% finding the differentiated coefficients of SCF5 which at a later  
    point can be combined: d(SCF5)/dt=da1*t^db1+da2*t^db2  
da=a.*b;  
db=b-1;
```



 **NTNU**

Norwegian University of
Science and Technology